

# **Stony Brook University**



OFFICIAL COPY

**The official electronic file of this thesis or dissertation is maintained by the University Libraries on behalf of The Graduate School at Stony Brook University.**

**© All Rights Reserved by Author.**

# **Large Scale Integration Issues in Superconducting Circuits**

A Dissertation Presented

by

**Supradeep Narayana**

to

The Graduate School

in Partial Fulfillment of the

Requirements

for the Degree of

**Doctor of Philosophy**

in

**Electrical Engineering**

Stony Brook University

**May 2010**

Copyright by  
**Supradeep Narayana**  
**2010**

**Stony Brook University**

The Graduate School

**Supradeep Narayana**

We, the dissertation committee for the above candidate for the

Doctor in Philosophy degree, hereby recommend

acceptance of this dissertation.

**Alex Doboli, Advisor of Dissertation**

**Associate professor, Department of Electrical and Computer engineering**

**Vasili K. Semenov, Co-Advisor of Dissertaion**

**Principle Investigator, Department of Physics and Astronomy**

**Ridha Kamoua, Chairperson of defense**

**Associate Professor, Undergraduate Program Director, Department of Electrical  
and Computer engineering**

**Dmitri Donetski, Assistant Professor,**

**Department of Electrical and Computer engineering**

**Dmitri V. Averin, Professor**

**Department of Physics and Astronomy**

The dissertation is acceptable by the Graduate School.

Lawrence Martin  
Dean of the Graduate School

Abstract of the Dissertation

# **Large Scale Integration Issues in Superconducting Circuits**

by

**Supradeep Narayana**

**Doctor of Philosophy**

in

**Electrical Engineering**

Stony Brook University

**2010**

Superconducting digital logic technology, Rapid Single Flux Quantum (RSFQ), is established as the fastest technology in microelectronics based on Josephson junction devices. Technological challenges in large scale integration of superconductor circuits (RSFQ) namely: flux trapping, low power dissipation and multi-chip modules are addressed here. One of the main limitations of the integration of the RSFQ circuits is flux trapping, which arises due to the presence of residual magnetic field during transition of the circuit into superconducting state. Flux trapping is an unusual problem specific in only superconducting circuits. The effect of flux trapping in RSFQ circuits is studied, with a controlled 3-D magnetic field setup, quantitatively. Layout configuration with different moat patterns making RSFQ circuits tolerant to external magnetic field upto 20mG was also developed.

Low power issue was addressed by developing a new logic family. Power independent logic, an improved form of RSFQ logic, enables the circuits to operate only when needed and circuits can be switched off the remaining time; thereby eliminating static power consumption by retaining the logic state of the circuit. Flux trapping has also been investigated in power independent cells.

Current recycling is a technique to reduce the bias current applied for the operation of the RSFQ circuits. In this technique the cells are biased by serial connections. The reduction in supply current is proportional to number of blocks connected in series. The effect of magnetic field on the operating margins of the current recycling circuits has also been studied.

Operation of Multi-chip modules, one of the most viable solutions to develop large scale circuits, was demonstrated. Multi-chip modules with lithographically designed bumps is presented where data transmission rate between two superconducting chips exceed 100GHz. Finally, the development of the multi-modulator ADC for low noise front end under-development is discussed.

# TABLE OF CONTENTS

|   |            |
|---|------------|
| <b>LIST OF FIGURES</b> .....  | <b>VII</b> |
| <b>LIST OF TABLES</b> .....   | <b>XIV</b> |
| <b>ACKNOWLEDGEMENTS</b> .....   | <b>XXI</b> |
| <br>  |            |
| <b>1. INTRODUCTION</b> .....  | <b>1</b>   |
| 1.1 SUPERCONDUCTIVITY .....   | 1          |
| 1.2 JOSEPHSON JUNCTION .....  | 2          |
| 1.3 FLUX QUANTIZATION .....   | 6          |
| 1.4 GENERATION OF FLUX QUANTA.....  | 7          |
| 1.5 RSFQ CIRCUITS .....   | 7          |
| 1.5.1 PRINCIPLE COMPONENTS OF RSFQ CIRCUITS.....                                  | 8          |
| 1.6 LARGE SCALE RSFQ CIRCUITS.....  | 10         |
| 1.6.1 MOTIVATION .....  | 10         |
| 1.7 CONTRIBUTION .....  | 13         |
| 1.8 LIMITATIONS .....   | 15         |
| <br>  |            |
| <b>2. FLUX TRAPPING IN SUPERCONDUCTING CIRCUITS: THEORY AND EXPERIMENTS</b> ..... | <b>17</b>  |
| 2.1 INTRODUCTION .....  | 17         |
| 2.2 THEORETICAL FACTS.....  | 17         |
| 2.3 NUMERICAL SIMULATIONS OF MAGNETIC FORCE ON VORTICES .....                     | 20         |
| 2.4 HOW TRAPPED FLUX AFFECTS SUPERCONDUCTING CIRCUITS.....                        | 22         |
| 2.5 RSFQ CIRCUITS FOR FLUX TRAPPING EXPERIMENTS .....                             | 23         |
| 2.5.1 MEASUREMENT PROCEDURE .....   | 23         |
| 2.6 EXPERIMENTAL SETUPS.....  | 24         |
| 2.7 ANALYSIS OF EXPERIMENTAL RESULTS .....  | 26         |
| 2.7.1 GLOBAL ANALYSIS OF THE CIRCUIT .....  | 26         |
| 2.7.2 MARGINS OF INDIVIDUAL D CELLS .....   | 27         |
| 2.8 DISCUSSION.....   | 29         |
| <br>  |            |
| <b>3. MOATS IN SUPERCONDUCTING CIRCUITS</b> .....                                 | <b>34</b>  |
| 3.1 INTRODUCTION .....  | 34         |
| 3.2 BASIC DESIGN CONSIDERATIONS OF MOATS.....                                     | 35         |
| 3.3 MOAT PATTERNS .....   | 36         |
| 3.4 THRESHOLD LIMIT OF MOAT PATTERN .....   | 43         |
| 3.5 EXPERIMENTAL RESULTS.....   | 44         |
| 3.6 EMPIRICAL RULES FOR DEVELOPING MOAT PATTERNS .....                            | 45         |
| 3.7 FABRICATION DEPENDENCY .....  | 46         |
| 3.8 DISCUSSION .....  | 46         |
| <br>  |            |
| <b>4. POWER INDEPENDENT RSFQ LOGIC CIRCUITS</b> .....                             | <b>48</b>  |

|  |            |
|--|------------|
| 4.1 INTRODUCTION .....   | 48         |
| 4.2.BASICS OF POWER INDEPENDENT OPERATION .....  | 48         |
| 4.3 DEVELOPING POWER INDEPENDENT RS FLIP-FLOP .....                                    | 50         |
| 4.4 INVESTIGATION OF POWER INDEPENDENT SHIFT REGISTER .....                            | 51         |
| 4.4.1 DESIGN OF 6-BIT SHIFT REGISTER WITH POWER INDEPENDENT CELLS .....                | 51         |
| 4.4.2 EXPERIMENTAL RESULTS .....   | 52         |
| 4.5 FLUX TRAPPING IN POWER INDEPENDENT RSFQ CELLS .....                                | 53         |
| 4.6 DISCUSSION AND CONCLUSION.....   | 60         |
| <b>5. CURRENT RECYCLING: TECHNIQUE AND APPLICATION .....</b>                           | <b>61</b>  |
| 5.1 INTRODUCTION .....   | 61         |
| 5.2 SERIAL BIASING CIRCUIT TECHNIQUE .....   | 62         |
| 5.2.1 EXPPTERIMENTAL VERIFICATION OF CURRENT RECYCLING CIRCUIT .....                   | 65         |
| 5.3 SUMMING AMPLIFIER BASED OUTPUT DRIVER: APPLICATION OF FLOATING GROUNDS<br>JTL..... | 67         |
| 5.3.1EXPERIMENTAL RESULTS OF SUMMING AMPLIFIERS.....                                   | 70         |
| 5.4 EFFECT OF EXTERNAL MAGNETIC FIELD.....   | 72         |
| 5.4.1 IMPACTOF MAGNETIC FIELD ON 10-STAGE FTL BASED OUTPUT DRIVER.....                 | 75         |
| 5.5 DISCUSSION AND CONCLUSION .....  | 75         |
| <b>6. MULTI-CHIP MODULES .....</b>   | <b>77</b>  |
| 6.1 INTRODUCTION .....   | 77         |
| 6.2 MCM MODELING.....  | 77         |
| 6.2.1New BUMP STRUCTURE .....  | 79         |
| 6.3 TEST CIRCUIT.....  | 83         |
| 6.4 EXPERIMENTAL RESULTS.....  | 84         |
| 6.5 DISCUSSION AND CONCLUSION .....  | 86         |
| <b>7. MULTIMODULATION ADC CONCLUSION AND FUTURE WORK.....</b>                          | <b>90</b>  |
| 7.1 INTRODUCTION .....   | 90         |
| 7.2 BEHAVIORAL SYSTEM SIMULATION OF MULTIMODULATOR ADC .....                           | 90         |
| 7.3 CIRCUIT LEVEL DESIGN AND SIMULATION.....   | 93         |
| 7.3.1 DETERMINTATION OF CIRCUIT PARAMETERS FOR ADC.....                                | 93         |
| 7.3.2 TRANSFORMER DESIGN .....   | 94         |
| 7.3.3 LC LOW PASS FILTER DESIGN .....  | 96         |
| 7.5 PSCAN SIMULATION OF THE 4-MODULATOR ADC .....                                      | 99         |
| 7.6 DISCUSSION AND FUTURE WORK.....  | 102        |
| <b>8. CONCLUSION AND FUTURE WORK .....</b>   | <b>103</b> |
| 8.1 CONCLUSIONS .....  | 103        |
| 8.2 RECOMMENDATIONS FOR FUTURE WORK .....  | 104        |
| <b>REFERENCES.....</b>   | <b>107</b> |
| <b>APPENDIX .....</b>  | <b>114</b> |



# LIST OF FIGURES

|  |    |
|--|----|
| <b>Figure 1.1</b> Temperature dependence of resistance of a superconducting material .....   | 2  |
| <b>Figure 1.2</b> RSJ model for Josephson junction.....  | 3  |
| <b>Figure 1.3</b> I-V characteristic for unshunted (a) and resistively shunted (b) Josephson junction.....   | 4  |
| <b>Figure 1.4</b> A single junction interferometer.....  | 7  |
| <b>Figure 1.5</b> A Josephson transmission line (JTL), where single flux quantum is transferred through J1 by entering J1-L2-L3-J2. ....   | 8  |
| <b>Figure 1.6</b> Two Junction Comparator.....   | 9  |
| <b>Figure 2.1</b> Distribution of surface currents in superconducting film with a circular virtual (or probe) hole $v$ and a moat. The currents are induced by flux frozen in circular hole .....  | 22 |
| <b>Figure 2.2</b> Structure of the counter-flow shift register consisting of D cells (a) and timing JTL splitters (b). Note that D cells have extra current terminals (Probe) connected with the separate power line with zero nominal bias voltage..... | 25 |
| <b>Figure 2.3</b> Layout of the test circuit (a) and one of D cells (b). Solid black lines show holes (moats) in the lower ground plane. ....  | 25 |
| <b>Figure 2.4</b> (a) cold head of the Cryo-cooler (b) 3D Helmholtz coil setup.....  | 26 |
| <b>Figure 2.5</b> Spread of upper and lower are bias margins for major components of the test circuit. The stripes show the minimal margins required for further testing of individual cells.....  | 27 |
| <b>Figure 2.6</b> The probability of too narrow margins or incorrect operation at different perpendicular magnetic fields.....   | 28 |
| <b>Figure 2.7</b> Margins of D cells not affected by trapped flux. (a) Shows margins for 16 individual cells. (b) Shows the same data but “convolved” position of cells in four groups of 4-bit shift registers.....                                     | 28 |

|  |       |
|--|-------|
| <b>Figure 2.8</b> Deviations of margins for all 16 cells repeatedly measured at different magnetic fields .....  | 30    |
| <b>Figure 2.9</b> Probabilities of deviations of margins as functions of normal magnetic field. ....   | 31    |
| <b>Figure 2.10</b> Probabilities of deviations of margins as functions of tangential field.....  | 32    |
| <b>Figure 2.11</b> Probabilities of deviations of D flip-flop threshold currents caused by flux trapping in tangential (a) and normal (b) magnetic fields. Please note that the tangential fields are larger than normal ones. As a result, it would be incorrect to use this plot to compare sensitivities to tangential and normal fields.....                   | 33    |
| <b>Figure 3.1</b> It is a 6bit counter clock shift register. The chip was fabricated at Hypres with 1kA/cm <sup>2</sup> process. JJ count 996 .....  | 39    |
| <b>Figure 3.2</b> Block diagram of the shift register. ....  | 38    |
| <b>Figure 3.3</b> Layouts configurations for different moat patterns. ....   | 39,40 |
| <b>Figure 3.4</b> Deviation of the threshold current induced by frozen flux as a function of applied magnetic field perpendicular to the chip. Solid vertical lines show the threshold magnetic field that separates acceptable and unacceptable values of the ambient magnetic field. Different plots (see text) correspond to different moat configurations..... | 41    |
| <b>Figure 3.5</b> Bubbles represent the probability of a deviation of threshold current caused by trapped vortices. Small bubbles correspond to the deviations in 1-4 $\mu$ A range, medium bubbles correspond to 4-20 $\mu$ A deviations, large bubbles indicate deviations that are greater than 20 $\mu$ A. ....  | 42    |
| <b>Figure 3.6</b> Threshold fields (in mG) for investigated moat patterns. Names of corresponding microphotographs in Figure. 3.3 are shown below the columns. ....  | 43    |
| <b>Figure 3.7</b> The threshold current deviation for layout 1e, for mask releases (a) KL1094 (b) KL1025. ....   | 47    |
| <b>Figure 4.1</b> A single junction SQUID as the simplest power independent cell.....  | 49    |

|   |    |
|---|----|
| <b>Figure 4.2</b> Transformation of a conventional RSFQ (a) RS flip-flop into a (b) power independent cell .....  | 50 |
| <b>Figure 4.3</b> Power Independent D flip-flop. Bias current IPI does 2 things: it “activates” SQUID with junction J0 and power the cell during its normal operation.....  | 52 |
| <b>Figure 4.4</b> Current (upper trace) and voltage waveforms illustrating the power independent operation of D cell. Note that the “activation” procedure could require larger current IPI than those during the regular circuit operation. .... | 53 |
| <b>Figure 4.5</b> The microphotograph of the shift registers of the power independent cells. The first three registers are designed with power independent cells .....  | 54 |
| <b>Figure 4.6</b> Low speed testing of one shift registers. The logic ‘1’ applied to the input (two lower traces) is read out from the output (the second from top trace) after 6 clock cycles (middle traces).....                               | 55 |
| <b>Figure 4.7</b> Three layout configurations for PI D flip-flop . ....   | 56 |
| <b>Figure 4.8</b> Threshold deviations for corresponding layouts configurations in figure 4.7.57  |    |
| <b>Figure 4.9</b> Probability of flux trapping in the each cells for the corresponding layout in figure 4.7.. ....  | 58 |
| <b>Figure 5.1</b> (a) Block diagram of current recycling digital transmission line.(b) The microphotograph of the layout digital transmission line.....   | 63 |
| <b>Figure 5.2</b> Circuit schematic for magnetic coupled SFQ pulse transfer between driver and receiver. ....   | 64 |
| <b>Figure 5.3</b> Layout for magnetic coupled SFQ pulse transfer between driver and receiver . ....   | 65 |
| <b>Figure 5.4</b> The complete block diagram of the serial biasing method.....  | 66 |
| <b>Figure 5.5</b> The microphotograph of the chip for demonstrating current recycling. ....   | 66 |
| <b>Figure 5.6</b> The digital waveform of the input and three outputs as shown in figure 5.4. The traces 1,3,5 are the outputs and 2 is the input trace .....   | 67 |

|  |    |
|--|----|
| <b>Figure 5.7</b> The (a) schematic of the floating transmission line and its (b) block diagram .  | 68 |
| <b>Figure 5.8</b> The (a) schematic of the N floating transmission lines and its (b) block diagram.  | 68 |
| <b>Figure 5.9</b> The microphotograph of the summing amplifier based output drivers – designs based on serial and parallel connections- containing both .  | 69 |
| <b>Figure 5.10</b> (a) The layout of the parallel connected summing amplifier based on floating transmission line. (b) Shows the microphotograph of the summing amplifier .  | 69 |
| <b>Figure 5.11</b> Measurements of the driver shown. Three inputs are operational at bias currents from 1.3 mA to 1.9 mA. One input has lower margins (from 0.85 mA to 0.98 mA). Please note that horizontal axis shows only half of total applied bias current. | 70 |
| <b>Figure 5.12</b> Layout output drivers with (a) 10 floating transmission lines and (b) 20 floating transmission lines connected in series.   | 71 |
| <b>Figure 5.13</b> Measurement of output voltage of the driver shown as a function of bias current. It is easy to see that at nominal bias (2.0 mA) the load circuit could be from 0 ma to 0.5 mA .  | 71 |
| <b>Figure 5.14</b> . Measurement of the driver with 20 FTLs. The driver operates at bias current from 1.5 mA to 2.0 mA.  | 72 |
| <b>Figure 5.15</b> The affect of magnetic filed on margins of the operations. (a) x-axis ,(b) y-axis and (c) z-axis, are the direction of the magnetic field applied to the circuit as shown .   | 73 |
| <b>Figure 5.16</b> Margins of the circuit due to the scan of 360 degrees of magnetic filed. The orientation of the chip to the axis of the magnetic field is also shown as reference.  | 74 |
| <b>Figure 5.17</b> The affect of magnetic filed on the output of the driver (10 serially connected FTL) operations. (a) x-axis ,(b) y-axis and (c) z-axis, are the direction of the magnetic field applied to the circuit as shown.                              | 76 |
| <b>Figure 6.1</b> 32-channel module; (A) Block diagram, (B) photo (C) photo of 1-channel PCB.  | 78 |

|   |    |
|---|----|
| <b>Figure 6.2</b> PI model with all the parasitic components are shown. (b) PI model used for simulation .....  | 79 |
| <b>Figure 6.3</b> Scattering parameters S11 and S21 for the pi model in figure 6.2b.....  | 79 |
| <b>Figure 6.4</b> Structure of a wide-band chip-to-chip connection. Signal bump (in the center) is surrounded by 4 ground bumps. Bumps are deposited into the centers of Nb contact pads. Superconducting microstrip line (MSL) is connected to the signal bump. It has a specially shaped end overlapping a cut in the ground plane in order to provide impedance matching and increase the transmission bandwidth. .... | 81 |
| <b>Figure 6.5</b> Block diagram of the ring oscillator used for testing SFQ pulse transmission between the flip chip and the active MCM carrier. SFQ driver and receiver are marked DRV and RES, respectively.....  | 83 |
| <b>Figure 6.6</b> (a) Microphotograph of the lithographically defined bumps.(b) The complete chip-set of the multi-chip module.....   | 84 |
| <b>Figure 6.7</b> The frequency of transmission of SFQ pulses between the flip-chip and the MCM carrier in the ring oscillator at various numbers of flux quanta circulating in the ring for the typical MCM. The maximum of 16 SFQ pulses can be inserted into the ring oscillator. The speed of circulation of the pulses was controlled by varying the bias on the JTL.....  | 86 |
| <b>Figure 6.8</b> The upper and lower margins of the receiver bias current at different rates of SFQ pulse transmission between the flip-chip and the MCM carrier with Au bumps. The MSL length is 2210 $\mu\text{m}$ . The wafer was bumped using 1.8 $\mu\text{m}$ Au bumps deposited by e-beam evaporation. The MCM was bonded by a cryogenically compatible adhesive.....   | 87 |
| <b>Figure 6.9</b> The upper and lower margins of the receiver bias current vs the SFQ pulse transmission rate between the flip-chip and the MCM carrier for InSn bumps. Both the chip and the carrier were bumped by immersion in molten InSn alloy at 150 $^{\circ}\text{C}$ and bonded by reflow and a cryogenically compatible adhesive. The MSL length is 2210 $\mu\text{m}$ .....                                    | 87 |
| <b>Figure 6.10</b> The upper and lower margins of the receiver bias current vs the SFQ pulse transmission rate between the flip-chip and the MCM carrier for InSn bumps. Each separate branch from left to right corresponds to the different number of SFQ pulses circulating in the ring oscillator. A geometric resonance in the MSL at $\sim 44$ GHz can be seen. InSn bumps were used in this MCM .....              | 88 |

|                    |   |     |
|--------------------|---|-----|
| <b>Figure 7.1</b>  | A simulink Matlab model for behaviroal–level system simulation. ....  | 91  |
| <b>Figure 7.2</b>  | Spectrum for 1,2,4,8 modulators PMD ADC. ....   | 92  |
| <b>Figure 7.3</b>  | SNR(dB) versus Signal Power (dBFs) of 1,2,4,8 modulators PMD ADC. ....  | 93  |
| <b>Figure 7.4</b>  | The Layout of the transformer coil. The Number of turns $N=12$ , with primary inductance $L_{pri}=27\text{nH}$ and secondary inductance $L_{sec}=19\text{nH}$ . The inner radius, $R_i=$ , Outer radius, $R_o=$ , Width, $W=$ . (b) the 3D view of the simulated transformer( cell size $2.5 \times 2.5 \mu\text{m}$ , air $=250\mu\text{m}$ , si_substrate= $250\mu\text{m}$ , separation from ground ring and outer coil radius $75\mu\text{m}$ ). .... | 95  |
| <b>Figure 7.5</b>  | The schematic developed for the transformer based on the values extracted by simulation. ....   | 96  |
| <b>Figure 7.6</b>  | Schematic of the 5 <sup>th</sup> order Butterworth Low pass filter, $R_1=R_2=50 \text{ ohm}$ , $C_1=C_2=5.15\text{pF}$ , $L_1=L_3=4.92\text{nH}$ , $L_2=15.9\text{nH}$ . ....   | 96  |
| <b>Figure 7.7</b>  | Amplitude and phase charaternistics of a normalize 5 <sup>th</sup> order Butterworth filter . ....  | 97  |
| <b>Figure 7.8</b>  | The bilayer spiral is shown above, with $N=12$ turns. The spiral inductor is constructed with $N=6$ , in M2 and M3 layers. The 3D view of the bilayer spiral is shown above, with $N=12$ turns. The spiral inductor is constructed with $N=6$ , in M2 and M3 layers.(cell size $2.5 \times 2.5 \mu\text{m}$ , air $=250\mu\text{m}$ , si_substrate= $250\mu\text{m}$ , separation from ground ring and outer coil radius $75\mu\text{m}$ ). ....          | 98  |
| <b>Figure 7.9</b>  | The Complete Layout of the 5 <sup>th</sup> order Butterworth Low Pass filter is shown. The two capacitor are constructed between M2 and the ground layer M0. ....   | 98  |
| <b>Figure 7.10</b> | The schematic of the 4 multi-modulator PSCAN simulation . ....  | 99  |
| <b>Figure 7.11</b> | The inter modulator delay . ....  | 100 |
| <b>Figure 7.12</b> | The correct operation of the front end of the multi-modulator ADC, the differential output pulses . ....  | 101 |
| <b>Figure 7.13</b> | The complete layout constructed for the 2-modulator design . ....   | 101 |
| <b>Figure A1.1</b> | RSFQ Splitter . ....  | 114 |
| <b>Figure A1.2</b> | RSFQ Confluence buffer . ....   | 115 |

|  |     |
|--|-----|
| <b>Figure A1.3</b> RSFQ D Flip-flop .....                          | 115 |
| <b>Figure A1.4</b> RSFQ SMSL driver .....                          | 116 |
| <b>Figure A1.5</b> RSFQ SMSL receiver .....                        | 117 |
| <b>Figure A1.6 (a)</b> DC/SFQ converter (b) SFQ/DC converter ..... | 118 |

## LIST OF TABLES

|   |           |
|---|-----------|
| <b>Table 6.1 Maximum transfer rate achieved for MSL lengths with Au bumps Wafer</b>   |           |
| KL1084,.....  | 88        |
| <b>Table 6.2 Maximum transfer rate achieved for MSL lengths with InSn bumps Wafer</b> |           |
| KL1057,.....  | 88        |
| <b>Table 7.1 Inductances of spiral inductor for LC lowpass filter, .....</b>          | <b>97</b> |



## ACKNOWLEDGEMENTS

Life during my graduate studies at Stony Brook would not have been fulfilling without the guidance, support, encouragement, friendship and love of many wonderful people. I would like to take this opportunity to express my gratitude to most of them.

First of all, I would like to thank Professor Vasili Semenov for providing a very stimulating scientific environment; introducing me to the challenging problems and constantly showing new opportunities and sharing his vision of superconducting electronics, physics and technology. This dissertation would not be possible without his help and support.

I would like to thank Dr. Yuri Polyakov for teaching me all aspects of cryogenic measurements and sharing with me untold secrets of the trade of experimental procedures in physics.

Special thanks to Prof. Alex Daboli for his help and advice during the course of my studies at Stony Brook. His support has been indispensable.

I would also like to thank Prof. Harbans Dhadwal, Prof. Murali Subba Rao, Prof. Petar Djuric and Prof. John Murray for their help during my various stages of graduate studies.

I thank Prof. D. Donetski, Prof. R. Kamoua and Prof. D. V. Averin for serving as members of my defense committee.

Many people in the RSFQ Lab have provided with assistance and support during the stay and I share great memories with them. Thanks to all members of this lab for assistance at various stages: Amol Inamdar, Anubhav Sahu, Alan Rodricks, Jie Yu, Jie Ren, Girish, and Nathan Broggren.

I have made friends for life at the university in Prashant, Samrat, Abhinay, Gajendra, Abin, Clarence, Nilotpai, Ravish, Gaurav, Ashwin, Balani, Kuashal, Tobi, Gopal, Ashish, Vikas, Girish and Prasanna, with whom I share great memories. Their support, encouragement and friendship have been crucial.

I would also like to thank Prof. Sergey Tolpygo, Dr Oleg Mukhanov and Dr Deep Gupta at Hypres Inc. for fruitful discussions and Hypres Inc. fabrication team for fabricating the circuits.

I would also like to thank Dr Deborah Van Vechten for her support from the Office of Naval research.

Finally, I want to thank my parents and my brother. Without their support and understanding, I would not be here now.

# Chapter 1

## Introduction

### 1.1 Superconductivity

When a material loses all its resistance then the material is said to become superconducting. The temperature when materials lose their resistance is called critical temperature,  $T_C$ . Superconductivity was discovered by Kamerlingh Onnes in 1911 after cooling mercury (Hg), with liquid Helium (He). The field of superconductivity has now developed over the years. With the discovery of high temperature superconductivity nearly 20 years ago has given a new life into this field.

The origin of superconductivity is that below the critical temperature electrons condense into Cooper pairs, which are two electrons with opposite spins. When electrons form Cooper pairs, they no longer follow fermion statistics, because the total spin is equal to zero. Instead all the Cooper pairs condense into the same state (the superconducting condensate); thereby they can move without resistance in the superconductor. In figure 1.1(b) shows the typical distribution of electrons and Cooper pair's versus temperature. At critical temperature Cooper pairs are formed and their density grows with decreasing temperature and saturates below  $T_c$  [1, 2].

Some of the main reasons as to why the area of superconducting is attractive to electronics are very low resistance, very high frequency operation and Josephson effect. In most of the electronics application Niobium is used as the superconducting material. Its critical temperature is around 9.2k.

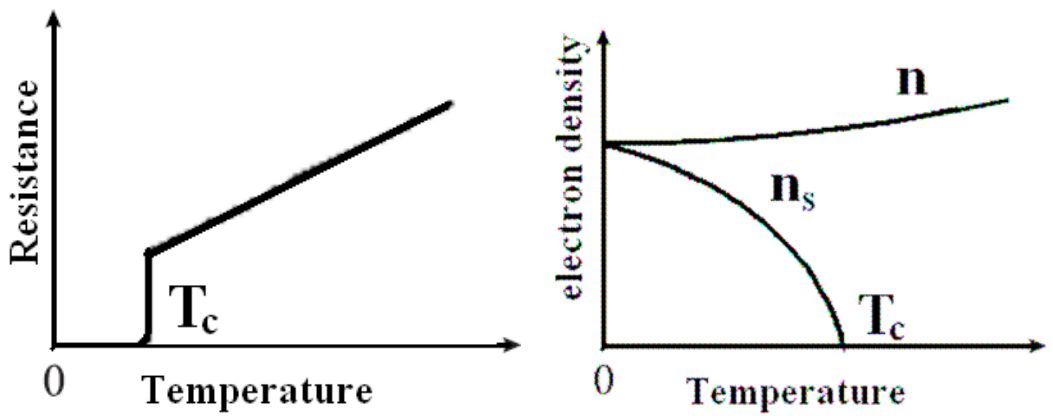


Figure 1.1: Temperature dependence of (a) resistance (b) electrons and Cooper pairs density in superconducting material

## 1.2 Josephson junction (JJ)

In superconducting electronics the active component is the Josephson junction (JJ). The Josephson effect occurs in a weak link contact between two superconducting electrodes. The main phenomena taking place in a JJ is the static and the dynamic Josephson effects.

The static Josephson (DC) effect [1,2,3,4], is the tunneling of current through a weak link without any applied voltage. The maximum possible current is limited by the critical current,  $I_c$ . Below  $I_c$  the current consists only of the super current,  $I_s$ .  $I_s$  is a function of the phase difference  $\Phi = \chi_1 - \chi_2$  of the superconducting condensate wave function between the two electrodes of the JJ. In the simplest case, this relation is sinusoidal

$$I_s = I_c \sin(\Phi) \quad (1.1)$$

The AC or dynamic Josephson effect [1,2,3,4], takes place when the current that flows through the Josephson junction is higher than the critical value,  $I > I_c$ . In case an average voltage,  $V$  exists across the junction, which gives continuous oscillations of the phase  $\Phi$  with the angular frequency  $\omega$ .

$$\omega = \dot{\phi} = \frac{2e}{\hbar} V = \frac{2\pi}{\Phi_0} \quad (1.2)$$

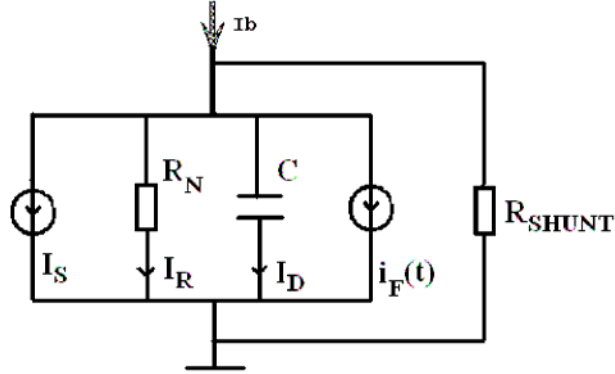


**Figure 1.2: RSJ model for Josephson junction.**

The dynamics of the Josephson junction can be explained in terms of Resistive Shunted Junction (RSJ) model as shown in figure 1.3.  $I_S$  is the super current through the junction,  $I_D$  is the displacement current through the capacitor,  $I_R$  is the resistive current through the insulating barrier and  $I_F$  is the fluctuation current.

$$I = I_S + I_N + I_D + I_F(t) = I_C \sin(\phi) + \frac{V}{R} + C \frac{dV}{dt} + I_F(t) \quad (1.3)$$

The Josephson inductance of the junction can be defined as

$$L_C = \frac{\hbar}{2eI_C}. \quad (1.4)$$

With the help of the model one can define the characteristic frequencies of the system:

Inverse relaxation time

$$\omega_C = \frac{R}{L_C} \quad (1.5)$$

and plasma frequency

$$\omega_p = \sqrt{\frac{1}{L_C C}} = \sqrt{\frac{2\pi I_C}{\Phi_0 C}}. \quad (1.6)$$

The dynamics of the Josephson junction depends on the ratio between relaxation time and plasma frequency as know as a dimensionless parameter called Stewart-McCumber parameter:

$$\beta_C = \left( \frac{\omega_C}{\omega_p} \right)^2 = \frac{2\pi}{\Phi_0} I_C R^2 C \quad (1.7)$$

The parameters of the Josephson junctions can be quite different depending on materials used and the way how Josephson junction has been formed. The most common type is the Superconductor/Insulator/Superconductor (SIS) Nb/AlOx/Nb tunnel junctions. These junctions typically have  $\beta_C \gg 1$  and I-V curve consists of two branches: superconducting branch with zero voltage and resistive branch with highly non-linear resistance. When the current exceeds the critical current, junction jumps into the resistive state with voltage equal to the gap voltage of the electrodes,

$V = 2\Delta \approx 2.6mV$ . At higher currents the voltage scale is given by the so called characteristic voltage,  $I_C R_N$ , for tunnel junctions which is about  $I_C R_N \approx \pi\Delta/2e$ . Due to the high capacitance of the barrier the I-V curve of the SIS junctions is highly hysteretic.

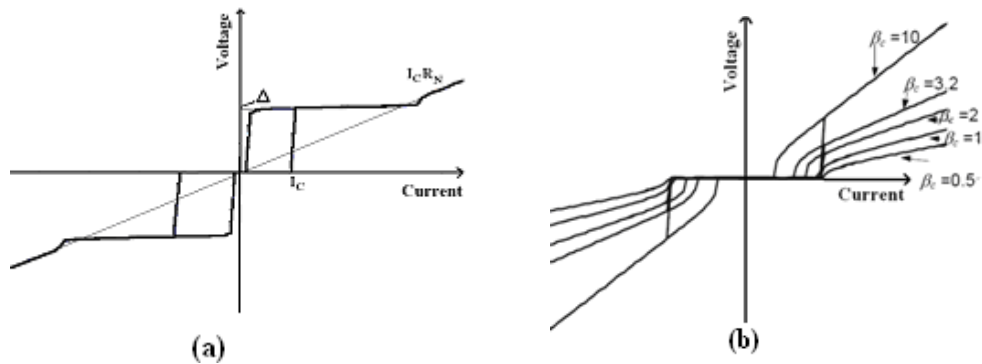


Figure 1.3: I-V characteristic for unshunted (a) and resistively shunted (b) Josephson junction.

Associated with capacitance plasma oscillations of the tunnel junction can be damped by the small shunting resistance,  $R_{SHUNT}$ , as it shown on figure 1.2. In the over-damped case with,  $R_{SHUNT} \gg R_N$ , the total resistance  $R$  in the RSJ model can be approximated by  $R_{SHUNT}$  and equation for RSJ model can be written as

$$I = I_C \sin(\phi) + \frac{\hbar}{2eR} \frac{d\phi}{dt} + \frac{\hbar C}{2e} \frac{d^2\phi}{dt^2} + I_F(t). \quad (1.8)$$

Introduction of the shunt resistor gives reduction of the  $\beta c$  and correspondingly reduction of the hysteresis on the I-V curves as it shown on figure 1.3(b). In the highly over damped case with  $\beta c < 1$  relaxation time  $\tau_N = RC$  is less than period of the plasma oscillations and switching of the junction into the resistive state gives periodic tray of the Single Flux Quantum (SFQ) voltage pulses with the area

$$\int V(t)dt \cong \Phi_0 = \frac{\pi\hbar}{e} = 2.07 \times 10^{-15} \text{ Wb}, \quad (1.9)$$

and the dissipated energy is

$$W = \int IV(t)dt \cong I_C \Phi_0. \quad (1.10)$$

For fixed  $\beta c$ , the characteristic voltage  $I_C R$  and switching time  $\tau_C$  of the over damped junctions depends on a critical current density  $J_C$  available at the fabrication process:

$$I_C R = \sqrt{\frac{\Phi_0 J_C}{2\pi C_j \beta_C}}, \quad (1.11)$$

$$\tau_c \cong \frac{\Phi_0}{2I_C R_N} = \pi \frac{L_C}{R} = \frac{\pi}{\omega_p} \alpha \sqrt{\frac{C}{I_C}} = \sqrt{\frac{C_j}{J_C}}. \quad (1.12)$$

For the typical range of the critical current densities in the currently available processes between 30A/cm<sup>2</sup> and 20KA/cm<sup>2</sup> the switching time is in the range from 10 to 0.05ps and energy dissipated per one single switching event is in the range from 10<sup>-20</sup> to 10<sup>-17</sup> J.

### 1.3 Flux quantization

Magnetic flux quantization forms the basis of data encoding in RSFQ technology [8,9,18]. Given area A, flux of the magnetic field B is an integral multiple of magnetic flux quantum  $\Phi_0$ .

$$\Phi = \int B dA \quad (1.13)$$

$$\Phi_0 = \frac{h}{2e} = 2.0678 \times 10^{-15}$$

According to [8,9,18], the data encoding for the SFQ logic is stated as “arrival of SFQ pulse at a terminal of an elementary cell during the current clock period indicates the binary value 1, while the absence of the voltage pulse is 0. “

The above property can also be used to relate the phase drop across the junction. If the total flux in the superconducting loop is  $\Phi$ , and the loop is interrupted by a Josephson junction (as in a single junction interferometer, figure 1.4) then the phase difference  $\phi$  across the junction is given by

$$\phi = 2\pi \frac{\Phi}{\Phi_0}. \quad (1.14)$$



## 1.4 Generation of Flux Quanta

SFQ pulses can be generated a single junction interferometer [8,9]. It can be described as a superconducting closed loop with two leads and interrupted by a Josephson junction. The total flux  $\Phi$  generated by the total current (internal and external)

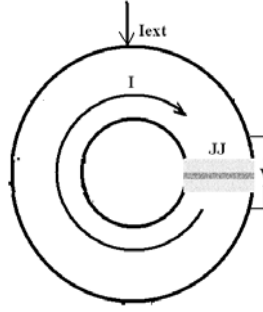


**Figure1.4: A single junction interferometer.**

$$\phi = \phi_{ext} + \phi_{int} = MI_{ext} - LI \quad (1.15)$$

We can see that the total flux can be fixed by applying an external current to introduce a phase difference. At a higher value of the external current the voltage pulse is produced (in accordance with Faraday's law, rate of change of flux result in the generation of voltage). The shape of the voltage pulse is very close to that of a Gaussian. But the voltage pulse must satisfy the constraints of eq. 1.9. In other words the change of flux through the interferometer is exactly one magnetic flux quantum.

## 1.5 RSFQ Circuits

The Meisner effect [1,2,3,4,6] and Josephson effect form the basis for of superconducting digital electronics. These effects allow storing information in the form of one single flux quanta and transferring them at high speeds via switching of Josephson junctions in the networks.

Rapid single flux quantum technology (RSFQ) was introduced in 1985 [8,9] suggesting a new approach to the existing Josephson junction digital computing. In

RSFQ the binary state is not presented by the DC voltage state of the gates but by magnetic flux quanta expressed in very short voltage pulses. Emanating from the properties of the overdamped Josephson junction, the following section introduces to the principles of the technology and basic circuit elements of RSFQ circuits.

### 1.5.1 Principle Components of RSFQ circuits

In figure 1.5, the basic idea of RSFQ is presented: to pass the information about the flux state from one loop to another using the dynamics of the flux transients [7,8,9]. A  $2\pi$  jump in Josephson phase  $\Phi$  across the junction corresponds to one flux quantum passing through the junction.

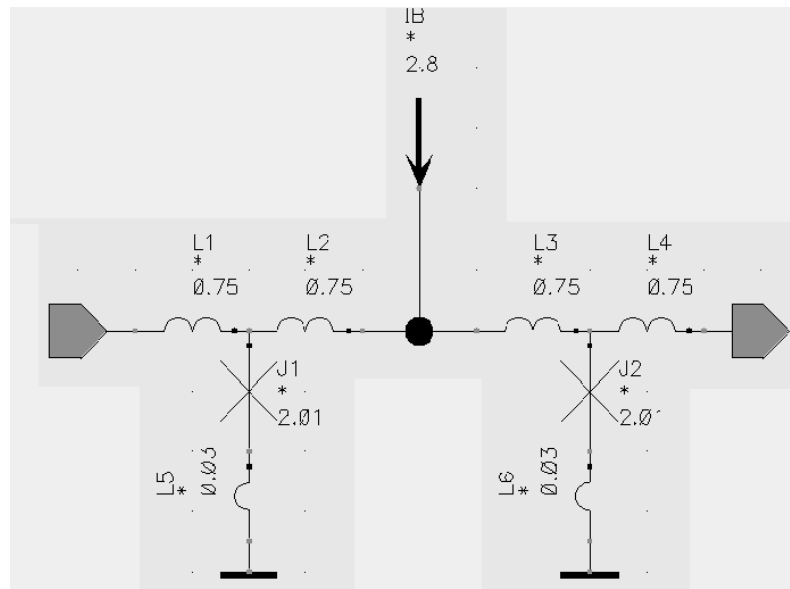


**Figure1.5: A Josephson transmission line (JTL), where single flux quantum is transferred through J1 by entering J1-L2-L3-J2.**

Figure 1.5 has many essential elements of a typical RSFQ circuit; overdamped Josephson junctions J1 and J2 break the superconducting loop formed by inductances L2, L3 and the ground plane. Both junctions are biased by current source  $I_B$  so that the current flowing through each junction is close but smaller than the critical value  $I_c$ . A flux quantum arriving from the input “in” (from the left) of the circuit drives the current

through the junction J1 above the critical value and for a short time, of the order 5ps, a voltage pulse is formed across the junction J1.

After the junction J1 returns to the superconducting state, the flux quantum is trapped inside the loop J1-L2-L3-J2 ground plane loop. What happens next is determined by the parameters of the circuits. If the inductance of the loop L2+L3 is large enough, so that the induced change in current  $\Delta I$  through the junction J2 ( $\Delta I \sim \Phi/L1$ ) is not sufficient to exceed its critical value, the state with a trapped flux is stable and the loop stores the information. If the inductance of the loop is smaller, so that current through the junction J2 exceeds its critical value, the junction flips, making a  $2\pi$  turn in phase  $\Phi$  and the flux quantum leaves the loop through J2 in the same manner as it entered it through J1.

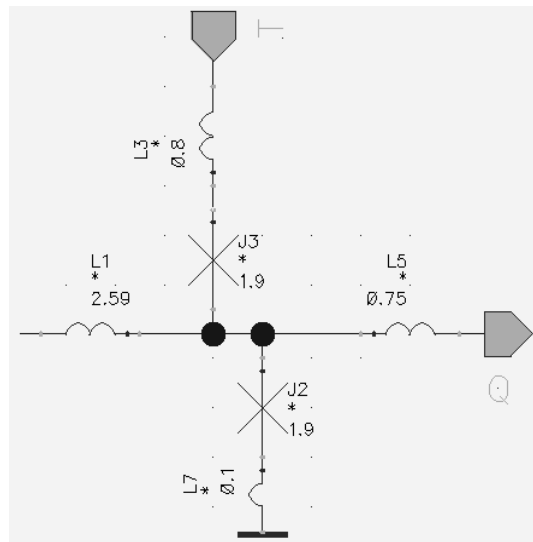


**Figure1.6: Two Junction Comparator**

The other basic idea of RSFQ is using a two junction comparator, as shown in figure 1.6, controlled by a quantizing inductance L1. The parameters of the circuit are chosen so that when an SFQ voltage pulse arrives at the two terminals input and “T”, the flux stored in the loop to the left of the junction J2 is released and appears on the output. When there is no stored flux, the current through J2 is smaller and further from its critical

value so with the arrival of the two read terminal of the pulse junction J3 flips and there is no output. Two junction comparators are the basis of every RSFQ design.

## **1.6 Large Scale Integration of Superconducting Circuits**

Superconducting SFQ electronics is a unique technology, that delivers the fastest digital circuits with extremely low energy dissipation [7, 10, 60]. But it is still an emerging technology and as a result it is very easy to compile a list of technical problems that remain to be solved.

Flux trapping, power dissipation, heat dissipation, integration of MCM and returning path of ground currents [71] are some of the crucial problems in the technological development aspects that must be overcome to increase the prospects of large scale integration of RSFQ circuits. Today, circuits of over 20,000 Josephson junctions have been reported [11,63,70, 80] and circuits of 5000 Josephson junctions have been tested at high speeds up to 80GHz [61,68,86,87].

In this thesis, integrated test circuits have been fabricated and tested that contain nearly 2000 Josephson junctions. The goal is to use test results from these circuits investigated to resolve the difficulties that arises in the design of large SFQ circuits. The area of development of smaller cryogenic coolers is also necessary to make RSFQ technology more easily accessible, but this area is beyond scope of discussion here.

### **1.6.1 Motivation**

In this thesis, we would like to address some of the most important aspects of RSFQ circuit technology for large scale integration.

### **1.6.1.1 Flux trapping**

Josephson junction circuits are highly sensitive to magnetic fields. This sensitivity derives from the small size of the magnetic flux quantum; one flux quantum is equivalent to  $2 \times 10^{-7}$  gauss in a  $1\text{-cm}^2$  area. (The magnetic field of the earth is  $\sim 0.4$  gauss.) JJ circuits are shielded from local magnetic fields, such as the earth's field, by high permeability shields. The field inside "good" shields can be as low as a few milligauss. Flux trapping occurs at unpredictable locations in superconducting films as they are cooled through their superconducting transition temperature,  $T_c$ . The flux is trapped in the films, in the form of Abrikosov vortices [1,6], where superconductivity in that region is lost and has magnetic field lines penetrating the film. Flux trapped in ground planes can significantly affect working of a SFQ circuits, from reducing the operating margins to completely rendering the circuit inoperable. One method for alleviating this effect is to intentionally trap the flux in holes (called moats) placed in the ground plane, such that circuit operation is not affected. There is no standard system for designing and locating moats.

### **1.6.1.2. Low power RSFQ circuit- Power independent RSFQ cell**

Even though the power dissipation in RSFQ circuits is low, it is relatively high for the temperature of 4.2K. The prospects of RSFQ circuits have now expanded largely from digital logic to realization of fast superconducting digital computers [13,53,54,61,67]. The wide range of circuits makes it the reason for different power requirements for the systems. A good system designed for any application is desired to have minimum or no static power dissipation, which are high in RSFQ circuits.

### **1.6.1.3. Current Biasing of RSFQ circuits:**

Chips with a large number of junctions require large bias currents. Even assuming all JJs are at minimum IC of 100  $\mu$ A, a  $10^6$ -JJ chip will require 100A. Efficient methods of supplying bias current to the circuit components on-chip have to be demonstrated for large scale circuits. A method to bias large circuit blocks in series (referred to as current recycling or current re-use) will be essential for large junction-count chips in order to reduce the total current supplied to the chip to a manageable value. Both capacitive and inductive methods of current recycling have been demonstrated at a small scale (fewer than 100 junctions) [56,57,58]. Current recycling can reduce the heat load in the power lines into the cryostat, but does not eliminate the on-chip static power dissipation.

### **1.6.1.4 Multi-chip modules:**

To develop large scale RSFQ circuits, one of the convenient methods is using flip-chip technology [55,59,86,87,89]. Flip chip technology [85] has been used for many years in semiconductor technology, but in superconducting electronics they have enjoyed lower success. One of the fundamental limitations is the low quality (high parasitic inductance and capacitance) of the high frequency bumps of the flip chip. The high parasitics of the bumps lower the limit of the transmission rate between the two bonded superconducting chips. The transfer rate between the bonded superconducting chips must be able comparable to the operating speed of on-chip components which above 100GHz.

### **1.6.1.5 Multi-modulator ADC design**

Superconducting Modulators have been demonstrated for high quality [11]. But one of the limitations has been due to the noisy nature of the front end of the ADC [14]. To overcome the limitation and improve the SNR and dynamic range, the number of

modulators can be increased and also the design of the pickup coil transformer should be improved. A possible incorporation of a low pass filter will improve the operation.

## **1.7 Contributions**

### **1.7.1 Flux Trapping**

-An empirical model has been presented for analyzing parasitic flux trapping in superconducting circuits.

-A quantitative analysis of the effect parasitic flux trapping on the operation of RSFQ circuits has been studied using shift registers. The method was also used in determining: fabrication spread, probability of flux trapping in circuits, effect of flux trapping on bias of the circuit, and locating defective cells in RSFQ circuits (which can limit the operating margin of the entire circuit)[44].

-A complete experimental setup and methodology, with 3D magnetic field control, has been developed for investigating parasitic flux trapping in cryo-coolers and Helium Dewars. The setup can be used to study flux trapping in other superconducting digital circuits [44].

-A new set of moat protocols were also studied for parasitic flux trapping to determine the layout configuration which are most resistant to parasitic flux trapping. The most resistant moat configuration has been able to prevent flux trapping upto 20mG, which is comparable to Earth's magnetic field [45].

-Flux trapping studies have also been carried out on the power independent circuits, a logic family for power independence [48].

### **1.7.2 Low Power RSFQ circuits**

-A new concept of low power superconducting circuits, power independent RSFQ cell was developed. The power independent logic circuits are able to retain logic state of the circuit, when the bias power is switched off. So, the power independent circuits can be biased only when the circuits are needed for operation and switched off the remaining period of time, eliminating static power dissipation. The logic was incorporated into shift register design, fabricated and experimentally tested with  $\pm 20\%$  margins. The concept was demonstrated using a 6bit counter shift register in both  $1\text{kA}/\text{cm}^2$  and  $4.5\text{kA}/\text{cm}^2$  [49].

### **1.7.3 Current Cycling in RSFQ Circuits**

-Current recycling has been implemented and tested to reduce current bias to the circuit. The principle of the method is to reuse current from one part of the circuit to bias another part; it is possible to the lossless nature of the superconducting devices. The technique was successfully demonstrated for a digital transmission line with over 1000 junctions on the chip.

-The technique of current recycling was also used to develop high frequency output drivers for SFQ circuits I/O interfaces.

-The impact of magnetic field on the operating margins was also studied on the current recycling circuits. The methodology of experiments we were also able to study the physical structure of the fabricated circuits.

### **1.7.4 Multi-Chip Modules**

-We were able to successfully demonstrate the digital data transfer at over 110 GHz by using a newly designed bump structure for connecting the two superconducting chips. The bump structure has parasitic reduced, thereby increasing the resonant frequency to



75GHz [47].

### **1.7.5 Multi-Modulator ADC Design**

-A design of the architecture for Multi-modulator with low noise and high sensitivity front end has been presented.

-New dipole transformer has been developed for low noise and high tolerance to external magnetic fields.

## **1.8 Limitations**

### **1.8.1 Flux Trapping**

-The fundamental limitation of the method used for quantifying the effect of flux trapping effects on the circuits is that our circuit has to operate correctly. The exact location of the flux frozen cannot be determined by our method. Also the probability of flux trapping, determined for each cell, will depend on the number of measurements carried out as the results are quantitative in nature.

### **1.8.2 Low Power RSFQ circuit- Power independent RSFQ cell**

-The power independent circuits have to be turned on every time when we wish to execute the circuits to perform a function. The circuits also have large inductances and hence occupy larger area of than the corresponding conventional RSFQ cells.

### **1.8.3 Current Recycling in RSFQ Circuits**

-The circuits are implemented on floating grounds and susceptible to larger transients, and so must have filters to lower these transients in serial biasing circuits. Even though they lower total current applied to the chip, the on chip dissipation is not reduced. The area of the current recycling circuits is also larger due to the additional circuits used to implement this technique, a driver and receiver must be attached to each block biased by

current recycling.

-The circuits using inductive biasing are more sensitive to magnetic field than the conventional biasing due to the use of larger number of transformers involved. The transformers can couple with remanent magnetic fields can affect the operation.

-If capacitive coupling is used in the technique, the area occupied by capacitors is going to very high compared to the area otherwise occupied.

#### **1.8.4 Multi-Chip Modules**

-The multichip modules bumps have higher resonating frequency but it is still within the operating range of the frequency and reduces the operating margins of circuits. Better bonding techniques will improve yield of the multi-chip modules.

#### **1.8.5 Multi-Modulator ADC**

-The task of synchronization is greatly increased and additional circuitry has to be developed for this purpose. Also, impact of jitter in the ADCs have not been addressed which are widely responsible for lower dynamic range and SNR.

## Chapter 2

### Flux trapping in Superconducting Circuits: theory and experiments

#### 2.1 Introduction

Magnetic flux gets trapped during cooling below transition temperature,  $T_c$ , in superconducting films and causes serious problems for superconducting devices such as operation errors [19,44,45]. The problem of flux trapping is uniquely existent only in superconducting circuits. However, since flux trapping is unique to superconductor electronics and its solution cannot be acquired from another branch of microelectronics. The closest analogy to this problem in conventional semiconductor technology is the sensitivity of circuits to elementary particles that affect the circuits during their operation

#### 2.2 Theoretical Facts

Discussions of flux trapping are almost as old as Josephson junction technologies. For example, good observations of flux trapping in narrow films and wide ground planes were originally reported in 1982 [20] (see also discussion in [32]). Holes in the ground plane of the superconducting circuits known as Moats, reduces the impact of flux trapping of Josephson junction circuits were suggested and experimentally investigated [21].

The physics of flux trapping after [20] is as follows: “As the film temperature  $T$  approaches  $T_c$ , small areas of superconductivity began to appear. As  $T$  decrease further, these areas grow larger, and new ones appear, and the superconducting areas begin to join up. ... As the superconducting areas join up, however, some normal areas will become surrounded entirely. As this occurs the flux within the normal area will adjust to the nearest integer number of quanta. Thus only if there is more than  $1/2\Phi_0$  threading the

normal region will a vortex be trapped in this region.”

The physics of moats in wide superconducting films is explained in [21,22,35,36, 45,72]. The effect of moat pattern on flux trapping is presented in chapter 3. In this chapter a review of the general properties of a vortex in a superconducting film is presented that will help in determining the effect of vortices on superconducting circuits. Force  $F$ , applied to a vortex can be presented as the gradient of vortex energy  $E$ :

$$F = \nabla E \quad \text{or} \quad F = dE / dx. \quad (2.1)$$

The energy  $E$ , in turn can be split into terms  $E_k$  and  $E_m$  with very different properties. Term  $E_k$ , describes the energy concentrated within the film in the tiny vortex kernel bordered by the larger of 2 characteristic lengths  $\xi$  (coherence length) and  $\lambda$  (London penetration depth) [1,2,6]. Each of them depends on factors such as temperature, film substance, deposition processes and internal stress in the film. It is important to note that a short range pinning forces is defined by local variations of  $\xi$  and  $\lambda$  as well as film thickness,  $d$ .

Term  $E_m$ , describes the energy of magnetic field  $H$ , outside the vortex kernel. This energy term is responsible for the long range interactions of the vortex with other vortices, edges of the film and external magnetic field. Energy  $E_m$ , (in contrast to  $E_k$ ) is universal and can be accurately calculated for different film geometries. For example, in endless films, field  $H$ , is spherically symmetric and attenuates inversely proportional to the squared distance from the kernel  $r$ :

$$H(r) = \Phi_0 / \mu_0 2\pi \cdot r^2. \quad (2.2)$$

$E_m$  is as

$$E_m = 1/2 \int \vec{B}(r) \cdot \vec{H}(r) dv. \quad (2.3)$$

and  $B = \mu\mu_0 H$ . All magnetic vortex interactions can be reduced to the calculation of Lorentz force between the vortex holding magnetic flux,  $\Phi_0$  and surface current with linear density of,  $J_H$  flowing in the vicinity of the vortex kernel (see [25,26]):

$$F = \vec{J}_H \times \vec{\Phi}_0 / c. \quad (2.4)$$

In thick films ( $t \gg \lambda$ ), it is more convenient to analyze two independent currents  $j_{Hi}$  ( $i=1, 2$ ) flowing along the upper and lower film surfaces. The values of these currents are numerically equal (but orthogonal) to corresponding magnetic fields  $H_i$ :

$$j_{Hi} = H_i. \quad (2.5)$$

Using the equations from above, the interaction of two vortices located at distance  $d$  from each other directly follows from (2.2), (2.4) and (2.5):

$$F = \pm \Phi_0^2 / 2\pi\mu_0 d^2 \quad (2.6)$$

Where negative and positive signs correspond accordingly to co- and counter orientations of the fields in the vortices.

To calculate the interaction of the vortex with the perpendicular magnetic field, it is enough to find the distribution of surface currents induced by this field and to use this distribution in eq. 2.4. Finally, the interaction of a vortex with the straight edge of the film can be explained in terms of the vortex interaction with its mirrored image. We can verify that the distribution of surface currents induced by one vortex located at distance,  $d$ , from the straight edge of the film coincides with those caused by two counter oriented vortices remote from each other at distance,  $2d$ . Identical current (and therefore fields) distributions definitely lead to equal attraction forces (2.6) for both geometries.

The presented theory allows, for example, the calculation of the perpendicular magnetic field,  $B_C$ , critical for the entrance of vortices into a superconducting strip with

width,  $w$ . Experimental results support the relationship ( $B_c \sim 1/w^2$ ), as reported in [23]. Later references to a similar formula containing an accurate numerical factor can be found in [4,24,39]:

$$B_c = \pi\Phi_0 / 4w^2. \quad (2.7)$$

This universal formula takes into account only the external (or magnetic) vortex energy  $E_m$ , but it gives a very reasonable match for the known experiments with Nb, PbIn and PbAu films [23].

### 2.3 Numerical Simulations of Magnetic Force on Vortices

According to eq. (2.7) a large ground plane film with  $w \sim 5$  mm would give a low-critical field. In other words, a low magnetic field initiates the entrance of numerous vortices. However, each vortex that enters the film decreases the external field and in equilibrium the entered vortices completely compensate for the external field. In other words, for wide films the effect of the external field can be reduced to the collective multi-vortex interactions. As mentioned above, it is well known that the undesirable drift of vortices along the film can be prevented by moats that “catch” those vortices, converting them into magnetic flux permanently frozen in the hole.

For single layer structures, the effect of long moats can be estimated with ease. The vortex located near a moat “sees” its boundary as the straight edge of the film. As we mentioned above, the vortex is attracted to this edge according to (2.6) with effective  $d$  that is twice as long as the real distance to the edge. If this force exceeds the pinning force then the vortex falls into the moat; the banks of the moat are vortex free.

The borders of guarded areas can be described as lines where the attraction force between a virtual vortex and the moat equals the pinning force. If the film is uniform for

pinning forces then the borders of the guarded areas coincide with the corresponding line of equal attraction forces. These lines can be numerically calculated using the 3D-MLSI package [27,28] developed for calculation of self and mutual inductances of superconducting film structures. This is possible due to the duality between the magnetic energy and inductance of a hole  $L$  with a frozen vortex:

$$E = \Phi_0^2 / 2L \quad (2.8)$$

eq. (2.8) implicitly connects the force (2.1) with a dependence of the inductance on its position in the film. For example, the circular hole centered at point  $x$  moves toward the film edge with coordinate  $x=0$ . According to (2.1) and (2.6) we can find that

$$E(x) = \int_{x'} F(x') dx' = (\Phi_0^2 / 2)(1 / \mu_0 D - 1 / 4\pi x) \quad (2.9)$$

The first term here is the integration constant selected to satisfy Ketchen's formula  $L = \mu_0 D$  for the inductance of a circular hole with diameter,  $D$  [29]. Now generalized formula for hole with center distance  $d \gg D/2$  from the film edge:

$$1/L = 1/\mu_0 D - 1/4\pi d. \quad (2.10)$$

Note that the force is proportional according to first derivatives of eq. (2.9) and eq. (2.10) does not depend on hole diameter,  $D$ . As a result, the parameter is relatively free and can be chosen to optimize the accuracy of numerical simulations.

Typical simulation results using the 3D-MLSI package are shown in figure 2.1. The figure shows a distribution of the surface currents in the film with the hole imitating a virtual vortex and the real moat.

Inductance calculations for numerous positions of the virtual vortex and mapped the attraction forces were calculated to find the gradients of reversed inductances of the

hole. These results were further used for the moat design in chapter 3.

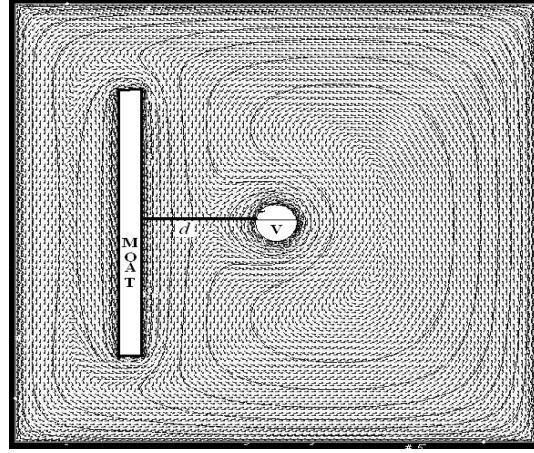


**Figure 2.1** Distribution of surface currents in superconducting film with a circular virtual (or probe) hole  $v$  and a moat. The currents are induced by flux frozen in circular hole

## 2.4 How Trapped Flux Affects Circuits

The frozen flux can affect the superconducting circuits by two different mechanisms: It can either directly penetrates into Josephson junctions or it can be coupled with the magneto-sensitive gates.

Josephson junctions are relatively small and therefore their properties will be affected only if the vortices are frozen in junction electrodes [31]. This effect is minimal if vortices penetrated both electrodes and are well aligned. In this case, the effective area of the Josephson junction is reduced only on  $\sim \xi^2$ . The area becomes much larger ( $\sim a^2$ ) if the vortices in the upper and counter electrodes are mutually misaligned at a distance,  $a$ . The effect will be catastrophic if the vortex is frozen only in one electrode. In this case, the magnetic field of the vortex covers a significant fraction of the junction area causing the critical currents of the Josephson junctions to be dramatically affected by the frozen vortices. The probability of such an event is very low as indicated by eq. (2.7). This



equation shows that small junction electrodes have high critical fields. The probability of the damaging effect increases if the base electrode is much larger than the junction area, or if the base electrode is strongly coupled to the practically endless ground plane.

The magnetic coupling of the frozen vortices with RSFQ devices or any other magnetically sensitive gates is much more common than the first mechanism discussed above. This is because even flux trapped in the moats would also be coupled with gate components; i.e., it is difficult to completely eliminate coupling circuits with frozen flux. It is more realistic to try to reduce this coupling. 3D-MLSI package [27,28] has been used to estimate the coupling vortex and RSFQ circuit components, which is about  $0.2\Phi_0$ .

## **2.5 RSFQ Circuits for Flux Trapping Experiments**

Shift register developed in [32] has been used to study flux trapping in RSFQ circuits. The important feature of D cells is an additional bias terminal probe connected with a separate power line (figure. 2.2). A nominal bias voltage applied to the line is zero which does not affect the circuit operation. However, a voltage was applied and the margins were measured for normal circuit operation.

### **2.5.1 Measurement Process:**

The measurement procedure is as follows: First that the whole circuit is checked if it is completely operational for at least one set of bias voltages. This set of bias was used to write into the register a digital code containing many logic “0”s and logic “1” that selects the investigated cell. The selection takes place due to a large circulating current (figure 2a) in the storage loop. This current affects the margin of the cell for probe current. At the same time the margin was affected by the current induced by flux frozen in the vicinity of the loop.

The operating margins were measured by numerous times for correct cell operation at different values of the probe voltage. The test result was extracted by returning to the nominal set of biases and reading out the content of the whole register. The circuit was capable of operating as a collection of digital SQUIDs. The complete measurement cycle is operated for a number of sophisticated sequence of data and clock pulses as well as variation of bias voltages. The OCTOPUX setup [33] was for the entire measurement procedure.

Another shift register technique [42] requires some extra hardware but in return dramatically simplified the testing procedure.

## **2.6 Experimental Setups**

Two experimental setups were used for the experiments. One of them was based on 0.5 W 2-stage close-cycle refrigerator “Coolpower 4.2GM” from Leybold Cryogenics. For testing a superconducting circuits we developed a special cold head (figure. 2.4) providing about a 5.2 K operation temperature. The other setup is our chip holder immersed in a commercial Helium Dewar (4.2 K). In both setups, thermo-cycling or “defluxing” procedure (the chip is heated above critical temperature to expel the frozen flux and then allowed to cool) was provided under OCTOPUX control using off-chip heaters and thermometers. Additionally, the chip temperature was measured by the observation of the transition into the superconducting state of Niobium strips located on the chips but not involved in the operation of the investigated circuit. (Each test chip contains two similar shift registers). The figure 2.4(b) shows the 3D Helmholtz coil arrangement for providing magnetic field during the experimentation.

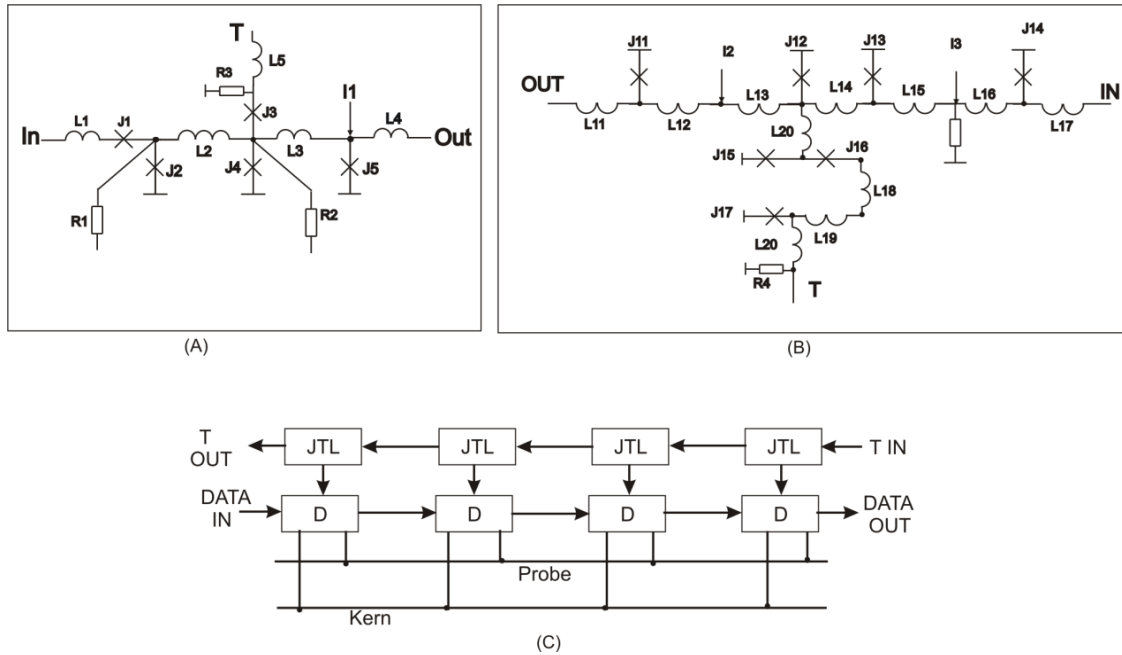


Figure 2.2: Structure of the counter-flow shift register consisting of D cells (a) and timing JTL splitters (b). Note that D cells have extra current terminals (Probe) connected with the separate power line with zero nominal bias voltage

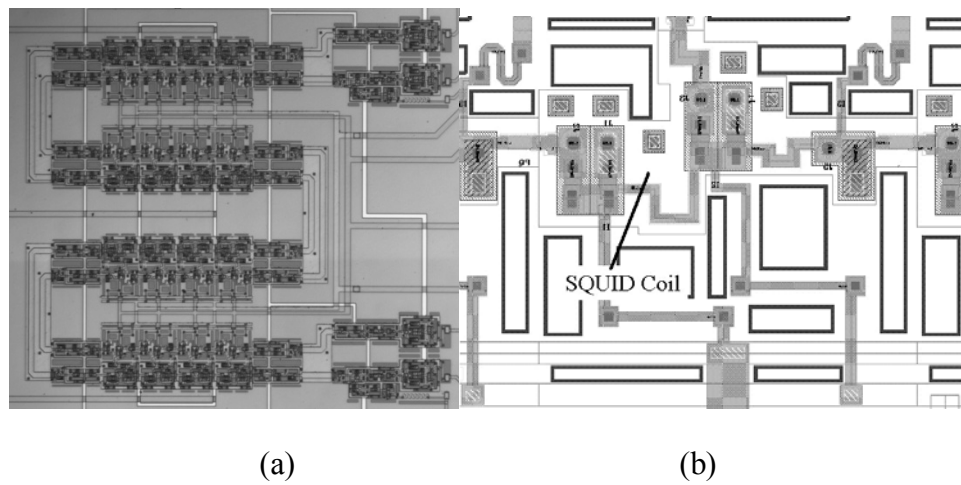
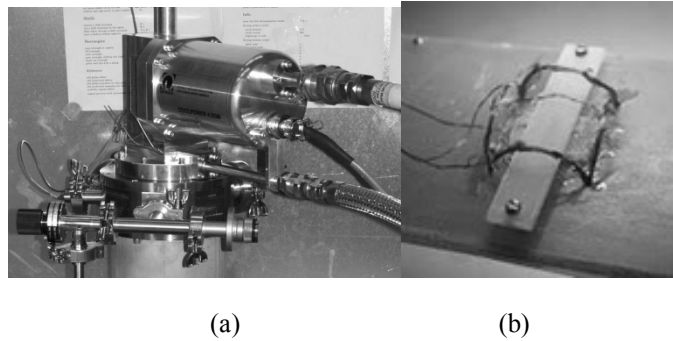


Figure 2.3: Layout of the test circuit (a) and one of D cells (b). Solid black lines show holes (moats) in the lower ground plane

Margins for the current probe usually measured with about  $0.5 \mu\text{A}$  accuracy. This accuracy was achieved due to averaging over about 50 to 1,000 primitive measurements (for details see [13]). About 50 thermo-cycles at each of the different values of intentionally applied magnetic fields in both normal and tangential directions.



**Figure 2.4: (a)Cold head of the Cryo-cooler(b)3D Helmholtz coil setup**

## **2.7 Analysis of Experimental Results**

### **2.7.1 Global Analysis of the circuit**

As we already mentioned after each thermo-cycle, circuit operation as a shift register is checked. It can be seen that the probability of incorrect operations depends on the applied magnetic field.

In figure 2.5 the lower and upper margins for 5 independent bias voltages is shown. Four upper plots (starting from the top one) illustrate margins for DC/SFQ and SFQ/DC converters, timing JTL/splitters, micro-strip interfaces and finally the conventional D cell biases. They are important for comparison of flux trapping sensitivities of mentioned circuit components. However, below we will focus only on the probe bias margins shown as the lowest plot in figure 2.5.

The horizontal coordinate for all plots is the applied magnetic field. The stripes (pink color) in the middle of the plots mark the “restricted” zone where the margins are

too low for reliable investigation. As a result, all experimental points within the stripes are eliminated from the circuit analysis.

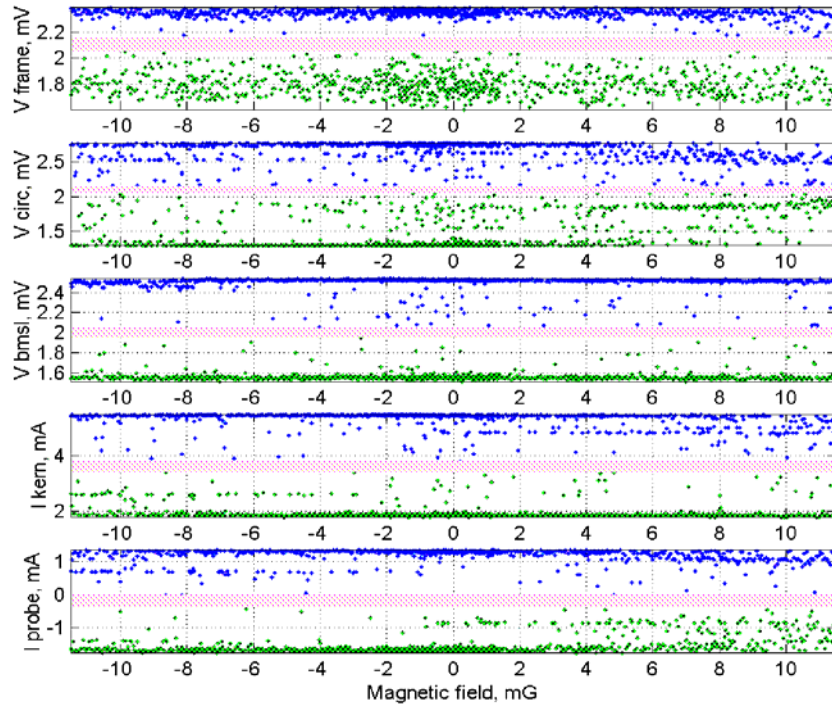


**Figure 2.5: Spread of upper and lower are bias margins for major components of the test circuit. The stripes show the minimal margins required for further testing of individual cells.**

## 2.7.2 Margins of Individual D Cells

Earlier it was described in the procedure that allows extracting margins for any of 16 D flip-flop cells. Figure 2.7 shows upper margins for each of the 16 measured cells. First, the fabrication spread is extremely low (about  $\pm 5 \mu\text{A}$ ). The shift register is organized as 4 groups of 4-bit registers (figure. 2.3a) connected by micro-strip lines, showing the deviations are mostly due to different positions of cells in the register. The plot shows that the pure fabrication spread within the same positions in different groups is below  $\pm 2 \mu\text{A}$ . This is a very interesting observation as it shows “design induced”

spread pattern

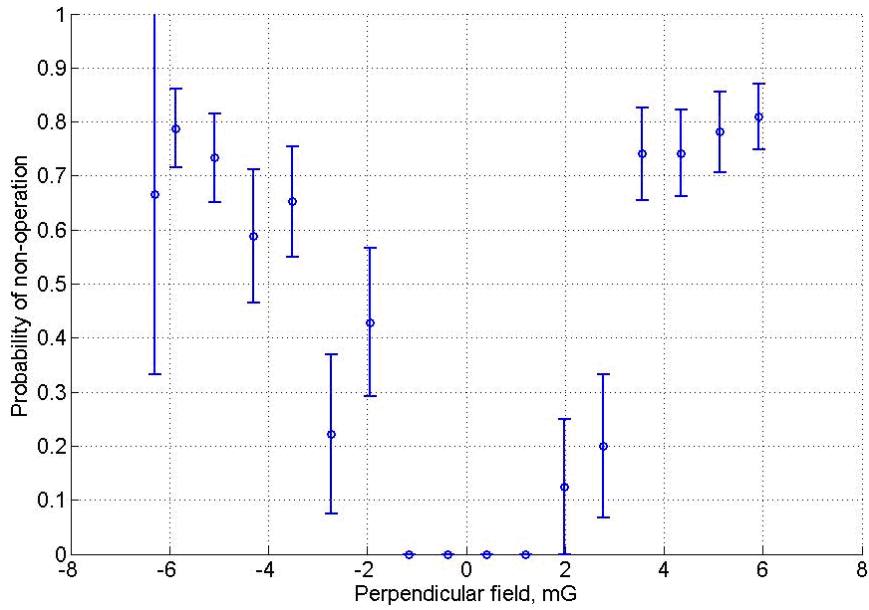


Figure 2.6: The probability of too narrow margins or incorrect operation at different perpendicular magnetic fields

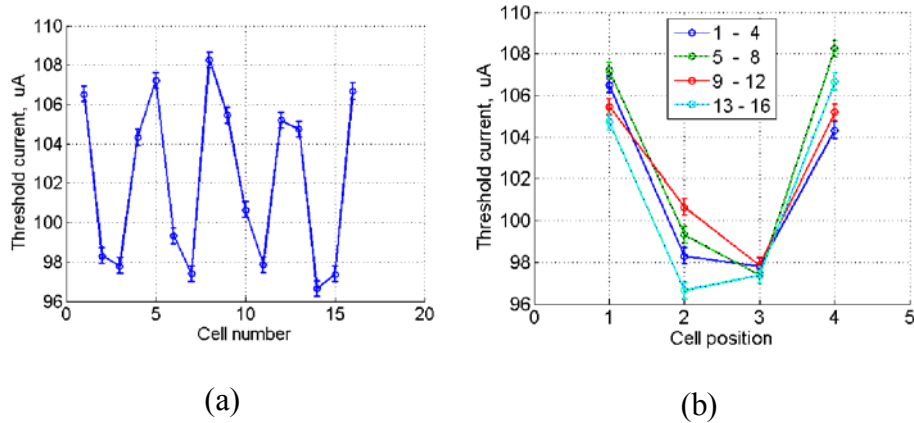


Figure 2.7: Margins of D cells not affected by trapped flux. (a) Shows margins for 16 individual cells. (b) Shows the same data but “convolved” position of cells in four groups of 4-bit shift registers

It is easy to see that at lower fields (below 3 mG) there are no noticeable flux-trapping induced deviations of the margins. The probability of flux trapping increases with magnetic field. However the dominant effect here is caused mostly by the flux

trapping in cell #13. Moreover, the flux trapping in this cell always causes the same margin deviations (+ 32  $\mu\text{A}$  at negative fields and -32  $\mu\text{A}$  at positive fields).

Measured deviations of margins for each cell into 3 groups: small deviations (below 4  $\mu\text{A}$ ), medium deviations (4  $\mu\text{A}$  to 20  $\mu\text{A}$ ) and large deviations (more than 20  $\mu\text{A}$ ). Figure 2.9 shows the deviation due to the field applied in the normal direction and the figure 2.10 deviation probability as a function of parallel field.

Another interpretation of the probability of deviation is shown in figure 2.11. The probability of events within each group is marked by circles of corresponding size. These deviations are caused either by flux frozen in moats located close to the cells or in remote timing JTLs. (In the latter case the flux affects the propagating delay that in turn affects the operation margins.) Only few of the several cells are affected by flux trapping. This is especially true for the large margins deviations. More specifically, only one cell (#13) shows the dramatic impact of flux trapping. There are 9 more cells that have been affected at least one time. The rest 6 cells have not been affected at all. The variation of flux trapping from cell to cell indicates its close connection with microscopic fabrication imperfections. This is a positive observation because technological imperfections are easier to overcome than fundamental limitations.

## **2.8 Discussion**

The influence of flux trapping on the operation of RSFQ cells has been evaluated using PSCAN [18], 3dMLSI and other models. A complete methodology to study the effects of flux trapping in superconducting circuits was established. The experiments of flux trapping were carried out in both in a closed-cycle setup and measured several other chips using both the cryo-cooler and Dewar setups. We were able to establish that the

worst case coupling between a vortex and the circuit component was about  $0.2 \Phi_0$ . The perpendicular magnetic field only significantly affects the circuits in flux trapping with tangential magnetic fields not contributing. The established experimental methodology also can be used to determine defective cells. This measurement technique complements SQUID visualization techniques [34,35,36,52].

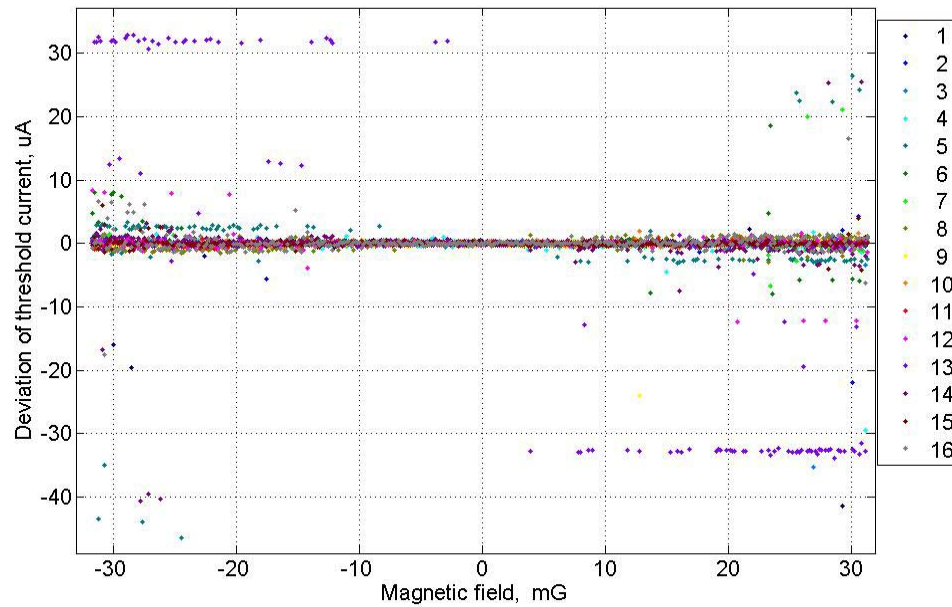


**Figure 2.8** Deviations of threshold current for all 16 cells repeatedly measured at different magnetic fields.



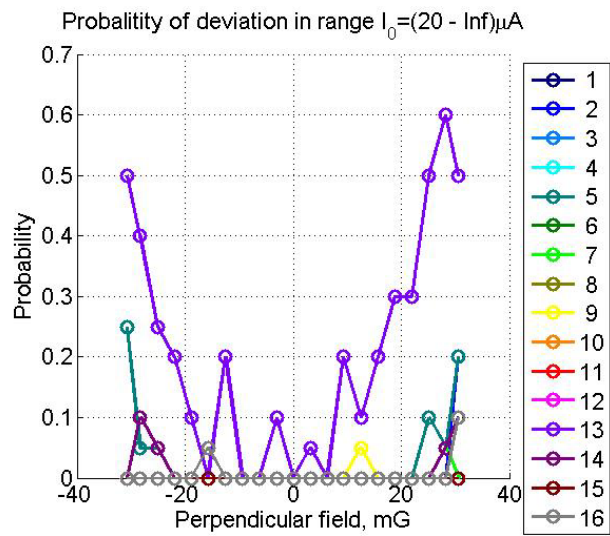
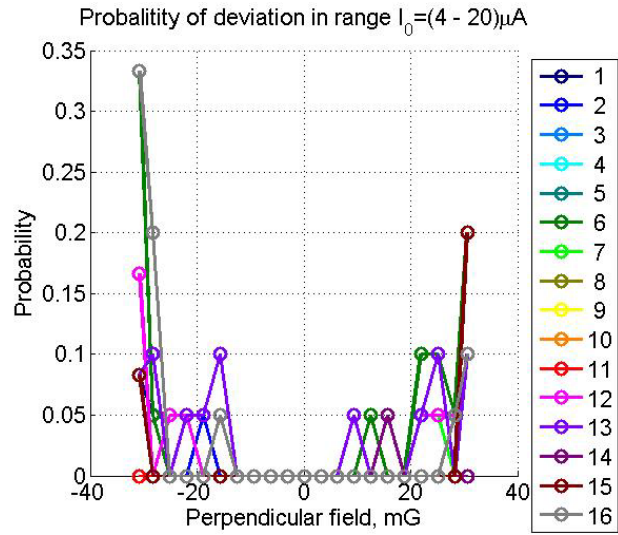
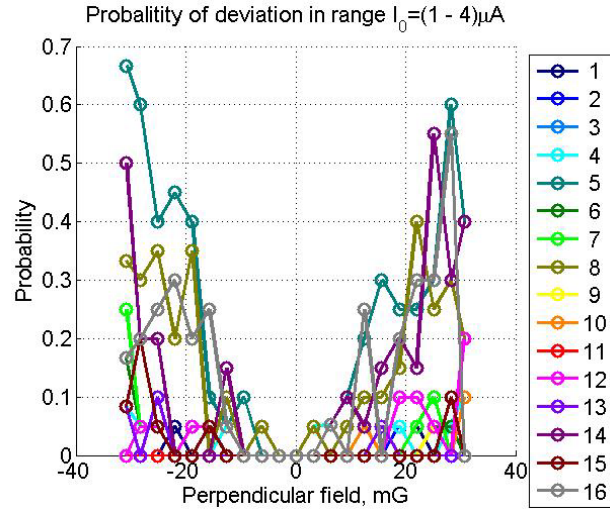


Figure 2.9: Probabilities of deviations of margins as functions of normal magnetic field.

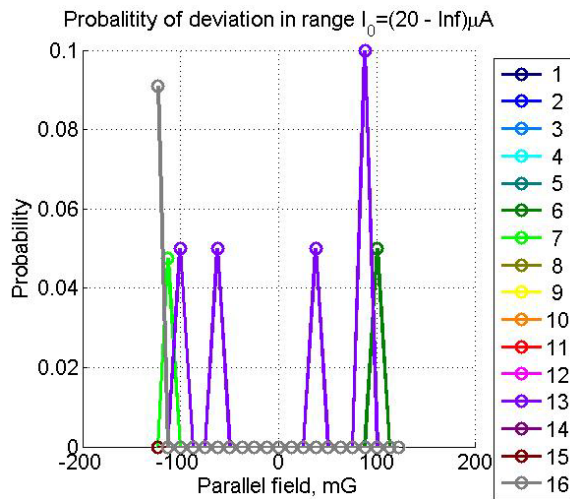
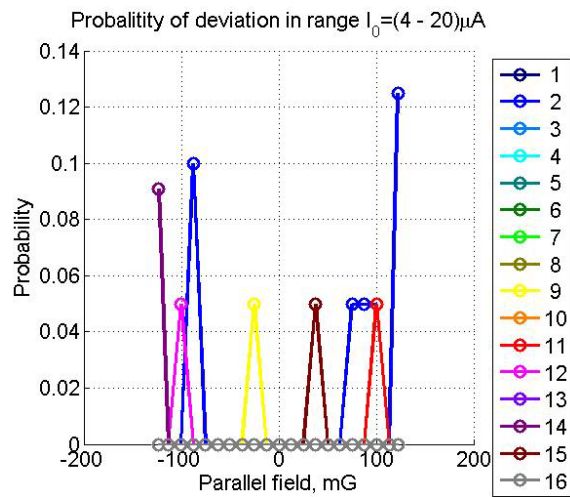
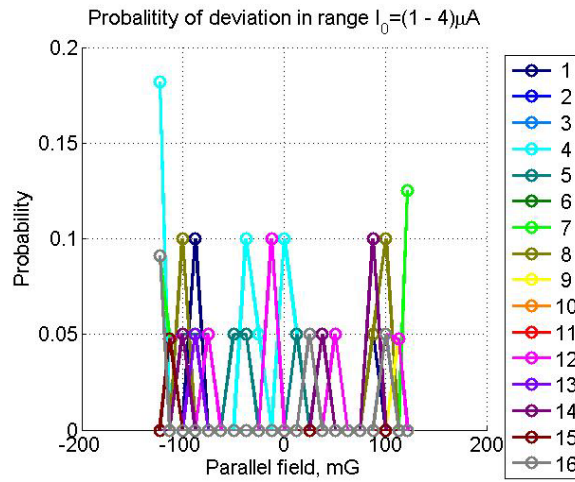
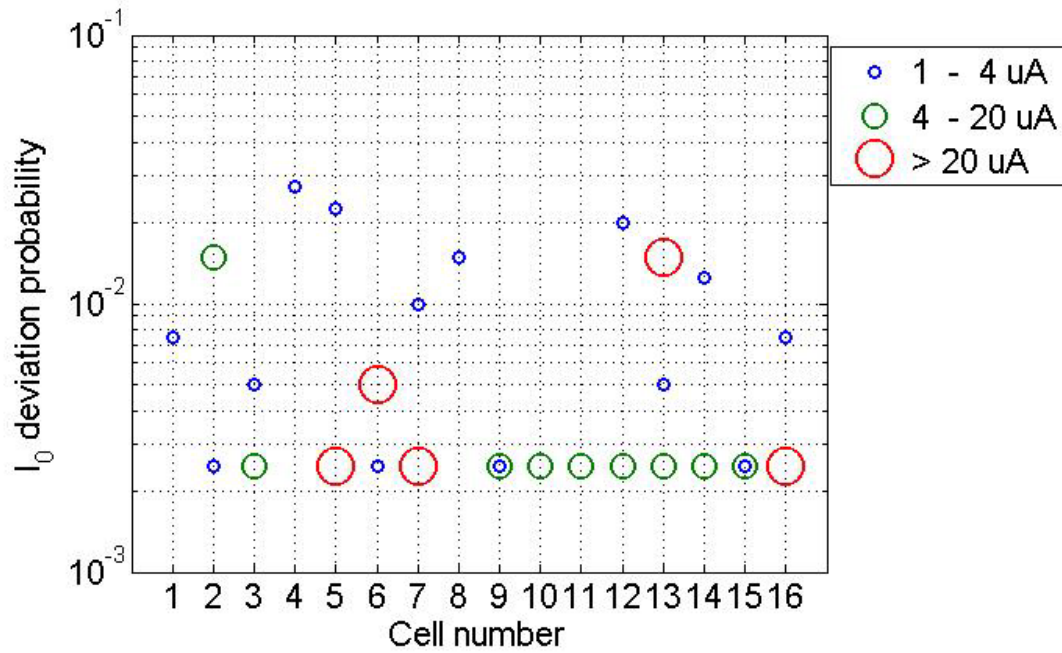
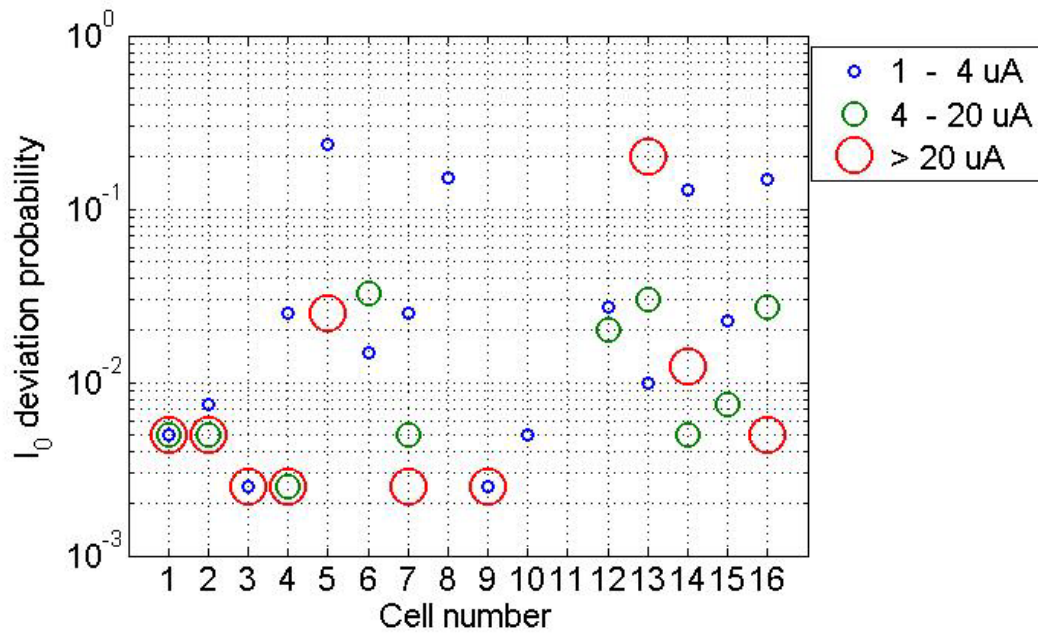


Figure 2.10: Probabilities of deviations of margins as functions of tangential field



(a)



(b)

**Figure 2.11: Probabilities of deviations of D flip-flop threshold currents caused by flux trapping in tangential (a) and normal (b) magnetic fields. Please note that the tangential fields are larger than normal ones. As a result, it would be incorrect to use this plot to compare sensitivities to tangential and normal fields.**

## Chapter 3

### Moats in Superconducting Circuits

#### 3.1 Introduction

As discussed, in the previous chapter, the frozen flux can affect the superconducting circuits by two different mechanisms: it can either directly “punch” Josephson junctions [32] or the frozen flux could be directly coupled to magneto-sensitive SFQ gates [44].

The first necessary step in preventing flux trapping is shielding of the ambient (Earth) magnetic field. However, this measure has proven to be inadequate response. Indeed, the flux is typically trapped by single flux quanta. Their numerical value:  $\Phi_0 \sim 2.07 \cdot 10^{-7} \text{ G cm}^2$  is rather small and, as a result, the residual magnetic field  $B$  should be very low to keep the density of frozen flux quanta:

$$n = B / \Phi_0 \tag{3.1}$$

Below one frozen flux quantum per chip. (As an example, eq. 3.1 gives  $n$  one flux quantum per  $\text{cm}^2$  at  $B$  about  $0.2 \text{ } \mu\text{G}$  or about  $2 \times 10^6$  times below the Earth’s magnetic field.) It is difficult to achieve this level of attenuation, but even such attenuation does not solve the problem because there is a probability of flux trapping even in a magnetic field that is well below the threshold of one vortex per chip.

As a result, it is almost mandatory to allocate some space on superconductor chips for special traps in order to keep frozen vortices far enough from magneto-sensitive circuits. These traps or moats in the ground planes and other large superconducting films are an early [21,22,72,73] and still the most effective way to reduce the sensitivity of

superconductor circuits to flux trapping.

### 3.2 Basic Designs Consideration of Moats

Moats of different sizes and shapes demonstrate different efficiencies for flux trapping [21,22,72]. However, the reported results have no clear conclusion on the shapes, sizes and density of moats. So to get an idea on the type of solution, the particle observations are summarized.

In most cases the critical magnetic field at which moats are still able to trap all frozen flux, ranges from 2 mG to 20 mG [45,]. These fields correspond to  $10^4$  to  $10^5$  vortices per  $\text{cm}^2$  or about 100  $\mu\text{m}$  to 30  $\mu\text{m}$  average distance between the vortices. This distance is comparable to or less than a typical cell size (135  $\mu\text{m}$  in our experiments).

It is difficult to estimate the efficiency of any particular combination of moats theoretically. However, such estimations for simple geometries are trivial: Firstly, it is natural to suggest that the moat density should be sufficiently high and exceed the expected density of frozen vortices. This is important, because a vortex frozen in the moat repulses other vortices of the same polarity and therefore reduces the moat efficiency.

The requirement for high moat density contradicts another requirement that the moats be long. (To be efficient a moat should be longer than the distance between the moat and the protected area.) It is possible to derive formulas for different moat geometries, (see, for example, discussion in [23]):

$$B_c = \pi\Phi_0 / 4W^2 \quad (3.2)$$

The eq. 3.2, has proven to be reliable in estimating the critical fields for vortex expulsion

in superconducting strips. Originally, it was derived for the critical magnetic field of a superconducting strip with width  $W$  [23, 29] but we noticed that it works even better if  $W$  is the distance between long and narrow moats.

It is important that the critical field is inversely proportional to the second power of the distance between moats. (As two examples we can note that 20 mG field is critical for about 25  $\mu\text{m}$  distance between the moats and a typical 400 mG Earth magnetic field would be critical at about 5.6  $\mu\text{m}$  moat spacing.)

### **3.3 Moat Patterns**

The cells with one old design- previously used moat designs, all results in chapter 2 were obtained for this design- and 7 new moat patterns are shown in figure 3.3a. The dimensions of all investigated cells are 135  $\mu\text{m}$  x 135  $\mu\text{m}$ . Moats in the pictures can easily be seen due to their darker intensity.

Our design was done in accordance to the layout that already existed (chapter 2 results). The moats were designed around the inductance and Josephson junctions in the layout and all unused space was filled with moats. Besides, it was useful to increase the inductances of bias resistors. To achieve this goal we opened moats under these resistors. The higher inductances on the biasing leads also reduce power consumption during operation of the circuit. The technique is called L-R loading and is discussed in greater detail in [61]. Finally, where possible the cells were surrounded by moats that were not part of those cells. As we reported earlier in chapter 2, large circuits with such cells have been operational at residual fields below 2 mG to 5 mG. The moat pattern (figure 3.3e) could be described as medium length and medium density.

Figure 3.3a shows the small moat pattern where the moats are just placed around

the Josephson junction. The objective of this design is that to check if just protecting active structures such as Josephson junction are enough for reducing the probability of flux trapping.

Figure 3.3a shows the best of the investigated patterns that could be described as a combination of very long, but rather remote moats and shorter moats bent around the edges and corners to be placed as close to the investigated circuitry as possible. The widths of the moats are 3  $\mu\text{m}$ .

Figure 3.3b an attempt is made to towards a regular moat pattern, which is “interrupted” by the circuitry. More exactly the moat pattern here presents a set of equally spaced (with 15  $\mu\text{m}$  distances) horizontal moats with bridges that are added only to keep the circuitry over the continuous ground plane. The widths of the moats are 3 $\mu\text{m}$ .

Figure 3.3c corresponds to the oldest known recommendation [19,22] - all space not occupied by the circuitry should be occupied by large moats.

Figure 3.3d shows moats similar to the “old” designs, as used in chapter 2, but with a larger density. In other words, the pattern is similar to those shown in figure. 3.3e but some additional superconducting “walls” are added to split larger moats into a greater number of smaller moats.

Figure 3.3f shows moats in which most of the space is not occupied by the circuitry, similar to the figure 3.3c. But in this layout the top ground plane is not used here, which is supposed as superconducting protecting plane to shield external magnetic field during cooling.

In figures 3.3g and 3.3h, are based on continuous moat designs in which one and two continuous moat covering all the six cells are designed respectively. The moat widths

are 3 $\mu$ m and are bent around corners to fit the design of the already existing Josephson junction layout.

All the patterns discussed above have a common drawback: their shapes are defined by the space occupied by the circuitry. In other words, first we design the circuitry and only later we add some moats.

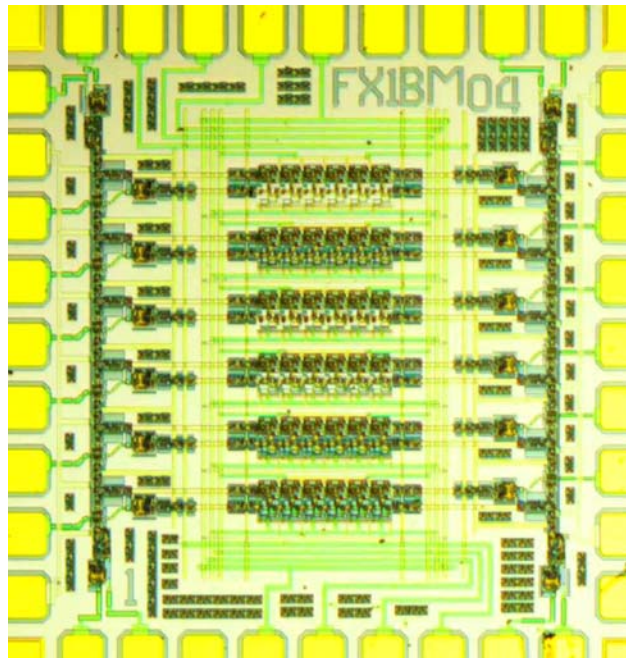


Figure 3.1: It is a 6bit counter clock shift register. The chip was fabricated at Hypres with 1kA/cm<sup>2</sup> process. JJ count 996

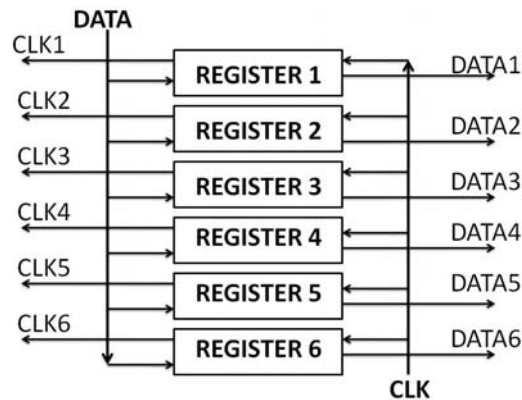
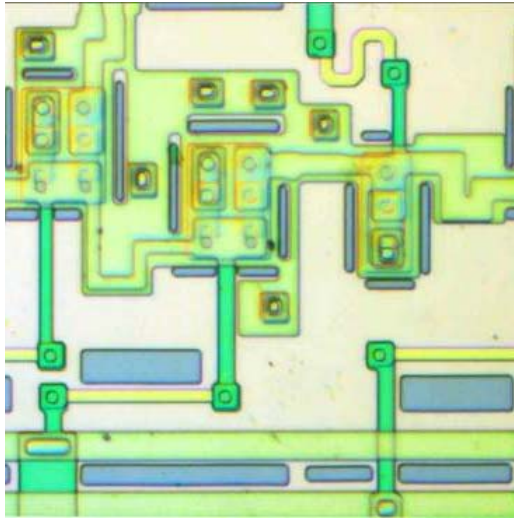
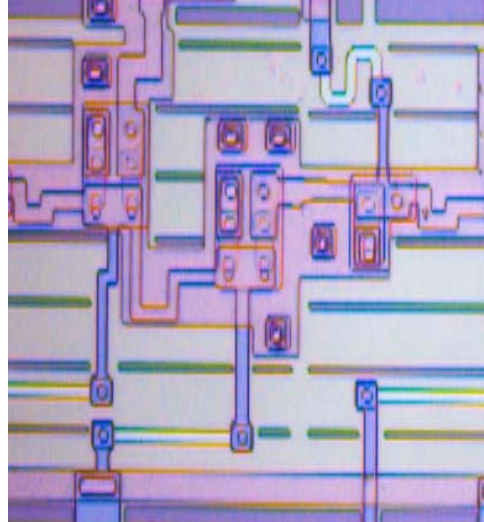


Figure 3.2: Block diagram of the shift register.

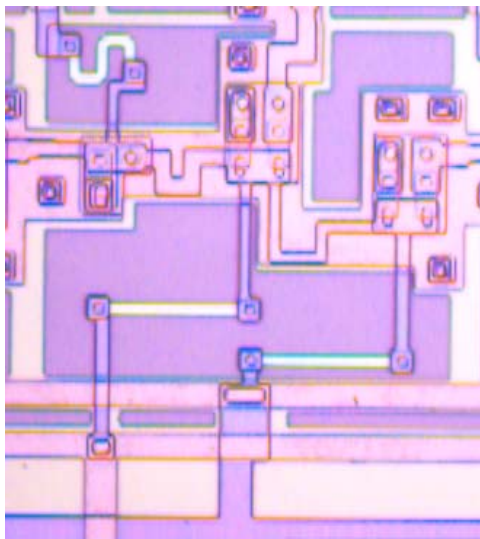




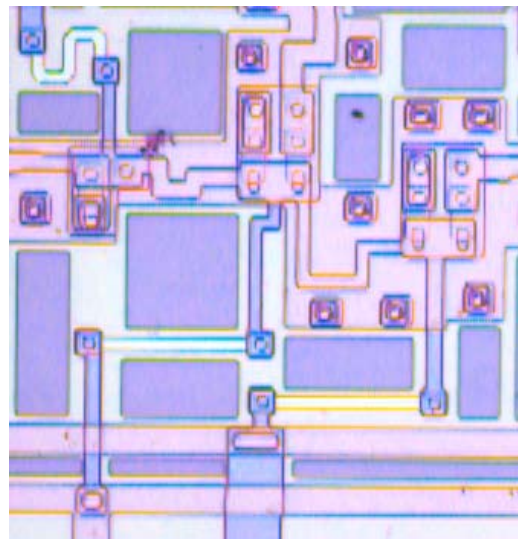
(a)



(b)

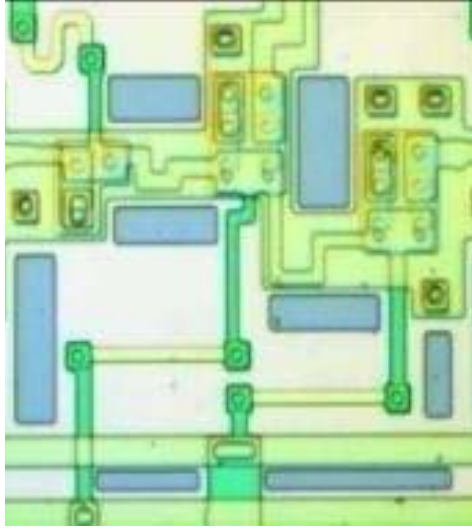


(c)

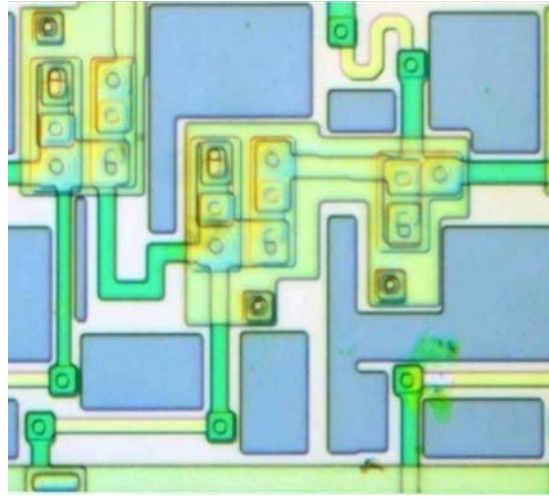


(d)

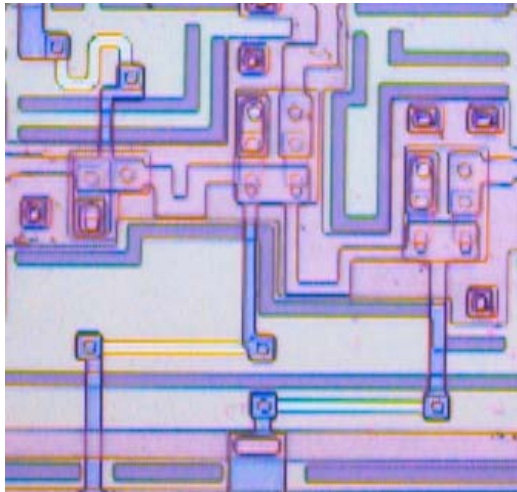
**Figure 3.3: Layouts configurations for different moat patterns.**



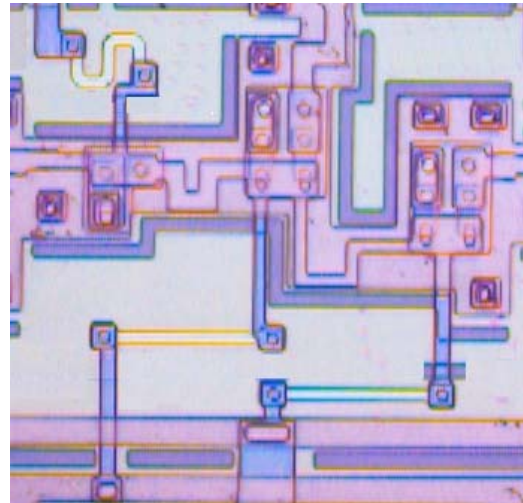
(e)



(f)



(g)



(h)

**Figure 3.3: Layouts configurations for different moat patterns.**

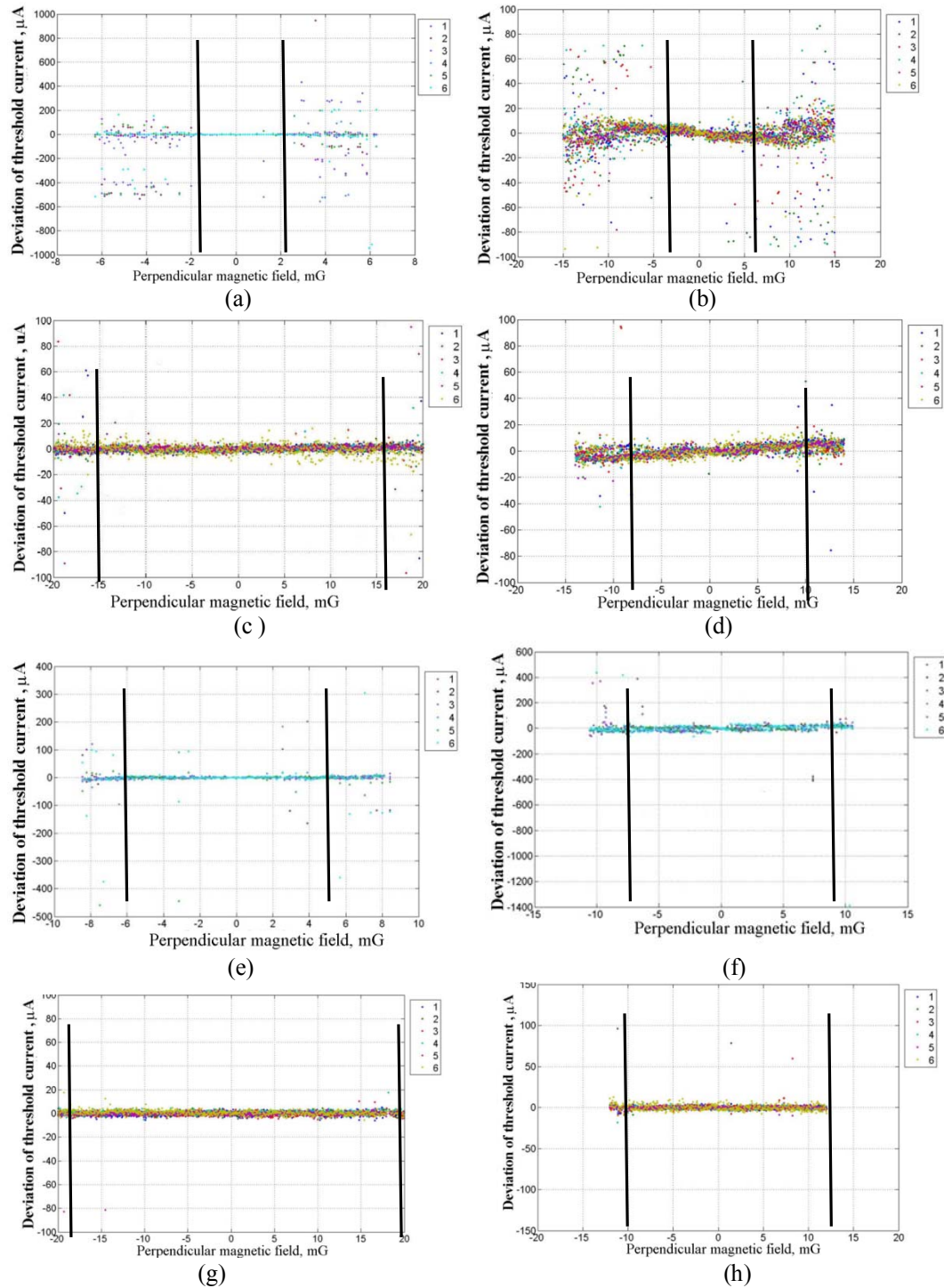


**Figure 3.4: Deviation of the threshold current induced by frozen flux as a function of applied magnetic field perpendicular to the chip. Solid vertical lines show the threshold magnetic field that separates acceptable and unacceptable values of the ambient magnetic field. Different plots (see text) correspond to different moat configurations.**

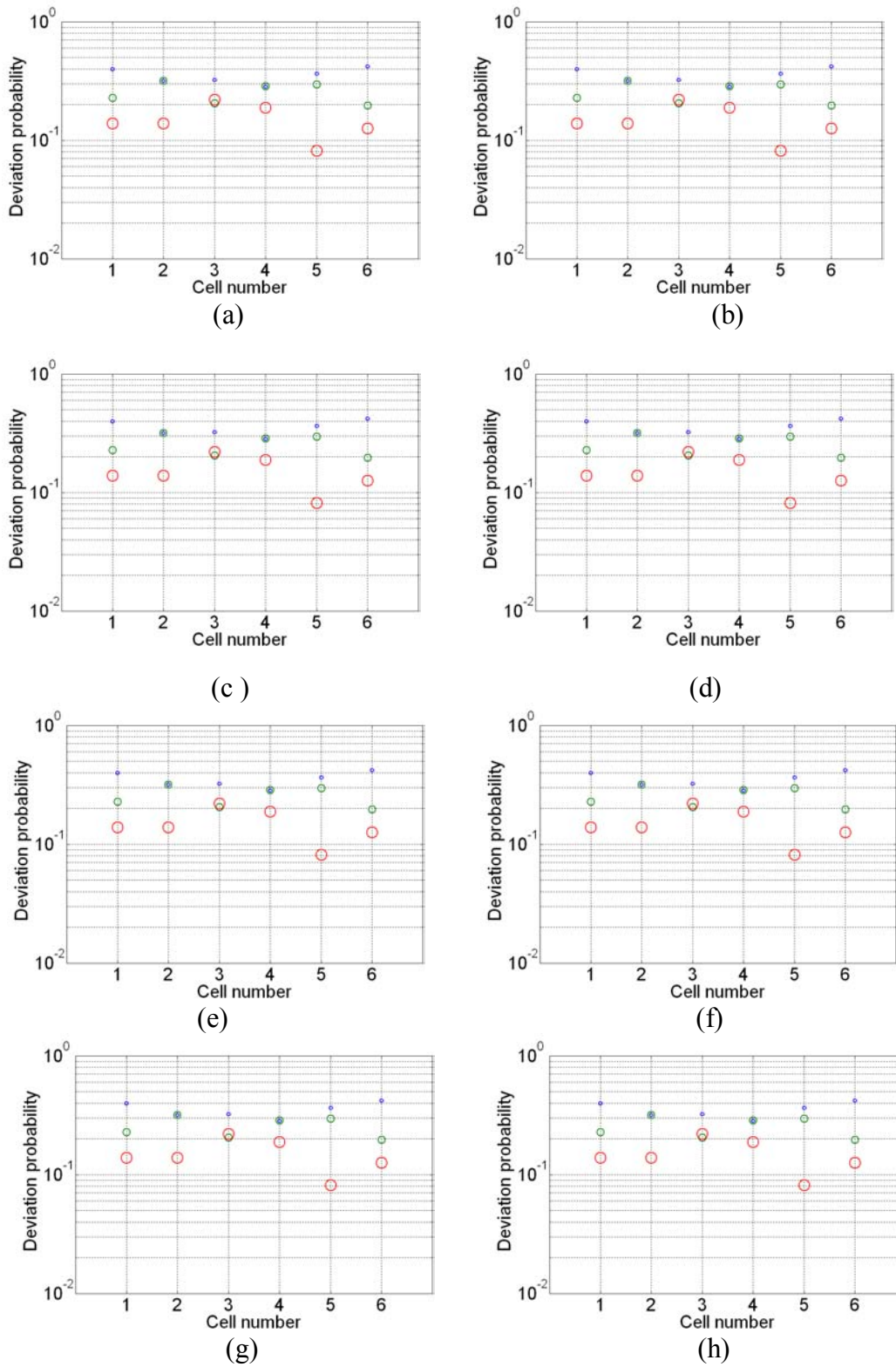


**Figure 3.5: Bubbles represent the probability of a deviation of threshold current caused by trapped vortices. Small bubbles correspond to the deviations in 1-4 $\mu\text{A}$  range, medium bubbles correspond to 4-20 $\mu\text{A}$  deviations, large bubbles indicate deviations that are greater than 20 $\mu\text{A}$ .**

### 3.4 Threshold Limit of Moat Pattern

The process of measurements for these experiments has been described in detailed in section 2.5 of the previous chapter. However, the test chip was designed with the intention of multiple I/O for obtaining provisions to measure number of different shift registers on a single chip.

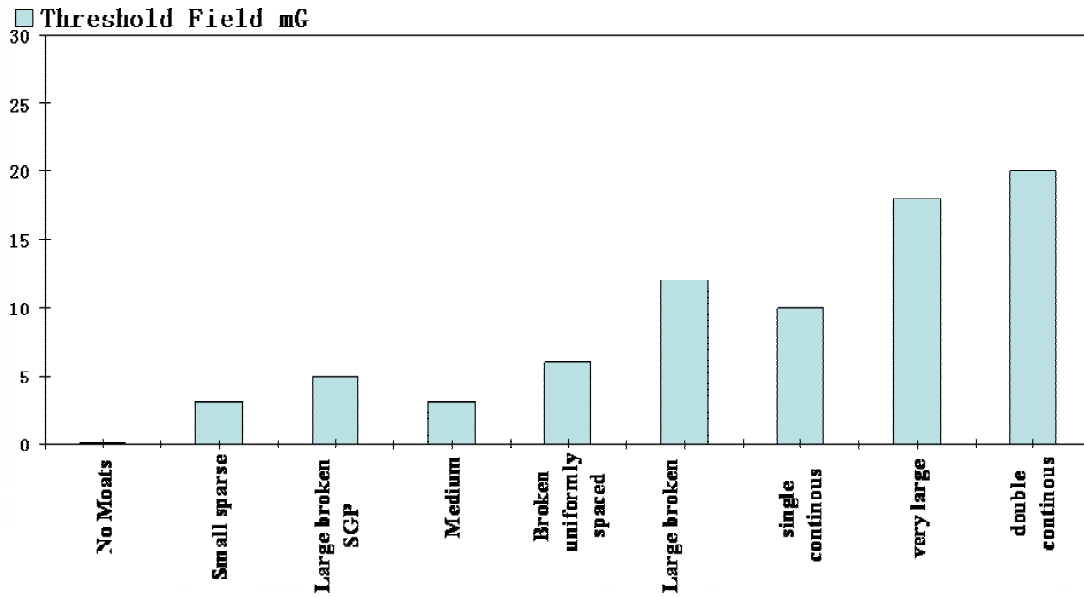


Figure 3.6: Threshold fields (in mG) for investigated moat patterns. Names of corresponding microphotographs in Figure 3.3 are shown below the columns

The most recent revision of our test circuits (Figure 3.1) contains 6 independent shift registers that share only some clock and data auxiliary circuits. As a result, we are able to carry out a comparative study, for example, of six different moat patterns. This time we carried out our experiments at 4.2 K in a transport helium Dewar. The thermo-cycling was provided under OCTOPUX [33] control using off-chip heaters and thermometers. The magnetic field was applied only during the chip cool down. Typically, we made 50 thermo-cycles at each magnetic field and totally about 10,000 thermo-cycles

for one experiment that usually lasts from 24 to 48 hours.

### 3.5 Experimental Results

As we mentioned in the previous chapter data can be represented in numerous ways. The plot is a dependence of deviation of margins for “Probe” currents from their nominal values (not affected by the flux trapping) as a function of magnetic field (Figure. 2.4, chapter 2). (Note that D cells have the extra current terminals “Probe” connected to a separate power line with zero nominal bias voltage.) It is easy to see that the deviations are rare and small at low fields and much more frequent and greater at larger fields. Two solid vertical lines in figure 3.4 visually separate these areas and show critical fields. Note that D cells have extra current terminals (Probe) connected with a separate power line with zero nominal bias voltage.

These critical fields are our most important results and they accumulated for investigated moat patterns in figure. 3.5. This figure definitely reflects our progress in understanding the efficiencies of different moat patterns. The best result achieved is about 20 mG. We would like to note that it is rather close to the simple forecast provided by eq. 3.2.

To see variations of flux trapping from cell to cell we use “bubble” plots (Figure 3.6), in which the horizontal position of the bubble on the plot codes the cell number. The vertical axes position of the bubble shows (in a log scale) the probability of flux being trapped. The plots show bubbles of three different sizes. The small bubbles show the probability of very small values of circulating currents ( $1 \mu\text{A}$  to  $4\mu\text{A}$ ) induced by the trapped flux.

So small currents are not dangerous for the cell, but we present these data as proof

of the high accuracy of our technique. Besides, we believe that these deviations to be expected because they are caused by vortices trapped in the moats. Medium bubbles (4  $\mu\text{A}$  to 20  $\mu\text{A}$ ) correspond to damage that, we think, would not be acceptable for circuits that should operate near their speed limits or in the case of very large integration level. Finally the large bubbles (above 20  $\mu\text{A}$ ) correspond to damage unacceptable for any practical circuits. Unfortunately the bubble plots contain data averaged over all values of applied magnetic field. As a result, they depend on the range of the applied fields. However, as we mentioned earlier here, we have the possibility of comparing properties of similar cells in one register. It looks as though all the cells of one register have statistically equivalent flux trapping properties. However, earlier in chapter 2, we observed that some cells could be much more sensitive to flux trapping because of undetected fabrication defects.

### **3.6 Empirical Rules for Developing Moat Patterns**

Based on the above obtained we can formulate a set of guidelines for developing a RSFQ layout in which the circuits will be most resistive to parasitic flux trapping.

The procedure can be summarized as empirical rules

1. It is recommended that multiple long moats are used in the cell design.
2. The circuit elements must be designed in rectangular span of width around 50 $\mu\text{m}$ .

If circuit design span is larger than widths 50 $\mu\text{m}$ , long rectangular moats must be incorporated within the design elements.

3. It is advisable to have at least only moat close to every Josephson junction. JJs are the most effected in the event of flux trapping and every precaution must be taken to safeguard them.

4. The gap between the moat holes must be much smaller than moat size only then the moat will have an effect.
5. The gap between two moat holes must not be too close that shielding current will exceed the critical current.
6. The bias lines will attract vortices when carrying high value of currents. So the bias lines must have moats close to it to trap the flux.
7. Care should be taken as the holes not cross bias lines to prevent shorts in the circuits.
8. Use of multiple numbers of small moats should be avoided.

### **3.7 Fabrication Dependency**

The effect of fabrication and flux trapping was also determined. When we tested two circuits which are schematically equivalent and also have the same layout configurations, the effect of fabrication run can be found out. It turns out that the flux trapping process is very less influenced by fabrication. This is evident in the figure 3.7 where the deviation of the threshold current is zero till the perpendicular magnetic field is of the order 7 mG.

### **3.8 Discussion**

We investigated eight moat patterns and its influence on flux trapping in superconducting circuits. The most important thing is to avoid serious mistakes such as leaving large chip areas without moats or making a moat only in one ground plane without a corresponding moat in the other ground plane.



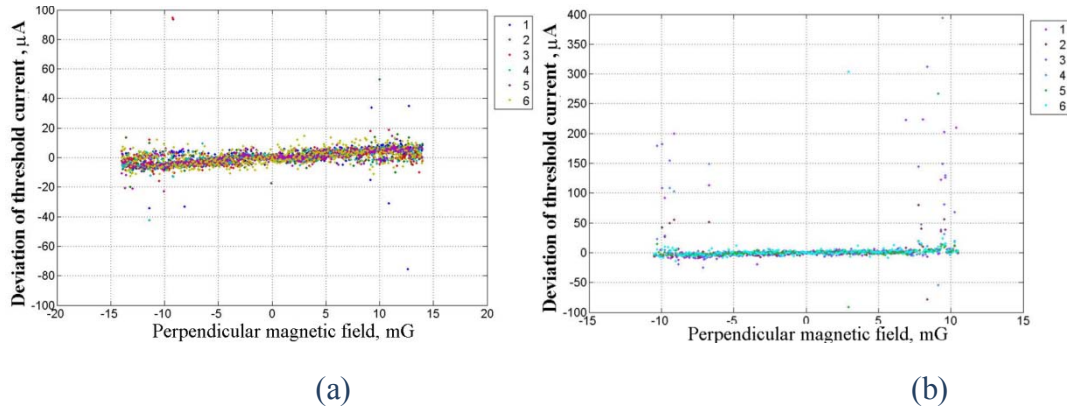


**Figure 3.7: The threshold current deviation for layout 1e, for mask releases (a) KL1094 (b) KL1025**

Next, it is important to keep the distance between the moats as small as possible. At 20  $\mu\text{m}$  to 30 $\mu\text{m}$  distance (that is easily achievable with the available HYPRES technology) [82] the critical field could be as high as 20 mG. If Eq. 2 is correct then at 5  $\mu\text{m}$  moat spacing the critical field would be comparable with the Earth’s (400 mG) magnetic field. This scale of dimensions is challenging for currently available superconductor technologies. This is because all active circuitry should be placed over narrow (5  $\mu\text{m}$ ) ground plane “strips”. But this goal could be within the reach of any well developed sub-micron lithography techniques if it is available for superconducting technology.

Finally, the moats should be sufficiently long. More exactly it is highly desirable that they are longer than the distance between them. Fortunately we did not notice any indications that some moat shapes are worse than others. In other words, there is great freedom in selecting moat shapes and patterns that would fit practically any design style.

## **Chapter 4**

### **Power Independent RSFQ logic cells**

#### **4.1 Introduction**

Low power RSFQ cells are essential in the large scale integration of RSFQ circuits. The dissipation of power in RSFQ circuits is small in comparison to semiconductor devices, but high for the temperature range of 4K. The main source of power loss is mainly due to the static dissipation in the bias resistors. The dynamic power dissipation, due to the switching operations of the junctions, is quite low. The static power dissipation is a result of continued applied bias to the circuit, to maintain the logic state of the operating circuit. Low power RSFQ circuits have been recently reported to be used as support circuits for developing superconducting quantum computational structures [18,19,70,81]. Mentioned prospective SFQ circuits are diversified and different kind of circuits would require different power minimization techniques [41,43,61,67,68,69,75,76,77].

#### **4.2 Basics of Power Independent Operation**

In this chapter, we discuss a new technique, where circuits are able to perform some functions without any significant energy static dissipation. More exactly, we try to show that the suggested technique could be applied to any RSFQ cell to obtain Power Independent (PI) operation. Power independence, means an ability to switch off circuits without any loss of stored information. As a result, power independent circuits could be powered only when logic operations should be performed [49,50].

The simplest power independent circuit with memory is a well-known single-junction SQUID [5] as shown in figure 4.1a. The single junction SQUID is a superconducting

loop with sufficiently large loop inductance  $L$  interrupted by a single Josephson junction. The dynamics of single Josephson junction SQUID has been well known for many years now and will not be discussed in detail here. But, it may be sufficient to recap the flux modulation as a function of the bias current to the SQUID as shown in figure 4.1b. From the figure 4.1b we can see that, we can write "1" or "0" by applying large enough positive ( $I_b > I_{th1}$ ) or negative ( $I_b < -I_{th1}$ ) bias current  $I_b$ . The device continues to remember any of these states if bias current is switched off ( $I_b = 0$ ) as there is no dissipation in the superconducting loop.

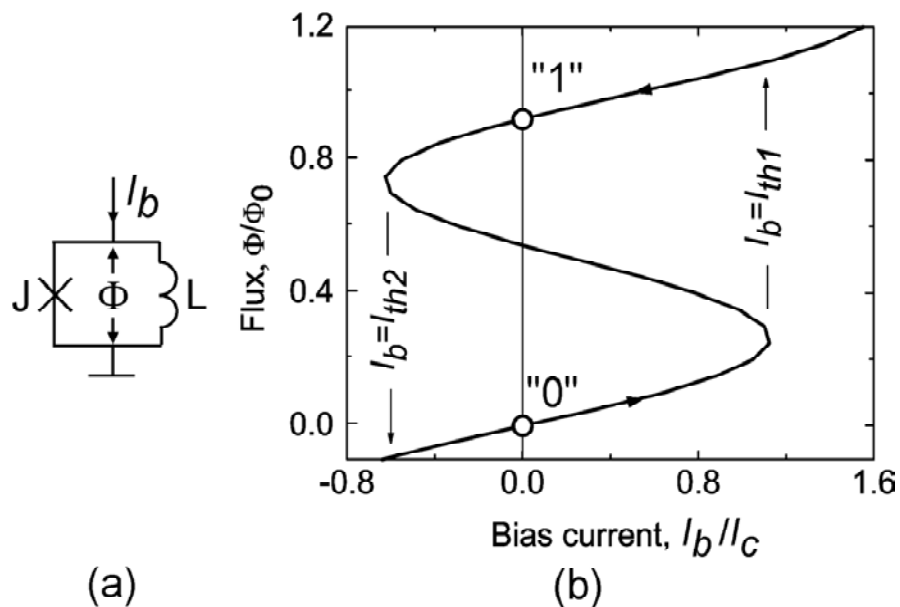


Figure 4.1: A single junction SQUID as the simplest power independent cell

The introduced memory cell of single junction SQUID could be incorporated into RSFQ flip-flops and logic gates. Before we discuss the operation of the power independent RS flip flop let us understand the operation of RSFQ RS flip flop.

### 4.3 Developing Power Independent RS flip-flop

First, let us recap how a RS Flip-flop functions, shown in figure 4.2a. The J3, L, J4 loop is a two junction interferometer with  $I_c L = 1.25\Phi_0$ , so it can store a flux quantum. The current in the loop can be expressed as the sum of the bias current equally divided between the two junctions and circulating current  $I_p = \pm\Phi / 2L$ .

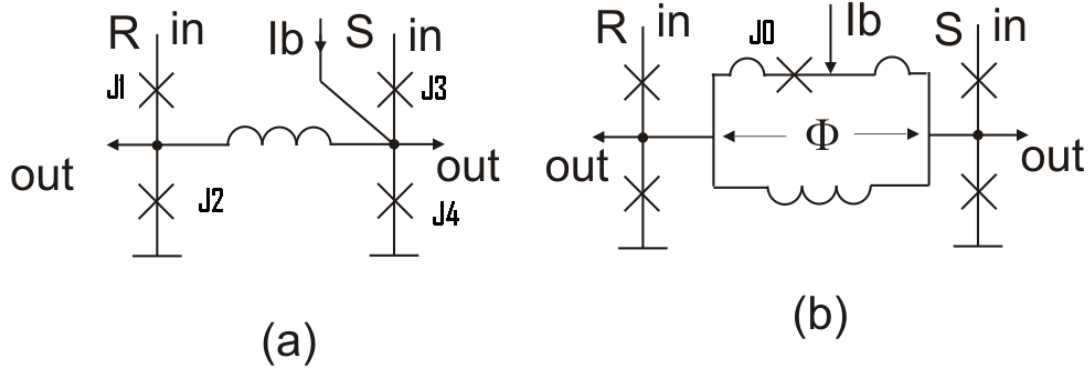


Figure 4.2: Transformation of a conventional RSFQ RS flip-flop (a) into a power independent cell (b)

Initially, the circulating current is counterclockwise, representing a stored “0”. The currents when the bias is applied are  $I_{J3} = (Ib / 2) + I_p$  and  $I_{J4} = (Ib / 2) - I_p$ .

When input pluses are applied to the input (S) and reset (R) terminals, this causes circulating current to reverse polarity. When pulse arrives on the input, its current passes through the J2 (nearly biased at  $\Phi = 0$ ) and causes J3 to switch and the circulating current is transferred to J4. The clockwise circulating current is representative of a stored “1”. Then, when a reset pulse is applied, it passes through J1 and into J4, thus causing it to switch. The voltage pulse developed during the switching reverses the circulating current, so again a “0” is stored in the loop; it simultaneously applies this SFQ voltage pulse to the output through J4.

The junctions J1 and J2 have lower critical currents than J3 and J4 and to protect

the inputs from back reaction of the interferometer if pulses come under the wrong circumstances.

In the conventional circuit figure 4.2a, as discussed above, the magnetic bias is created by asymmetrically applying bias current  $I_b$ . This magnetic bias disappears if the bias current is switched off. As a result the circuit keeps its internal state only as long as the bias current remains applied.

Figure 4.2b shows this transformation for the simplest RS flip-flop. The operation of the Power independent RS flip flop operates in the similar manner as the conventional RSFQ RS flip flop. In contrast PI cell (figure 4.2b) holds its magnetic bias inside its SQUID, instead of a single quantizing inductance. To activate the SQUID and the circuit one should apply large enough bias current  $I_b$ . (Note that this "activating" current is slightly greater than its nominal value for regular logic operation.) Being activated the circuit remains magnetically biased (presumably by flux about  $\Phi_0/2$ ) even if bias current is off. Note that even power independent circuits should be powered to perform logic operations, in order to provide the needed the additional magnetic flux bias.

#### **4.4 Investigations of Power Independent Circuits**

In order to investigate the power independent RSFQ flip flop we simulated the RSFQ flip flop. The clocked RS flip flop, where the reset terminal used as the clock terminal can be used as the RSFQ D flip-flop.

##### **4.4.1 Design of 6-bit Shift Register with PI cells**

Figure 4.3 shows schematics of a D flip-flop re-optimized for operation in power independent mode at 4 K. The power independent D flip-flop has the single junction interferometer that can be identified by schematic components L1, L2, LD4 and J0. The

interferer meter is biased by current IPI. The components in the figure 4.3 are represented by dimensionless PSCAN units, which are easier for computation.

Figure 4.4 illustrate current and input data patterns used for a numerical circuit optimization with PSCAN software package. The new feature of the simulation is a more complex shape of applied bias current IPI. During the simulation it was required that junction J0 is switched only one time and when IPI current it applied for the first time. No other junctions switched when bias current goes down.

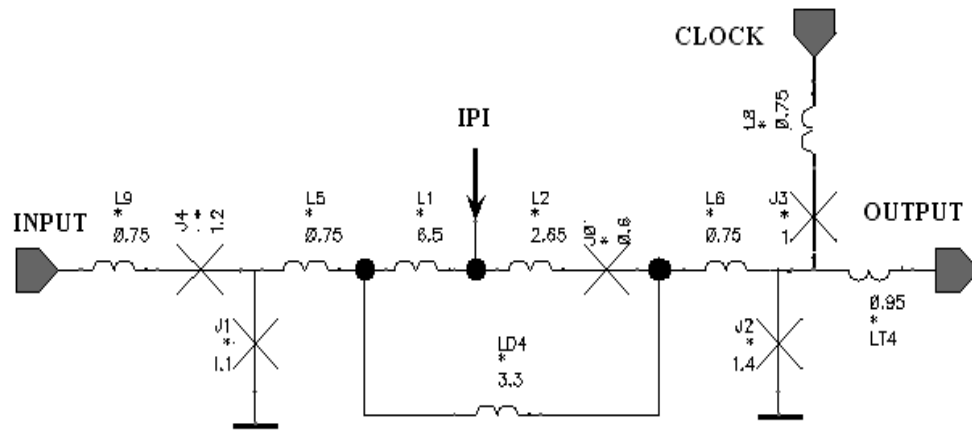


**Figure 4.3 Power Independent D flip-flop. Bias current IPI does 2 things: it “activates” SQUID with junction J0 and power the cell during its normal operation**

#### 4.4.2 Experimental Results

A 6-bit shift register with PI D cells has been designed and laid out for HYPRES fabrication technology. The shift register has been incorporated into a benchmark test chip developed for a comparative study of flux trapping sensitivities of different D cells. (The revision of the test circuit has been presented in chapter 2.)

Figure 4.5 shows a microphotograph of a fully operational circuit (as shown in figure 4.6) fabricated at HYPRES (1 KA/cm<sup>2</sup> technology). Bias current margins ( $\pm 16\%$ ) for the only measured chip are about 2 times below our numerical estimations (35%).

The figure 4.6 the shift register was tested with Octupux setup, where the low speed testing was used to confirm the correct operation of the shift registers. Since the shift register is a counter shift register, the clock and the data pulses travel in the opposite direction and this can be confirmed by the traces in figure 4.6.

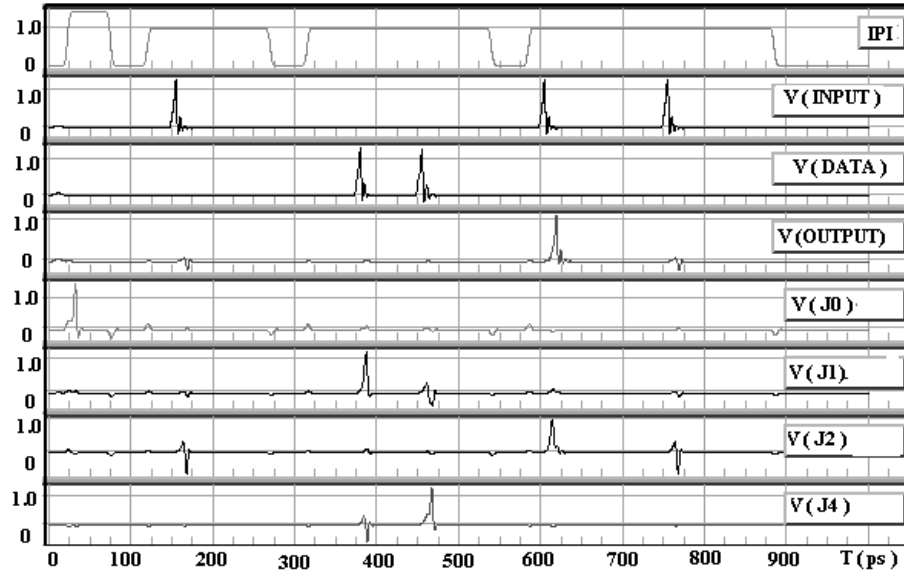


Figure 4.4: Current (upper trace) and voltage waveforms illustrating the power independent operation of D cell. Note that the “activation” procedure could require larger current IPI than those during the regular circuit operation

## 4.5 Flux Trapping in Power Independent RSFQ Cells

The topic of flux trapping was discussed in chapters 2 and 3 in detail. In this chapter to complete the study of power independent cells in RSFQ cells, we investigate flux trapping in power independent RSFQ cells. The methodology to investigate, including the circuits and I/O, are the same, as discussed in chapter 2,3, and the designed chip can be seen in figure 4.5.

Three different layouts configuration for the PI-RSFQ cells were investigated. It presents the results of investigations of a specially developed chip that contains power

independent RSFQ cells with apparently the same schematics but different layouts. The goal of this experiment is to compare prospective design styles and to select those with the highest “resistance” to the parasitic flux trapping and also compare with flux trapping in conventional RSFQ cells.

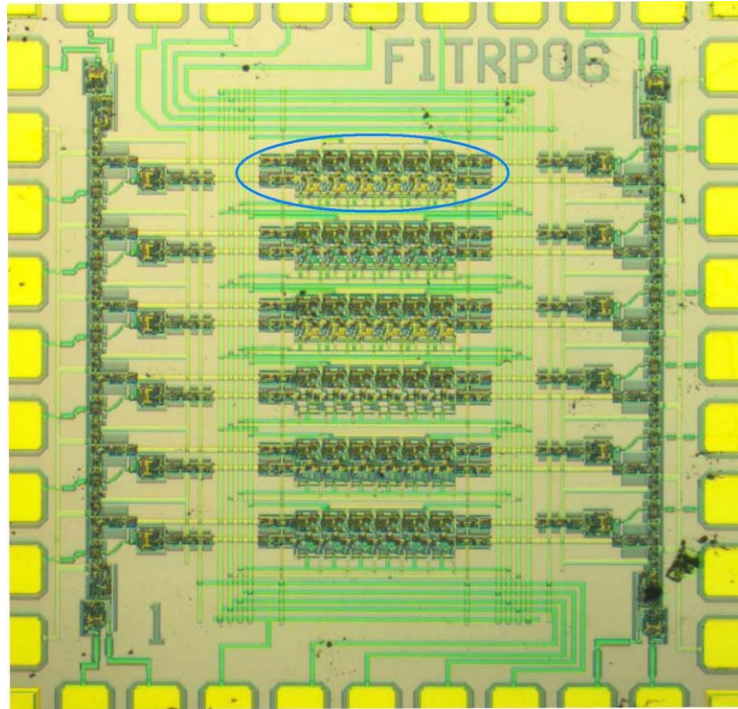


**Figure 4.5: The microphotograph of the shift registers of the power independent cells. The first three registers are designed with power independent cells.**



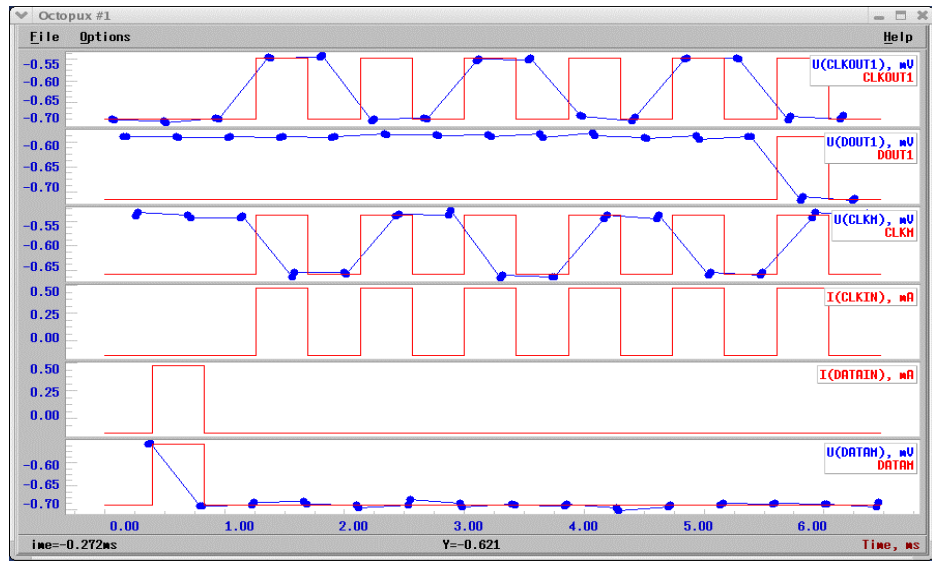
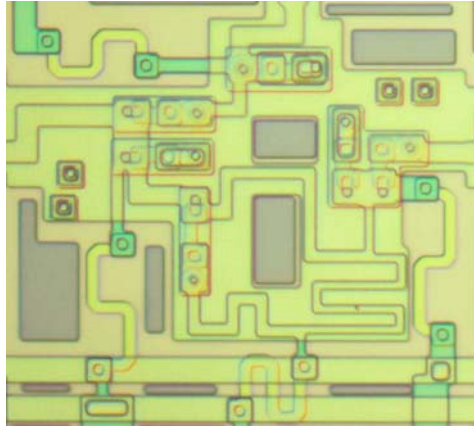
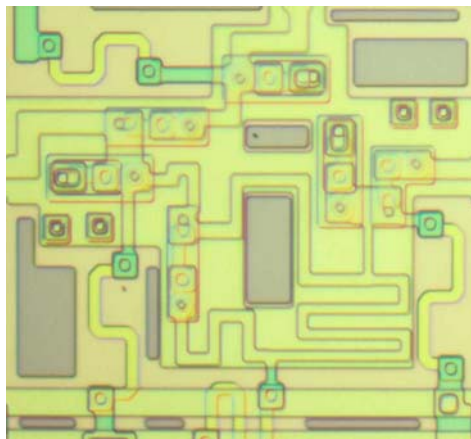


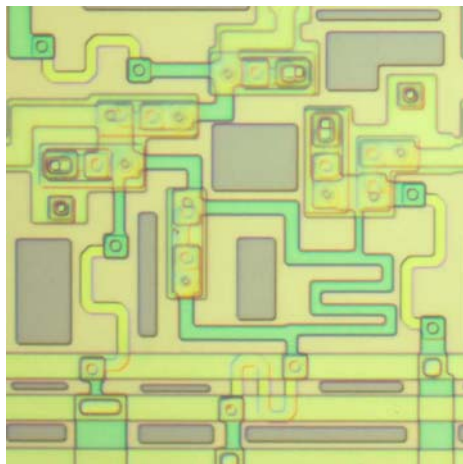
Figure 4.6: Low speed testing of one shift registers. The logic '1' applied to the input (two lower traces) is read out from the output (the second from top trace) after 6 clock cycles (middle traces)



(a)

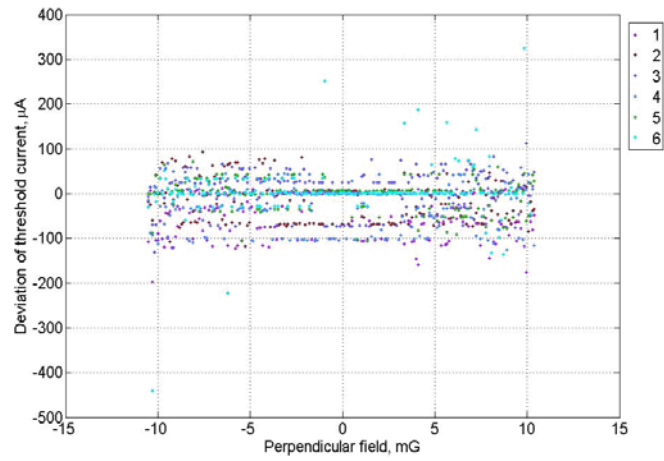


(b)

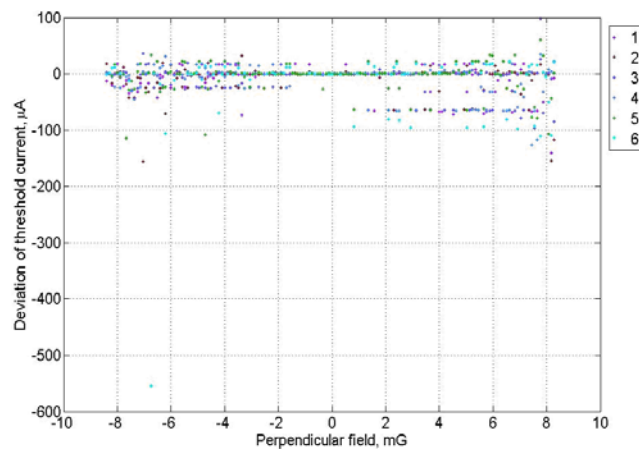


(c)

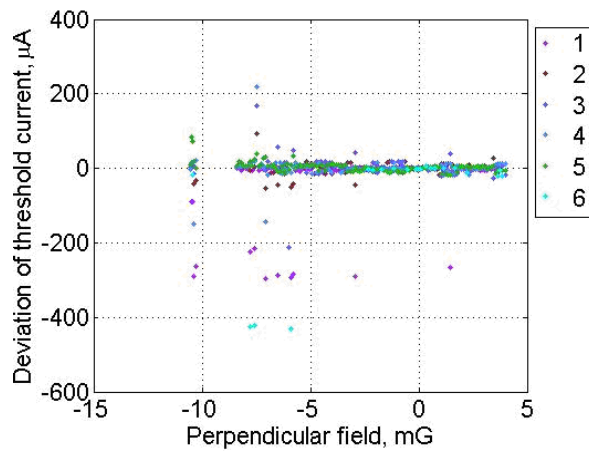
**Figure 4.7: Three layout configurations for PI D flip-flop.(a)Josephson junctions are grounded only to the sky plane,(b) Josephson junctions are grounded by using sky plane and ground plane,(c) sky plane is absent.**



(a)

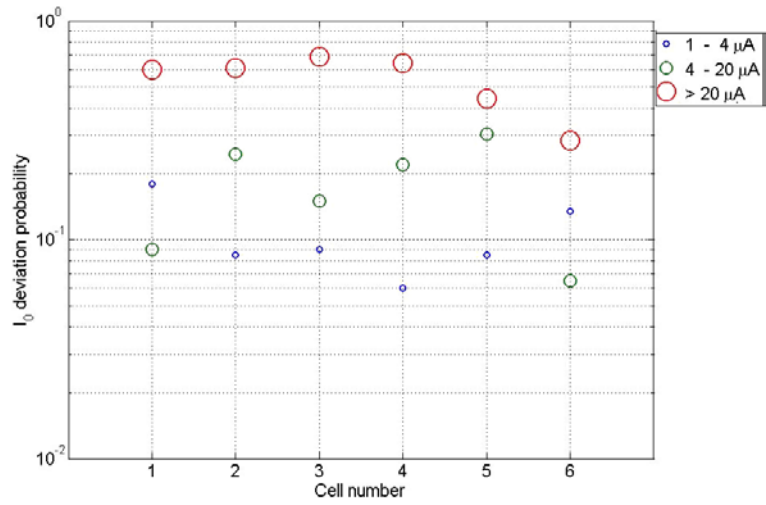


(b)

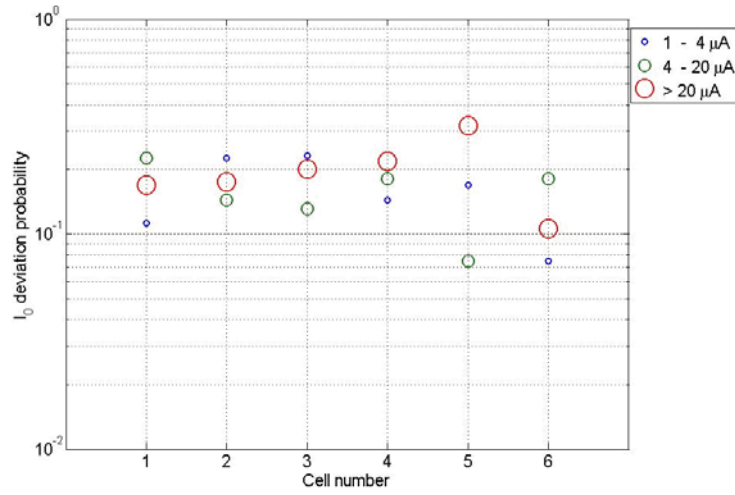


(c)

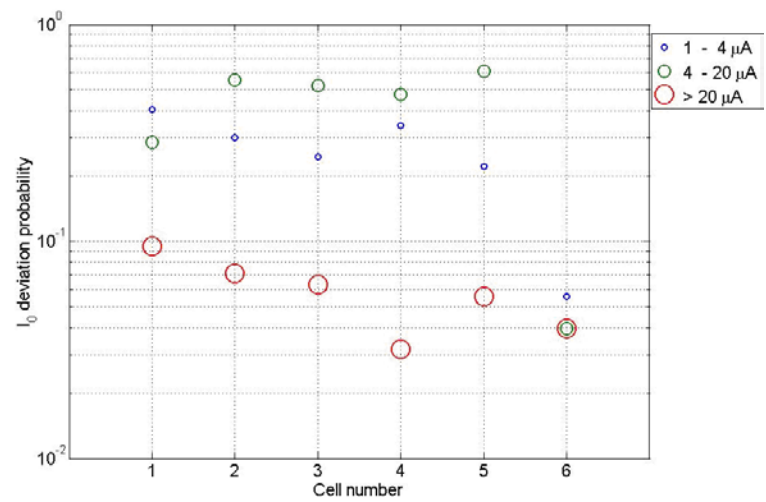
Figure 4.8: Threshold deviations for corresponding layouts configurations in figure 4.7



(a)



(b)



(c)

Figure 4.9: Probability of flux trapping in the each cell for the corresponding layout in figure 4.7

The results of the flux trapping experiments on shift registers designed with power independent cells are shown in figures 4.8 and 4.9. The method to explain the results shown we use the same interpretation used for figures 2.8 and 2.9 presented in chapters 2. Based on the results presented, we can now deduce which is the best layout configuration.

The lower the threshold current deviations for each cell with varying magnetic fields are the better the configuration against parasitic flux trapping. Deviations of threshold currents caused by flux trapping magnetic fields are shown in the corresponding figure 4.8 for each layout in figure 4.7. We can see that the best layout configuration is figure 4.7b. We can observe that at lower fields (below 3 mG) there are no noticeable flux-trapping induced deviations of the margins in figure 4.8b, but in figure 4.8a the deviation is large. In figure 4.8c the threshold fields are much lower than figure 4.8a; figure 4.8b and deviation of the margins occurs at lower magnetic fields. The least deviations observed in the threshold current are in figure 4.8b over large magnetic fields. The graphs cannot be directly compared as the working threshold for each layout as the operating regions are different, but more or less each layout gives an insight as which of the layout is most resistant to parasitic flux trapping.

The probabilities of deviation of threshold currents are shown in figure 4.9. We can see that the probability of large deviations of current (over  $20\mu\text{A}$ , which are likely to cause the circuit to fail), is small for figure 4.7b, but quit high for figure 4.7a. We can also see that the probability of deviation of large current is least for figure 4.7c, but we have to keep in mind that the threshold operation limit for figure 4.7 is the least, so in that operating region it works best (below 3mG magnetic field). In figure 4.9b, we do

however, see that one cell namely '5' of the shift register indicates a probability of larger than the average for large deviations, we are likely to believe it is due to damage caused to the cell (such as a scratch) or presence of impurities in close proximity to it.

#### **4.6 Discussion and Conclusion:**

In this chapter, we have successfully proposed and demonstrated a new low power technique called the power independent RSFQ cells. The operation of the power independent was verified by simulation. The power independent D flip flop was used to construct a 6 bit shift register and its operation was verified experimentally. Flux trapping experiments were also carried out on three different layout configuration of the power independent D flip-flop layouts. The performance of Power independent D flip flop is inferior than conventional D flip flop towards parasitic flux trapping, which can be attributed to the single junction interferometer used as a memory element in the PI-RSFQ flip-flop.

## **Chapter 5**

### **Current Recycling: Technique and Application**

#### **5.1 Introduction**

One of the main advantages of RSFQ circuit is that only dc bias is needed. It eliminates the cross-talk problems caused by ac biasing and makes designing larger blocks easier. However, in larger circuits the total dc bias current could add up to a few amperes and such large bias currents cause large heat dissipation, which is not preferred. One of the techniques that has been proposed [10] is biasing the circuits serially otherwise commonly known as 'current recycling'. Biasing large circuit blocks in series (referred to as current recycling or current re-use) will essentially reduce the total current supply for the superconducting IC to a manageable value. Both capacitive [57] and inductive methods [56] of current recycling have been demonstrated at a small scale. Current recycling becomes easier at higher current density of the superconducting IC. Current recycling however has its limitations; it does not reduce the on-chip static power dissipation by the circuit blocks and also due to additional structures, the area occupied by the circuit's increases.

In this chapter, we will demonstrate the implementation of current recycling technique using inductive coupling, also its application in the design of high frequency drivers. The circuits designed by current recycling technique have been found to be highly sensitive to external magnetic fields.

## 5.2 Serial Biasing Circuit Technique

To demonstrate the method of current recycling, we have designed a Josephson junction transmission line (JTL) as shown in figure 5.1. The complete operating principle of the circuit is explained below.

The figure 5.1 shows structure of one module. The module consists of three parts, the driver, receiver and the payload. The payload is usually the circuit block that is used for operation, in this case to keep matter simple a JTL has been used, as its operating margins are very high. The payload can otherwise be replaced by flip-flops, filters, or logic gates.

Before we explain the operation of the driver-receiver circuit, it is important to remember a few thumb rules for the current recycling design. For current recycling, the ground planes under adjacent circuit blocks must be separated and subsequent blocks biased in series. It will also be necessary to isolate SFQ transients between adjacent blocks. This may be achieved by low pass filters, but will need to avoid power dissipation in the filters. Series inductance could provide high frequency isolation; the inductors could be damped by shunting with suitable resistance, such that there is no DC dissipation. Capacitive coupling between adjacent blocks can be used for current recycling however they are not discussed here and also capacitors used for this method also occupy larger space compared to the inductive filtering method.

To demonstrate the technique, the circuit with 80 payloads (JTL) serially biased was considered. The payload block consists of a receiver and driver. The requirement for serial biasing of circuits is that



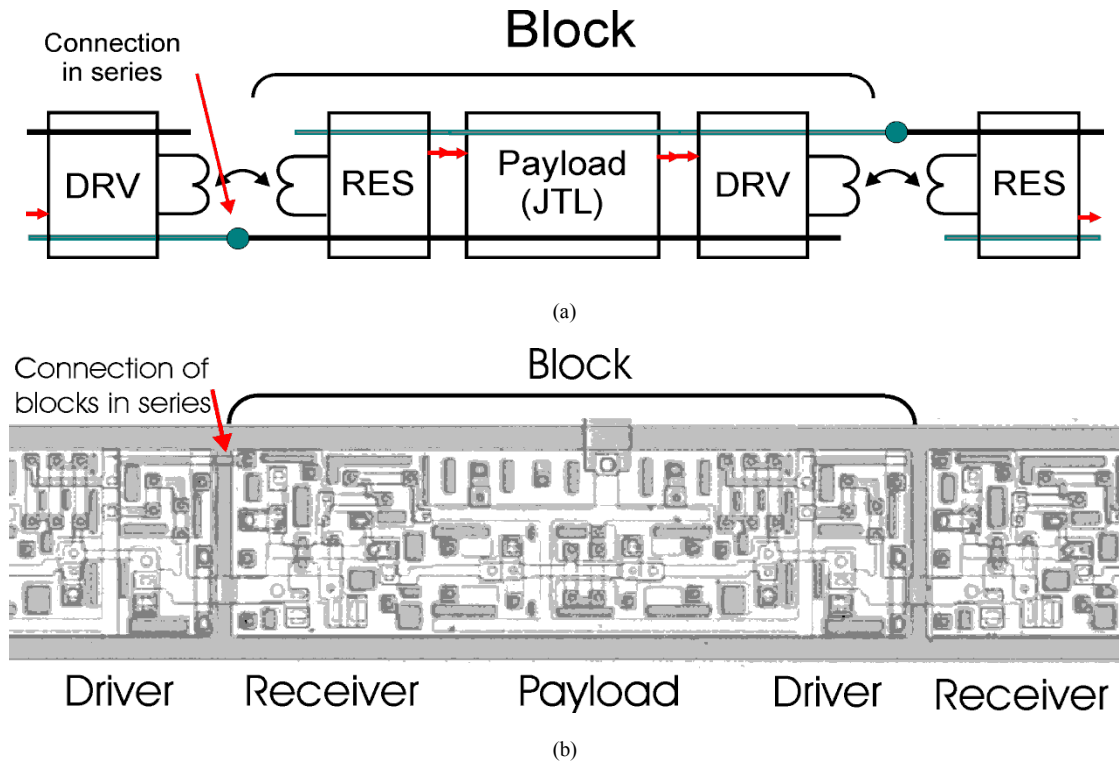


**Figure 5.1: (a) Block diagram of current recycling digital transmission line.(b) The microphotograph of the layout digital transmission line**

1. The current drawn from each circuit must be equal
2. The input and output must not add current to the serially biased circuits.

The inputs and outputs are connected via galvanic connection to satisfy the above requirements.

In figure 5.2, the complete schematic of the driver- receiver is shown. The driver and receiver circuits are completely different grounds (more clearly in the layout figure 5.3). An inductor connecting two Josephson junctions momentarily stores a single flux quantum while an SFQ pulse propagates from one junction to another. Typically, this duration time is about 5picoseconds, depending on the circuit parameters. Between the times when J13 and J14 generate a voltage pulses, the magnetic flux stored in the inductor that connects J13 and J14 induces a current in the inductor, L1u, connecting J1

and J2. With proper circuit parameters, this induced current causes a voltage pulse to be created on J1 and this pulse then propagates through J2 to be further processed. In this way, an SFQ signal pulse is transferred from one ground to another plane.

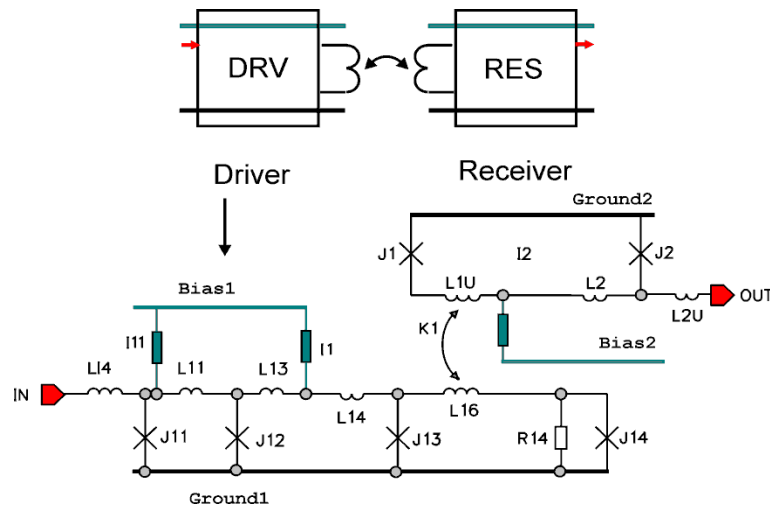


**Figure 5.2: Circuit schematic for magnetic coupled SFQ pulse transfer between driver and receiver**

In figure 5.3 the circuit layout is shown corresponding to the circuit schematic of figure 5.2. The bias current for the junction on the input side are passed to one ground plane while the ground for the junctions on the output side is isolated from the other ground by a ground plane moat. The Josephson junction J13 and J14 are damped more heavily than other junctions to guarantee that minimum reflections take place at the end of the input JTL. Tight magnetic coupling is required between the pulse transmitting the JTL and the pulse receiving JTL to obtain a robust circuit with excellent operational margins. To ensure higher coupling holes were opened in both the upper and lower ground planes as indicated. The complete block diagram for the circuit that was fabricated is shown in figure 5.4. The complete fabricated chip that was tested is shown in figure 5.5.

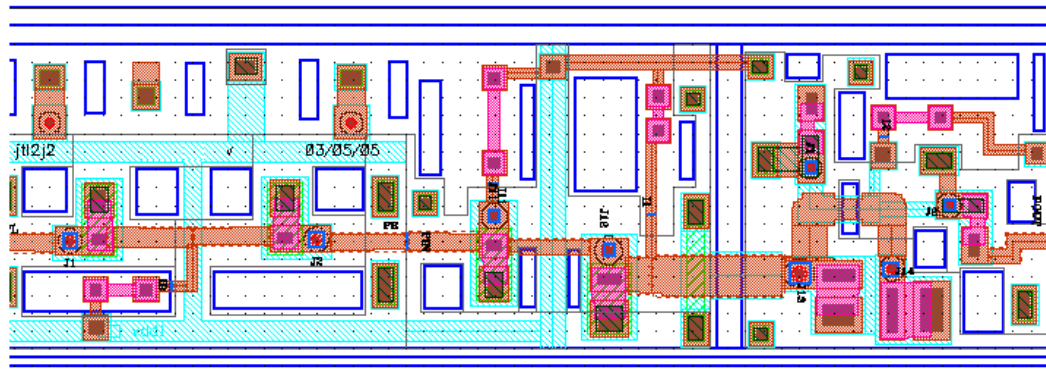


Figure 5.3: Layout for magnetic coupled SFQ pulse transfer between driver and receiver

### 5.2.1 Experimental Verification of Current Recycling

The digital traces for the correct operation of the circuit are shown in figure 5.6. The measurements were carried out at low frequency using Octupux setup. The circuit tested used the standard I/O blocks of SFQ/DC converters to measure the operating margins of the circuits. The circuits were fabricated for both 1kA and 4.5KAcm<sup>2</sup> Hypres tri-layer Nb technology. The circuit has margins of  $\pm 15\%$ . The bias current to obtain correct operation was reduced to 1.7mA; otherwise the operation of 80 blocks with parallel biasing would require nearly 200mA.

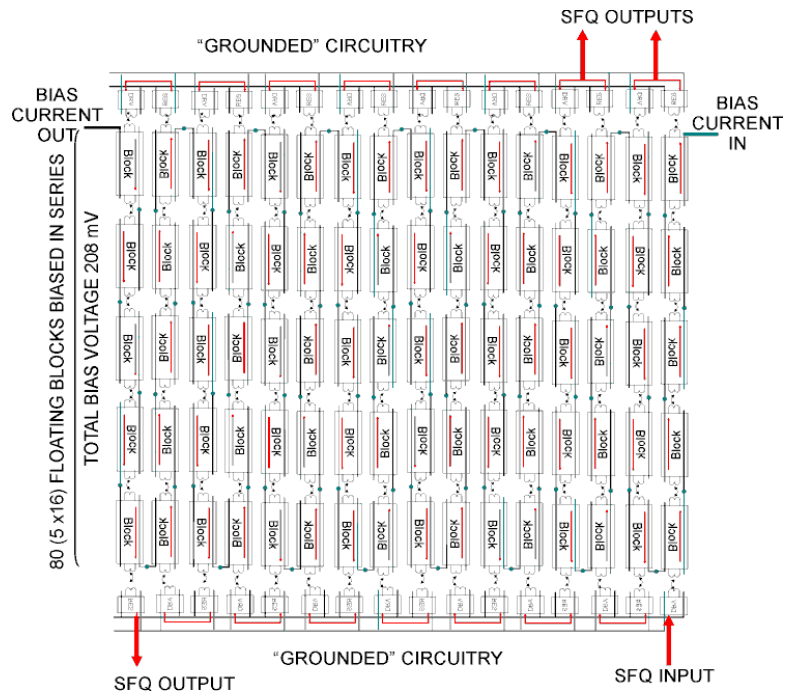


Figure 5.4: The complete block diagram of the serial biasing method.

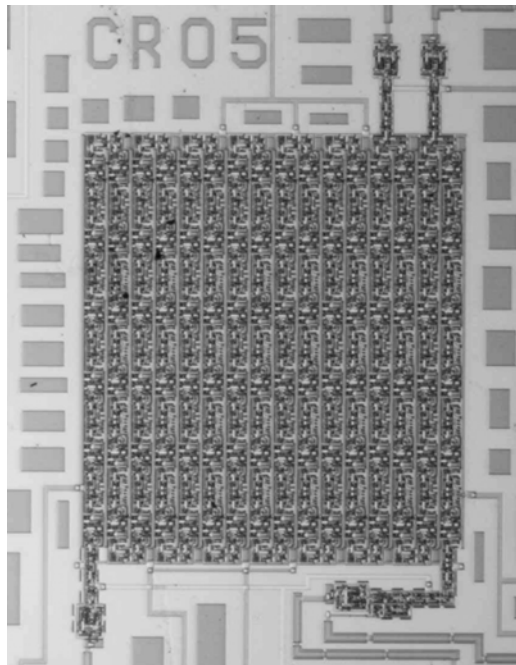


Figure 5.5: The microphotograph of the chip for demonstrating current recycling.

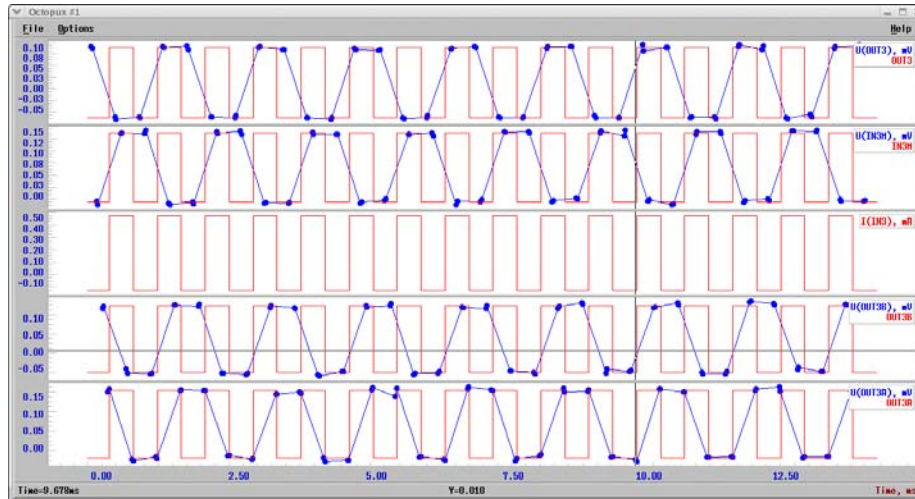


Figure 5.6: The digital waveform of the input and three outputs as shown in figure 5.4. The traces 1,3,5 are the outputs and 2 is the input trace

### 5.3 Summing Amplifier Output driver: application of floating grounds JTL

Based on the principle used in the previous section, one of the applications is designing the summing array amplifier based high frequency output drivers.

Floating Transmission Line (FTL) that receives SFQ pulses from a conventional (grounded) Josephson Transmission Line JTL (figure 5.7) is shown here. The floating grounds are based on the same principle used in current recycling, which was discussed in the previous section. However, in the digital transmission lines, like in the previous section, where the pulses were transferred, here the magnetic quantum fluxons are stored in the floating transmission block. FTL forms an outlet for a finite voltage value (by AC Josephson effect), which can be controlled by bias, and can be used as a driver when connected in serial or parallel fashion. Originally, these kinds of devices were designed to operate at relatively low frequencies. This is because of distorting effect of parasitic capacitances of each of serially connected FTLs to the ground (figure 5.8). However, this distortion could be presented as a propagation delay in a parasitic micro-strip line

composed of the parasitic capacitances and inductances of the wires connecting FTLs. For this the device has been drastically re-optimized to increase the maximum load current to 0.4 mA.

In particular, the bandwidth of the device is dramatically increased if SFQ pulses are applied to FTLs with delays  $\tau$  equal to corresponding propagating delays in serially connected FTLs. The output driver could be composed from two voltage multipliers with different gains ( $N1$  and  $N2$ ) as shown in Fig 5.8.

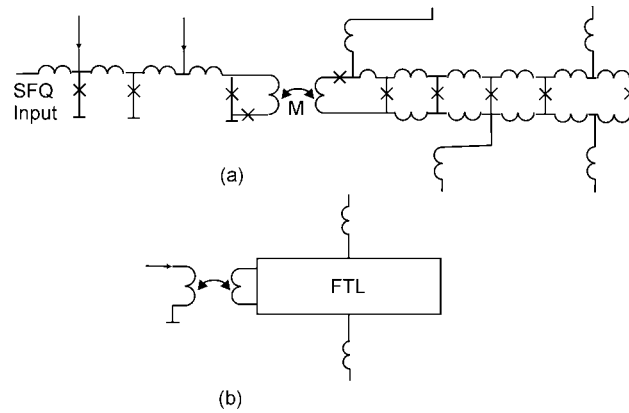


Figure 5.7: The (a) schematic of the floating transmission line and its (b) block diagram

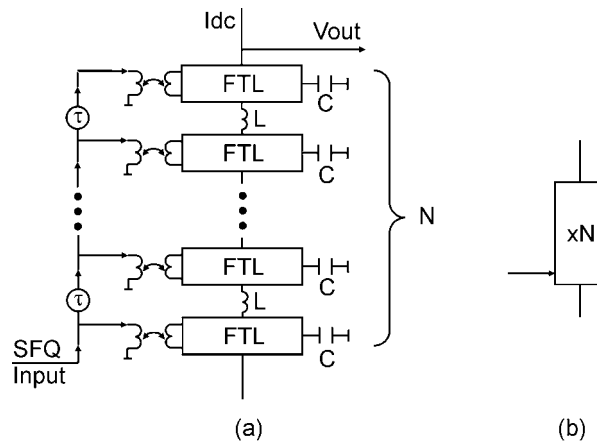
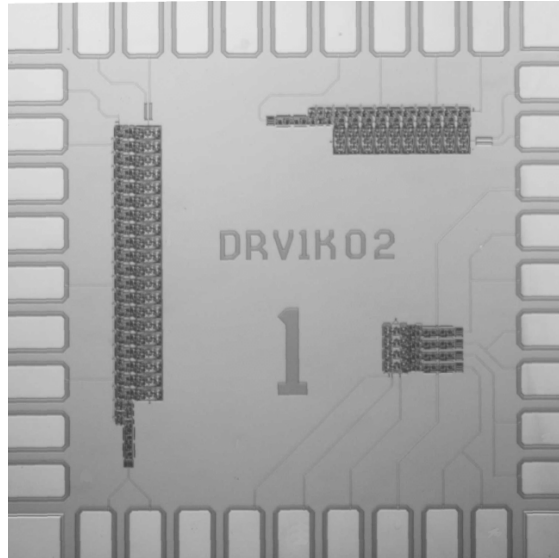
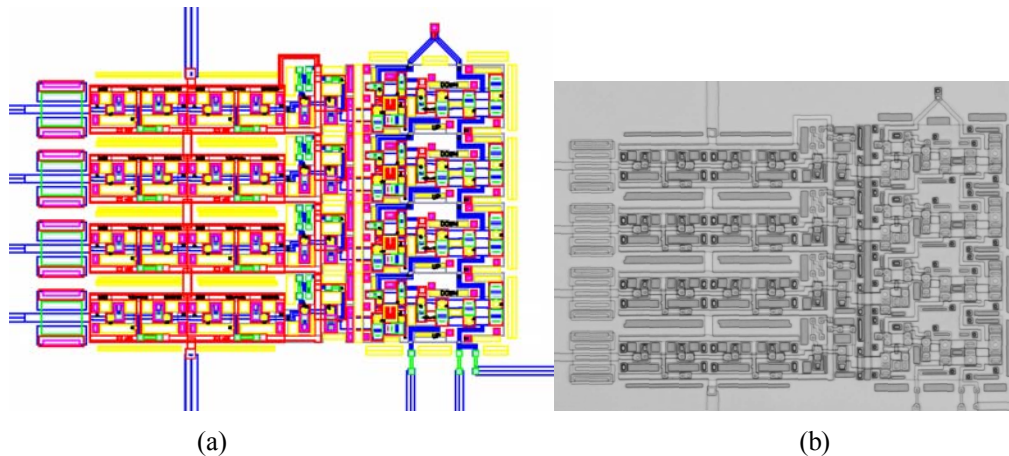


Figure 5.8: The (a) schematic of the  $N$  floating transmission lines and its (b) block diagram.



**Figure 5.9: The microphotograph of the summing amplifier based output drivers – designs based on serial and parallel connections- containing both**



**Figure 5.10: (a) The layout of the parallel connected summing amplifier based on floating transmission line. (b) Shows the microphotograph of the summing amplifier**

Figure 5.9 shows the complete microphotograph of the drivers based on summing array amplifiers. We designed three structures one is the parallel connected FTLs which has number of controls based on number of blocks-  $N$  blocks have  $N$  controls, one for each- and the layout and microphotograph is shown in figure 5.10. The other two structures are serially connected with 10 and 20 FTL blocks whose layouts are shown in figure 5.11.

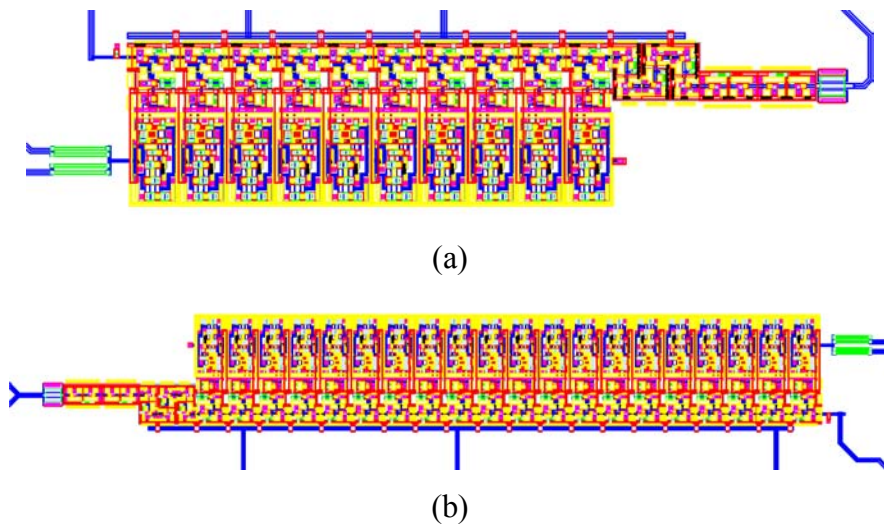


**Figure 5.11: Layout output drivers with (a) 10 floating transmission lines and (b) 20 floating transmission lines connected in series**

### 5.3.1 Experimental Results of Summing Amplifiers

The measurement results for the parallel connected summing amplifier are shown in figure 5.12. The flat Plautus region in the output traces is the optimum region for the operation of the circuits. One can see when all four FTLs are switched on the output voltage of the driver is 0.55mv with bias current margins being 0.85 mA to 0.98 mA.

The measurement results for the serially connected blocks are shown in figure 5.13 and figure 5.14 for 10 and 20 FTL blocks, respectively. The flat Plautus region in the output traces is the optimum region for the operation of the circuits.



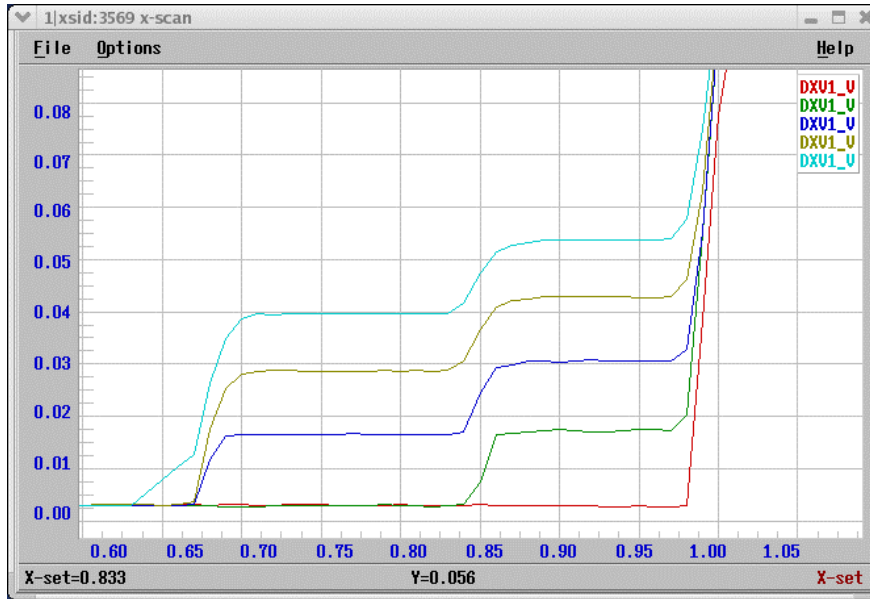


Figure 5.12: Measurements results of the driver are shown. Three inputs are operational at bias currents from 1.3 mA to 1.9 mA. One input has lower margins (from 0.85 mA to 0.98 mA). Please note that horizontal axis shows only half of total applied bias current

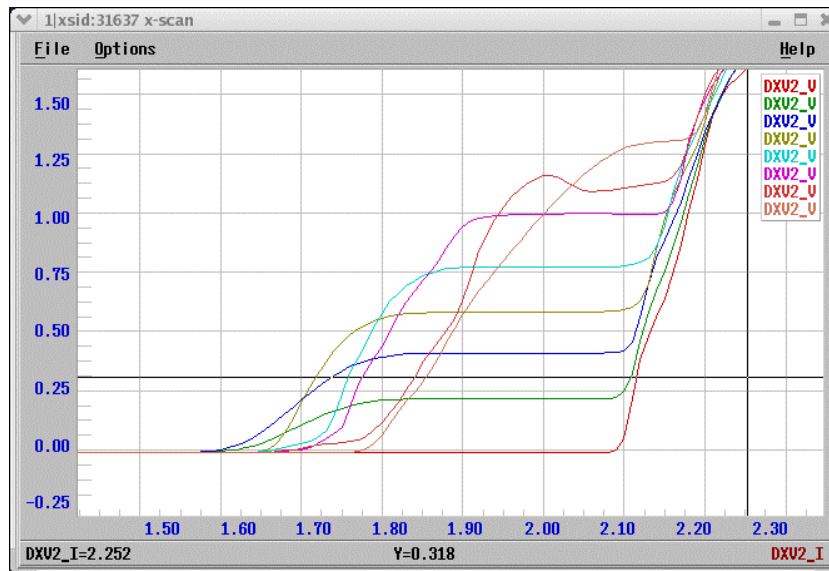


Figure 5.13: Measurement of output voltage of the driver shown as a function of bias current. It is easy to see that at nominal bias (2.0 mA) the load circuit could be from 0 ma to 0.5 mA

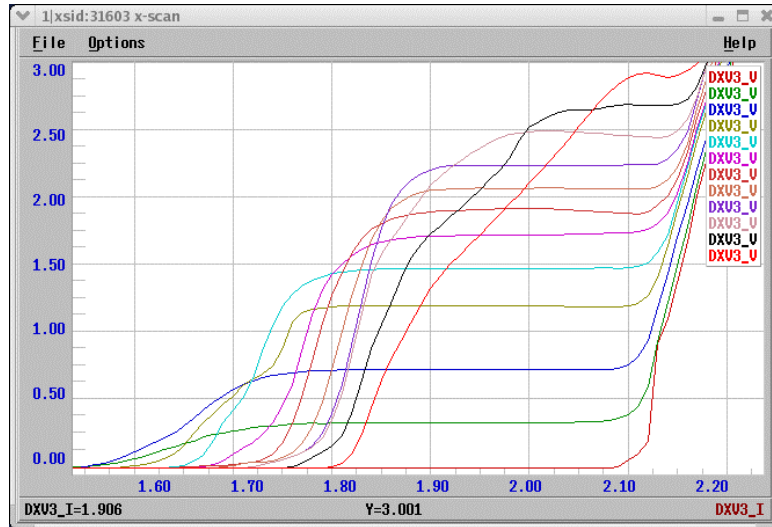
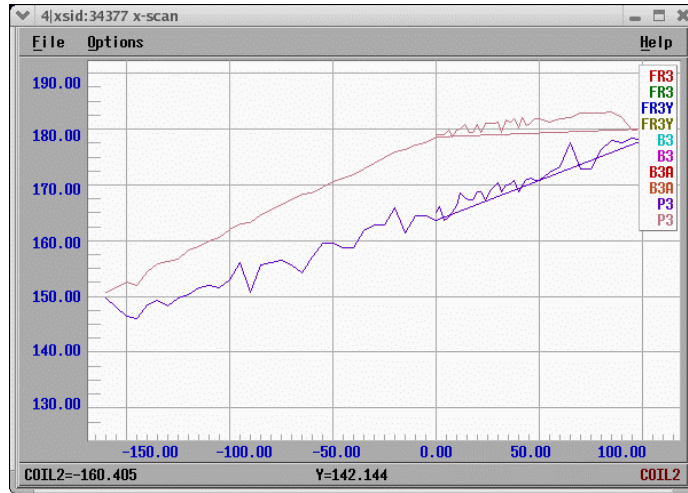


Figure 5.14: Measurement of the driver with 20 FTLs. The driver operates at bias current from 1.5 mA to 2.0 mA 4k

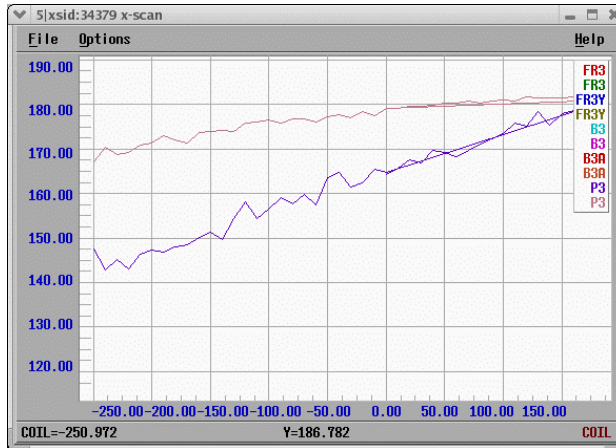
## 5.4 Effect of External Magnetic field

The circuits -current recycling based JTLs and summing array amplifiers - were analyzed for the effect of parasitic residual magnetic field on the operating margins of the circuit. With the available 3D setup developed from previous experiments [chapters 2, 3] was used. The application of magnetic field one can determine, the structure of the fabricated circuit, defects in fabrication and the magnetic properties of the circuit.

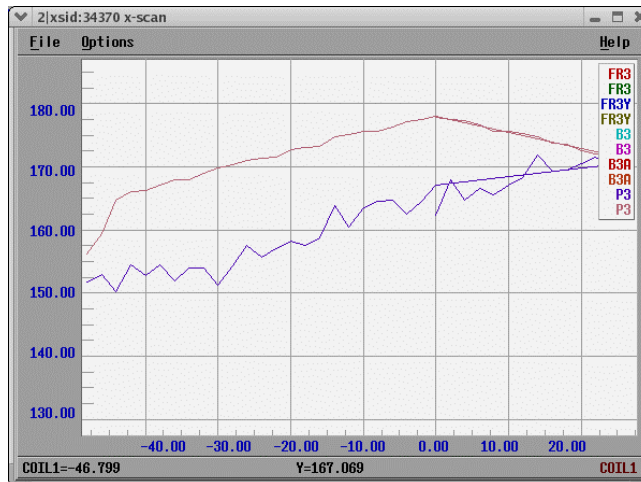
The circuit is still under active research but preliminary results show asymmetric effect of on the margins of the circuit. The figure 5.15 shows that affect of the parallel fields in both parallel directions and the normal direction.



(a)



(b)



(c)

Figure 5. 15: The affect of magnetic field on margins of the operations. (a) x-axis ,(b) y-axis and (c) z-axis, are the direction of the magnetic field applied to the circuit as shown

The asymmetric effect is assumed due to internal structure of the fabricated circuit. The circuit can be considered to be similar to a superconducting loop. The orientation of the loop can be estimated by the scanning the magnetic field over the entire horizontal plane (rotational magnetic field). This fact of single loop imitation or a number of loops orientated in the same manner is confirmed by figure 5.15, which shows the rotation of magnetic field due to both coils, a sine wave is obtained (so it can be considered as a single coil or many coils in the same orientation ). The magnetic field coefficient that was applied on the X and Y axis were of the or  $B_x, B_y = 6.4\text{mG/mA}$  and  $B_z = 1.5 \text{ mG/mA}$ .



**Figure 5.16: Margins of the circuit due to the scan of 360 degrees of magnetic filed. The orientation of the chip to the axis of the magnetic field is also shown as reference**

The orientation of the coil can also be determined. In the figure 5.16 is the best angle, the angle at which the margins are same when no external magnetic is applied, is determined. This angle is set and the amplitude on both coils was scanned simultaneously. The best angle is approximately determined from calculations

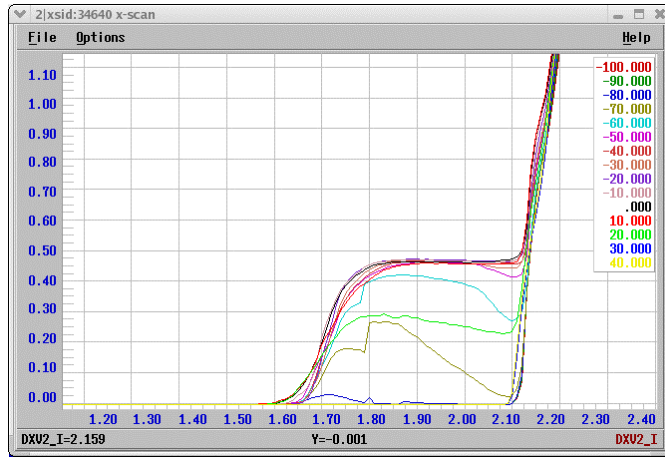
(around  $(180 - 165) = 15$  degree from x-axis). The orientation of the applied field for XY in figure 5.16 was with amplitude 128mG.

#### **5.4.1 Impact of Magnetic Field on 10-stage FTL Based Output Driver**

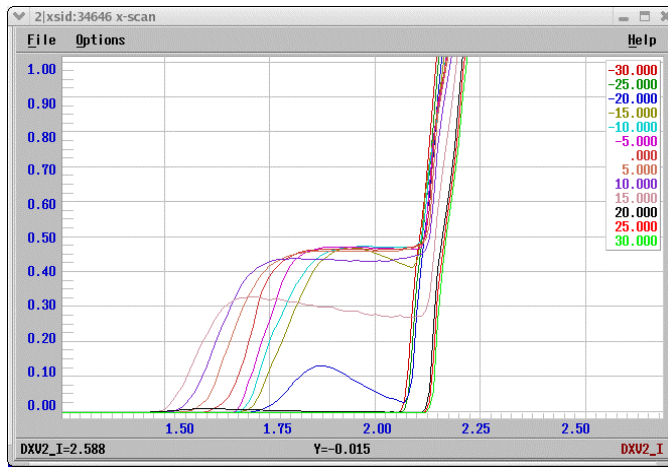
The experiments were carried out in the similar fashion as the current recycling ICs and the output voltage of the driver was noted. The circuit is most sensitive in the Y direction and least sensitive in the Z direction. The result is clear from the plots in figure 5.17. The magnetic field coefficient that was applied on the X and Y axis were of the order  $B_x, B_y = 6.4\text{mG/mA}$  and  $B_z = 1.5 \text{ mG/mA}$ .

### **5.5 Conclusion**

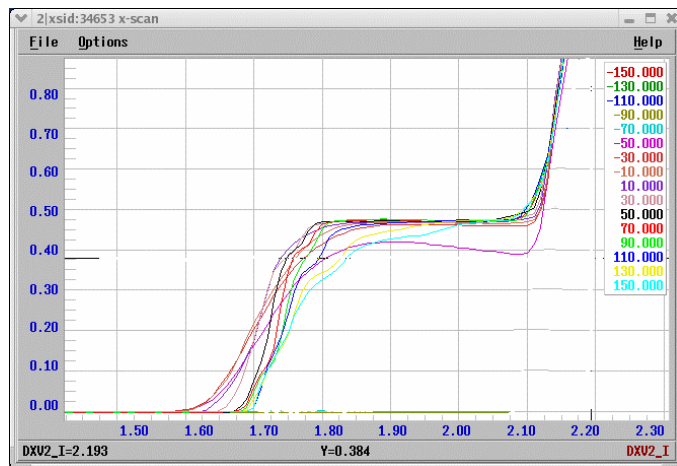
The current recycling technique for serially biasing RSFQ cells for large scale integration of RSFQ circuits is explored here. The application of current recycling based principles was used to design output drivers. The sensitivity of SFQ cells to magnetic field caused by external magnetic field or by normal operation of (many) other cells in proximity was noted. The excessive sensitivity to magnetic field could be easily hidden by other problems, which are difficult to notice without establishing experimentally.



(a)



(b)



(c)

Figure 5.17: The affect of magnetic field on the output of the driver (10 serially connected FTL) operations. (a) x-axis ,(b) y-axis and (c) z-axis, are the direction of the magnetic field applied to the circuit as shown.

## **Chapter 6**

### **Multi-Chip Modules**

#### **6.1 Introduction**

It has been demonstrated now that superconducting microstrip lines (MSLs) [90] are able to process and transfer digital data with rates up to several hundred GHz [85,86]. The complexity and functionality of Superconducting ICs are limited by the logic cell density or, crudely, by the number of Josephson junctions (JJs) which can be placed on a single chip. For the existing IC fabrication technologies (see, e.g., HYPRES 4.5 kA/cm<sup>2</sup> Josephson critical current density process [81,82,83,84]), the maximum circuit density is  $\sim 2 \times 10^4$  JJs per chip. To increase the chip functionality one of the convenient ways to increase the complexity is the use multichip module (MCM) technology otherwise commonly known as flip-chip technology. For MCM technology to be viable, the modules require transferring data between the two superconducting ICs at the same or similar rates as on-chip, i.e. up to several hundred Gbit/s and beyond. In collaboration with Hypres Inc, we developed the new technology for the development of the inter-chip connection for ultra-high data transfer rate.

#### **6.2 MCM Modeling**

As mentioned above the MCM contains two superconducting IC connected together with a bump. The microstrip lines, power lines and the ground bumps have to be assembled in a manner that causes least scattering during data transfer between the two chips. The best configuration is illustrated in figure 6.1.

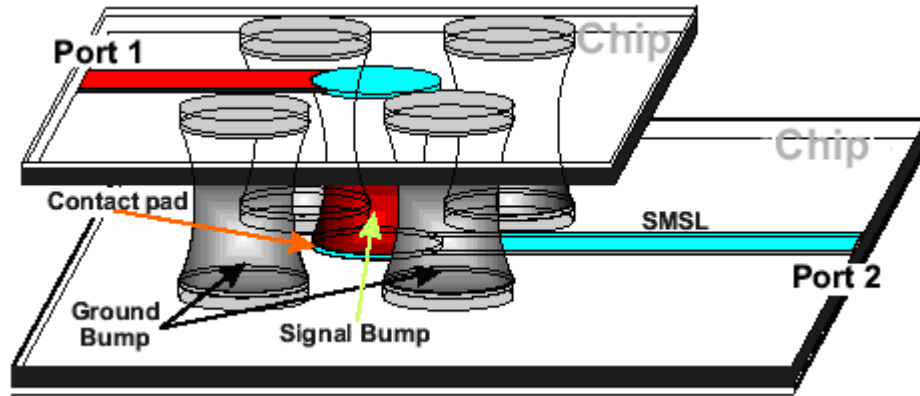


**Figure 6.1: Structure of a wide-band chip-to-chip connection. Signal bump (in the center) is surrounded by 4 ground bumps [17]. (Courtesy R. Rafiq)**

The figure 6.1 shows the complete structure of MCM, where two chips have to connect such that parasitic in the entire structure has to be at the lowest to reduce the effect of resonances. The model of the MCM can be represented by a simple PI model as shown in figure 6.2. An advantage of using this model is that it is convenient for extracting the parameters for designing the bumps and easy for simulations. The simulations were carried out using SONNET software for estimating the parameters of the bumps.

In all the existing MCM bump structures we found that the parameters that could most affect the performance are the inductance of the bump and the capacitance between the two signal pads of the signal bump between the two chips.

Our simulation results showed that the resistance of the bump is small and not influential to reduce the performance of the MCM. The existing structure [17,55,64], the resonant frequency, a deterrent to optimal performance, is much lower due to relatively high values of inductance and capacitance of the bump. To increase the resonant frequency the parasitic, inductance of the bump and capacitance between the two chips have to be reduced.



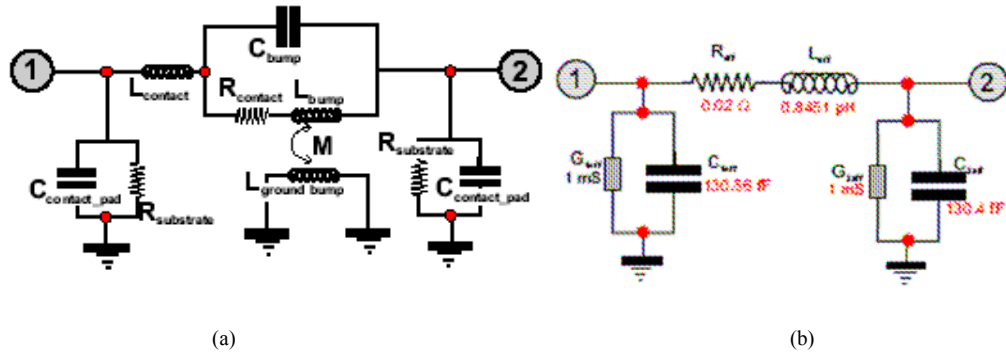


Figure 6.2: (a) PI model with all the parasitic components is shown. (b) PI model used for simulation.

The pi model in figure 6.2b, with the values indicated, was used for simulation and we obtained resonant frequency of around 72GHz, as indicated in figure 6.3.

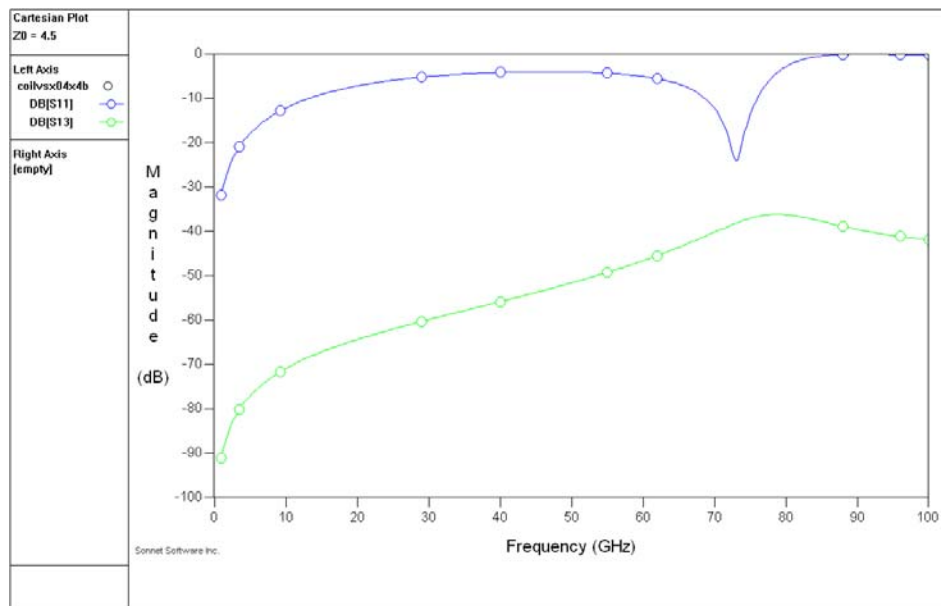


Figure 6.3: Scattering parameters S11 and S21 for the pi model in figure 6.2b

### 6.2.1 New Bump Structure

The arrangement of signal and ground contacts for inter-chip communication is a peripheral array shown in figure. 6.4. Each signal contact is surrounded by four ground contacts which can also be shared with the next signal contact. The signal (data) is coming along a microstrip line (width  $w$ ) formed in one of the superconducting layers and

marked **MSL** in figure. 6.4. The bumps are formed in the centers of the signal and ground contact pads. Their diameter is smaller than the diameter of the contact pads. The microstrip line impedance is matched to a load or a driver at the other end of the microstrip line [46,47]. Conventional solder bumps have relatively large parasitic inductance,  $L_p$  that is acceptable for relatively slow semiconductor devices having a high, typically  $R = 50\Omega$ , impedance. However, high parasitic inductance is not acceptable for a low-impedance, typically  $\sim 2\ \Omega$ , and superconductor devices operating at about 100 GHz data rate. This is because the bump inductance limits the cutoff frequency for signal transmission through the bump,  $\omega_{cf}$ , which can be crudely estimated as

$$\omega_{cf} \sim \frac{R}{L_p}. \quad (6.1)$$

The parasitic inductance can be reduced by reducing the contact pad size  $R1$  (figure. 6.4). This approach however has evident technological limitations if the bumps are formed by manual solder wetting. Besides, this reduction is rather small because it is proportional only to  $\ln(R1)$ . Another known approach is to compensate the series parasitic inductance by a proper parallel capacitor [46]

$$C_c = \frac{L_p}{R^2}. \quad (6.2)$$

However, the cutoff frequency for this solution is limited by the resonant frequency, giving the same answer as

$$\omega_r = 1/\sqrt{L_p C_c} = R/L_p \quad (6.3)$$

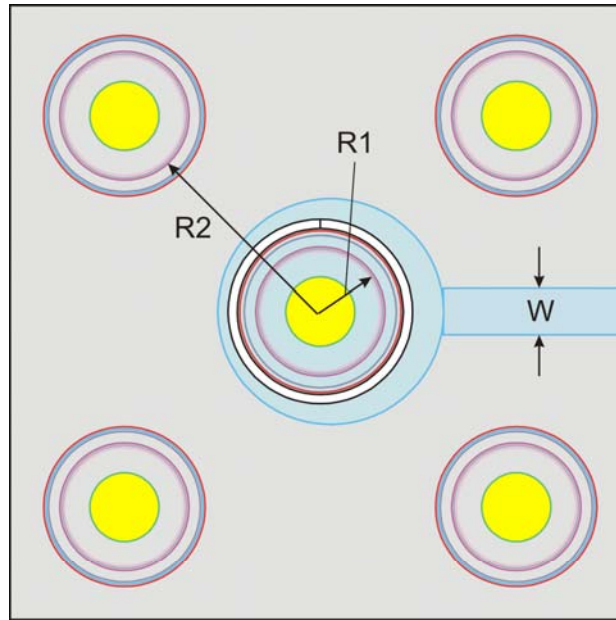


**Figure 6.4: Structure of a wide-band chip-to-chip connection. Signal bump (in the center) is surrounded by 4 ground bumps. Bumps are deposited into the centers of Nb contact pads. Superconducting microstrip line (MSL) is connected to the signal bump. It has a specially shaped end overlapping a cut in the ground plane in order to provide impedance matching and increase the transmission bandwidth.**

Our new interconnect design actively utilizes advantages of several metallization levels common for superconductor integrated circuit technology. The ground plane bumps occupying corners in figure 6.4 provide galvanic connections between the ground plane layers on the MCM substrate and on flip chips. Their contact pads contain all superconducting layers (from M0 to M3 in the HYPRES process) mutually connected via contact holes in isolating layers. The sequence of metal layers in the signal contact pad is identical to those of the ground contacts. However, the patterns of the layers and therefore the bump properties are original. First, the signal contact pad is isolated from the ground plane by a narrow disk-shaped moat shown in white. The microstrip line is galvanically connected to the bump. Second, the bump end of the microstrip line is shaped such that it overlaps the ground plane moat and behaves as a line with gradually

reducing width. One of the possible implementations of this transition is a “misaligned” circular end shape formed in the same M2 layer as the microstrip, as shown in figure 6.4.

The complementary signal bump located on the MCM carrier has exactly the same design but is just mirrored with respect to the y-axis. As a result, the whole structure after flip-chip bonding behaves almost as a uniform microstrip line which has a transition in the z-direction from the MCM carrier (substrate) onto the flipped chip. Of course, the transition creates a parasitic inductance in the vertical z-direction. But for this geometry it is small and easy to calculate as

$$L_p = L_w \cdot N \quad (6.4)$$

where the sheet inductance  $L_w = \ln(R2/R1)/2\pi$ . Magnetic gap,  $t_m = t + 2\lambda$ , where  $\lambda$  is magnetic field penetration depth, is the only parameter depending on the spacing,  $t$ , between the substrate and the flip chip, i.e. on the bump height. It crudely equals to the distance between the ground planes on the MCM carrier and on the flip-chip. At  $t_m = 3\mu\text{m}$ ,  $L_w \approx 3.8\text{pH}$ .

Another convenient feature of the suggested design is that  $N$  depends only on  $R2/R1$  ratio and does not depend on the contact pad and bump diameters. At  $R2/R1=5$ , the number of squares equals to 0.25. As a result, the parasitic inductance is about 1 pH. Even for a very low (e.g., 2  $\Omega$ ) impedance of the microstrip line, the characteristic resonant frequency  $\omega_r$  according to eq. (6.3) is about  $2 \times 10^{12}$  rad/sec corresponding to the cutoff frequency of about 300 GHz. In practice, the cutoff frequency can be even higher. This is because the parasitic inductance  $L_p$ , is not a lump element but is distributed along the microstrip line with varying width. The distributed inductance can be compensated by a distributed capacitance. In the design, this compensation is achieved by widening the

microstrip line's end and increasing the overlap with the ground plane. The interconnect geometry shown in figure. 6.4, includes this capacitive compensation. We adjusted the M2/MO overlap area at a fixed  $R1$  to achieve the bandwidth larger than 150 GHz. For the highest possible bandwidth, both the direct measurements and more detailed analysis should be carried out to ensure that the geometry is completely optimized.

Yet another advantage of the proposed design is that the signal contact pad, although contains the ground plane layer, is isolated from the circuit ground in the  $x$ - $y$  plane by a moat rather than by the interlayer dielectric in the  $z$ -direction as is common to many conventional designs. This makes it possible to apply significant pressure to the bump during flip-chip bonding without punching through the insulation and shorting the signal bump to the ground. Also the distributed capacitance can be varied independently of the size of contact pads and bumps.

### 6.3 Test Circuit

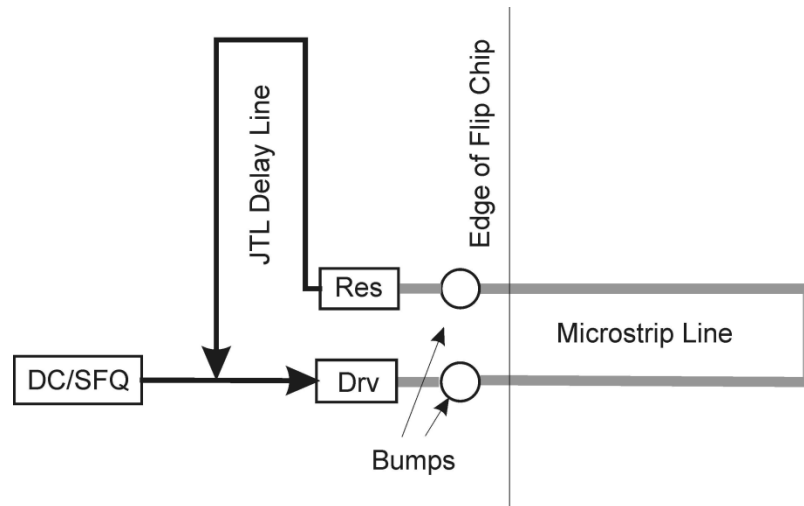
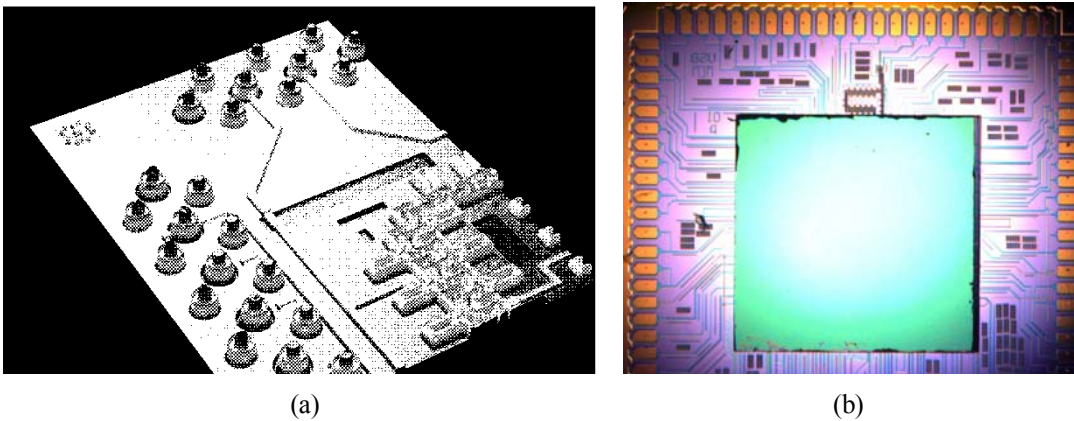


Figure 6.5: Block diagram of the ring oscillator used for testing SFQ pulse transmission between the flip chip and the active MCM carrier. SFQ driver and receiver are marked DRV and RES, respectively

In figure 6.5 shown is the design of a simple ring oscillator. The bumps intersect the microstrip line between two superconducting ICs. A simple ring oscillator consists of confluence buffer or a merger, delay controllable JTL, driver and a receiver. The frequency can be tuned by adjusting the bias current to the JTL. The choice of the frequency is a compromise between accuracy of the measured voltage and the ability to tune the frequency. The rotation frequency can be changed in strips by varying the number of circulating pulses in the oscillator.



**Figure 6.6: (a) microphotograph of the lithographically defined bumps.(b) The complete chip-set of the multi-chip module**

## 6.4 Experimental Results

Test circuits were placed on both the flip chips and the MCM carriers. Their block diagram is shown in figure 6.5. The circuits presented ring oscillators for testing transmission of single flux quantum (SFQ) pulses from the Josephson transmission line (JTL) on the chip through the bumps to the microstrip line on the carrier and back to the chip. Similarly, SFQ pulses generated on the carrier can be transmitted to the flip chip and back to the carrier. The length of the microstrip lines in different circuits was varied

from 300  $\mu\text{m}$  to 13 mm in order to see if there are any resonances or other limitations on the data rates associated with the length of the microstrips.

The speed of the pulse circulation was controlled by varying the bias on the JTL as well as by the number of flux quanta inserted into the ring. For a comparison, identical circuits were placed entirely on the chip and on the carrier, so the SFQ pulses do not need to propagate through the bumps. Testing was done using an automated set-up *Octopus*[33].

Figure.6.8 shows the frequency of transmission of the SFQ pulses through the bumps in the ring oscillator at different biases of the JTL controlling the SFQ pulse propagation speed. Each curve from left to right in figure 6.7 corresponds to a progressively increasing number of SFQ pulses moving in the ring from one to sixteen. Figure 6.8 shows the margins of operation of the receiver (**Res** in figure 6.5) in the ring oscillator as a function of SFQ pulse transmission rate in the ring. The receiver is the most sensitive part of the whole circuit, so the margins on its bias current are the most representative of the circuit operation. The maximum SFQ pulse transmission rate,  $f_{\text{max}}$  observed is about 110 GHz. Figure 6.9 the operating margins of the receiver are recorded with the flip-chip made by conventional solder technology.

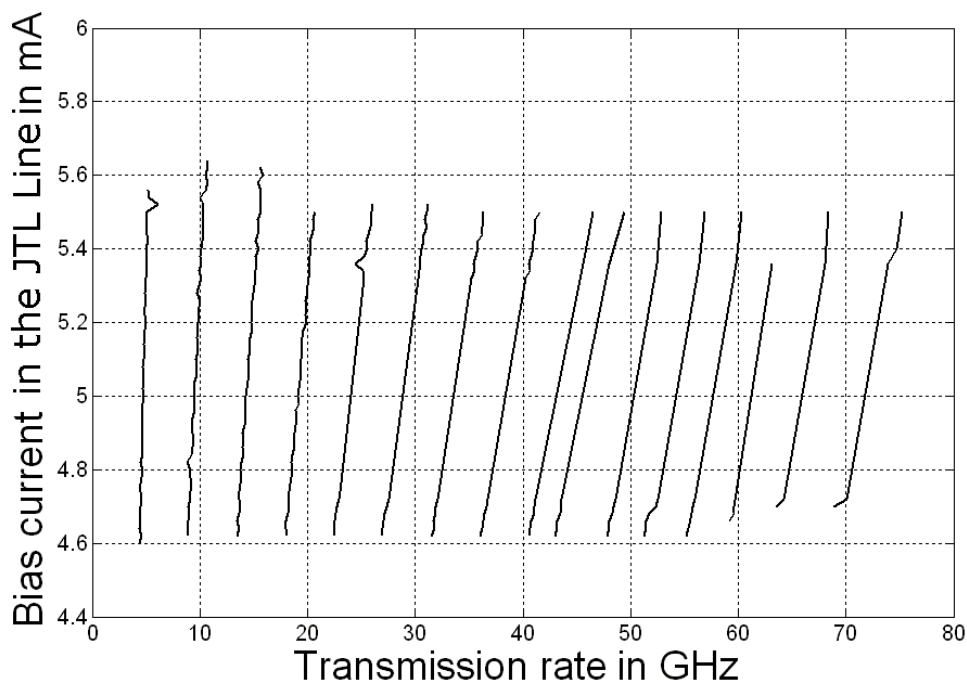


**Figure 6.7: The frequency of transmission of SFQ pulses between the flip-chip and the MCM carrier in the ring oscillator at various numbers of flux quanta circulating in the ring for the typical MCM. The maximum of 16 SFQ pulses can be inserted into the ring oscillator. The speed of circulation of the pulses was controlled by varying the bias on the JTL**

Figure 6.9 shows the results for the same circuit but from a wafer bumped manually by the traditional immersion process. The  $f_{max} \sim 78$  GHz in this MCM is somewhat lower than in the previous one with the Au bumps. However, by testing the ring oscillator located entirely on the flip-chip of this MCM, we found basically the same maximum transmission rate of SFQ pulses. It means that the observed  $f_{max}$  is not limited by the transmission through the bumps but by the operation speed of the circuit itself which varies somewhat from wafer to wafer.

The reproducibility of the performance of different circuits on the same MCM is shown in two tables Table 6.1 and Table 6.2, for the two typical MCMs from two different wafers. The circuit performance was recorded for different lengths of the microstrip lines.



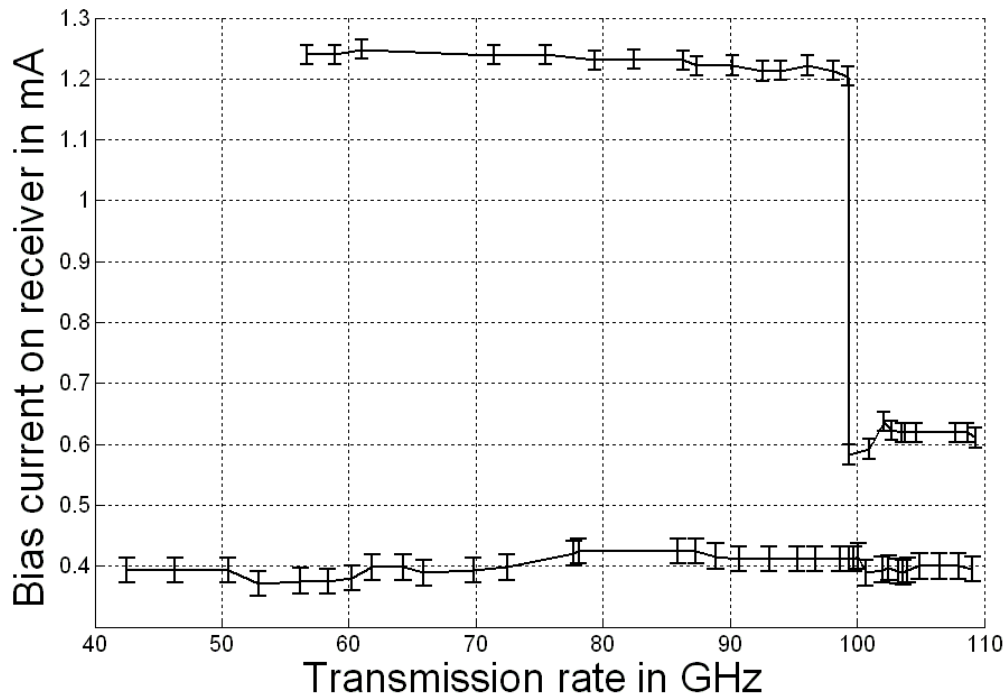


Figure 6.8: The upper and lower margins of the receiver bias current at different rates of SFQ pulse transmission between the flip-chip and the MCM carrier with Au bumps. The MSL length is 2210  $\mu\text{m}$ . The wafer was bumped using 1.8  $\mu\text{m}$  Au bumps deposited by e-beam evaporation. The MCM was bonded by a cryogenically compatible adhesive

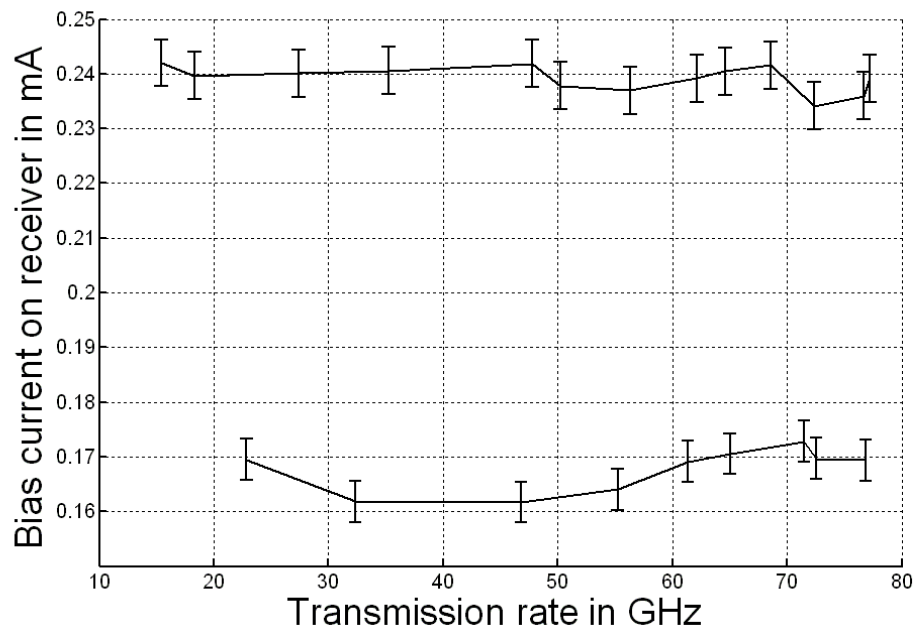
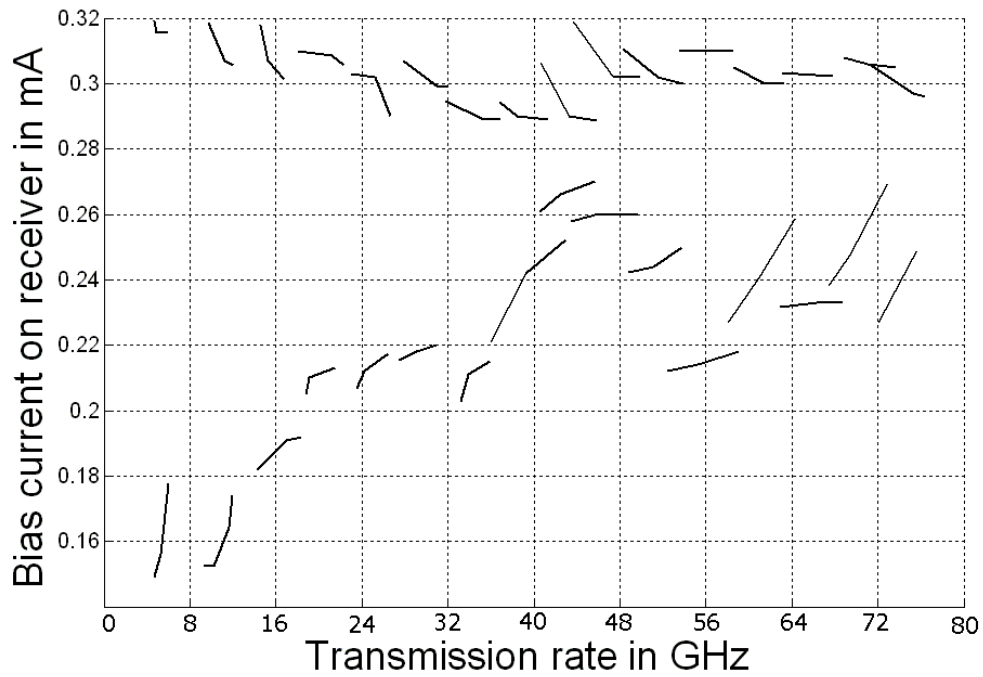


Figure 6.9: The upper and lower margins of the receiver bias current vs the SFQ pulse transmission rate between the flip-chip and the MCM carrier for InSn bumps. Both the chip and the carrier were bumped by immersion in molten InSn alloy at 150  $^{\circ}\text{C}$  and bonded by reflow and a cryogenically compatible adhesive. The MSL length is 2210  $\mu\text{m}$



**Figure 6.10:** The upper and lower margins of the receiver bias current vs the SFQ pulse transmission rate between the flip-chip and the MCM carrier for InSn bumps. Each separate branch from left to right corresponds to the different number of SFQ pulses circulating in the ring oscillator. A geometric resonance in the MSL at ~ 44 GHz can be seen. InSn bumps were used in this MCM

**Table 6.1:** Maximum transfer for MSL length in Au bumps

Wafer KL1061, bumped by evaporated 1.8-  $\mu\text{m}$  Au

|                         |      |      |      |      |      |      |
|-------------------------|------|------|------|------|------|------|
| MSL                     | 3580 | 3680 | 3760 | 3845 | 4315 | 7050 |
| Length( $\mu\text{m}$ ) |      |      |      |      |      |      |
| $f_{\text{max}}$ (GHz)  | 104  | 108  | 108  | 109  | 88   | 105  |

**Table 6.2:** Maximum transfer rate for MSL length in InSn bumps

Wafer KL1084, bumped by immersion in InSn melt

|                         |      |      |      |      |      |       |
|-------------------------|------|------|------|------|------|-------|
| MSL                     | 1900 | 2210 | 2335 | 4475 | 7650 | 12895 |
| Length( $\mu\text{m}$ ) |      |      |      |      |      |       |
| $f_{\text{max}}$ (GHz)  | 78   | 80   | 78   | 76   | 81   | 76    |

## 6.5 Discussion and Conclusion

We have developed a new inter-chip interconnect design and the wafer-level bumping process for superconductor integrated circuits, using evaporated or electroplated bumps of various compositions – Ti/Pd/Au, Ti/Pd/Cu/Au, Ti/Pd//In/Au – in order to replace the manual chip-level immersion bumping in molten InSn. A large number of MCMs containing a single flip-chip and an active MCM carrier have been assembled using adhesive and Reflow bonding processes. The maximum chip-to-chip SFQ pulse transmission rates of 110 GHz was observed for the circuits fabricated by HYPRES 4.5 kA/cm<sup>2</sup> process and using evaporated Ti/Pd/Au bumps of 1.8  $\mu\text{m}$  height. By testing the SFQ pulse transmission on-chip and chip-to-chip, it was found that the maximum transmission frequency through the bumps is not limited by the employed interconnect design or the bump metallurgy but by the maximum speed of the test circuitry. Therefore, the developed design and the whole wafer bumping technology should be well suited for the future higher  $j_c$ - fabrication processes providing yet higher operating frequencies of superconductor integrated circuits.

## **Chapter 7**

### **Design of the Multi-modulator ADC Architecture**

#### **7.1 Introduction**

In this chapter, the design of a high sensitivity ADC by implementing a multi-modulator architecture is described - with subsequent modulators sampling the time delayed version of the input signal. Superconducting Phase modulation demodulation (PMD) ADCs [78], have been successfully demonstrated to operate at 20GHz [11]. In this chapter, the design steps in the development of the multi-modulator front end will be described without going to complete detail on the study of superconducting PMD ADCs. The design and simulation results are included of the multi-modulator; LC low pass filter and Transformer here.

As the input signal applied to each modulator is correlated, the noise for each modulator is uncorrelated. Consequently, averaging outputs from multiple modulators effectively reduces the noise floor by the square root of the number of modulators used. The signal is coupled to each of the modulators by connecting the primaries of the transformers in series. Each transformer is designed as an LC transmission line, with the impedance matched to the load impedance. An LC low pass filter (1GHz cutoff frequency) is also used before each modulator to remove the high frequency noise components

#### **7.2 Behavioral System Simulation of Multi-modulator ADC**

A Simulink model, as shown in figure 7.1, of the multi-modulator ADC architecture at behavioral level was constructed, to examine the properties of the system. With a system level simulation it was shown that a 3 db dynamic range improvement was

achieved for every doubling of the number of modulators. In Simulink simulations, an LC transmission line model was not included and the signals to all comparators are applied simultaneously. In the implementation of ADC, the input signal to each subsequent modulator is delayed by the LC transmission line and a delay compensation mechanism is required before the outputs of the modulators are added in a parallel counter. The thermal noise for each comparator is modeled by adding a white noise source with different seed. The outputs from the four modulators are added in a parallel counter and the data is further processed by the digital decimation filter.

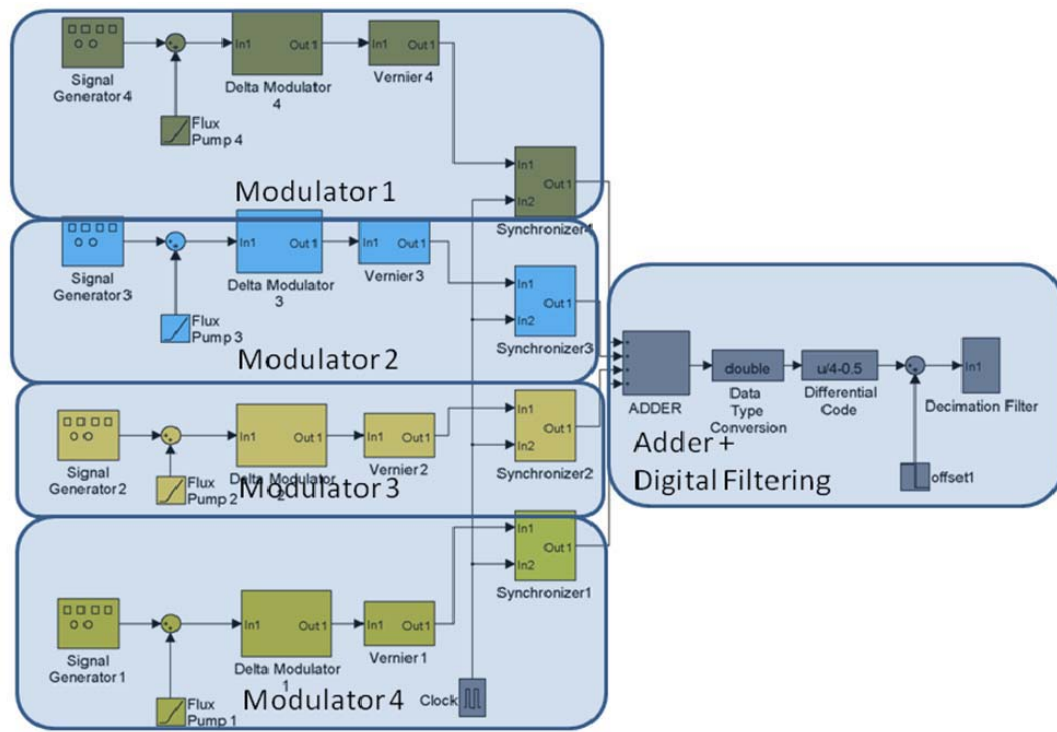


**Figure 7.1: A simulink model for a 4-modulator PMD ADC**

Figure 7.2 shows the spectrum for the 1, 2, 4 and 8 modulators. A -3dBFS, 10 MHz sine wave is applied as the input. The sampling frequency is 20.48 GHz, and the SNR is measured in 19.34 MHz bandwidth. The bandwidth was chosen, so as to not include the

second harmonic. The simulation results show a 3 dB dynamic range improvement for every doubling of the modulators.

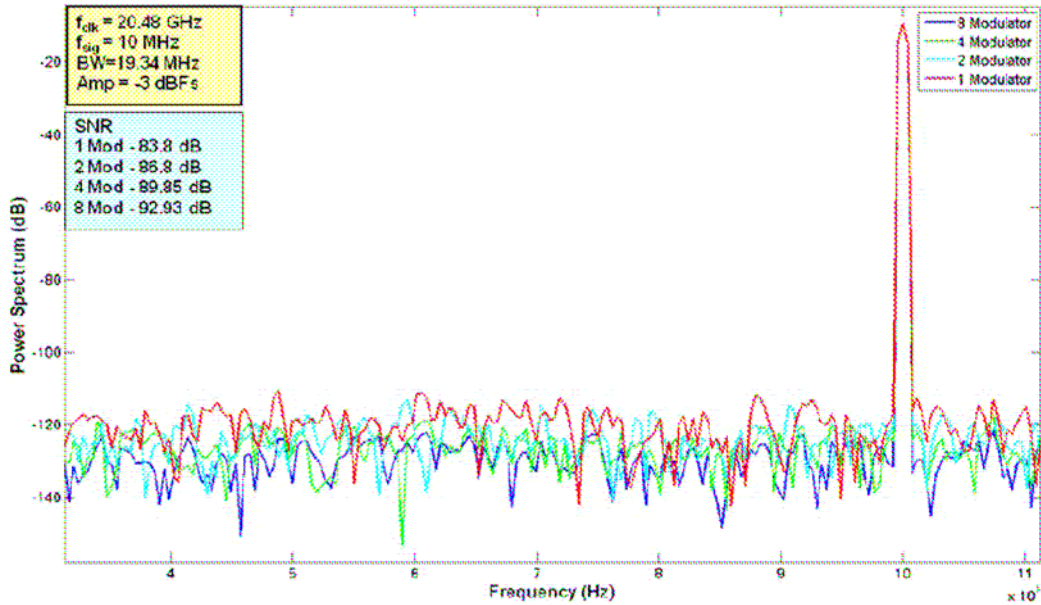


**Figure 7.2: Spectrum for 1,2,4,8 modulator PMD ADC**

Figure 7.3 shows the improvement of performance over a range of input signal- by plotting SNR versus Signal power. An SNR improvement over a range of input signal power was observed. A 9db dynamic range improvement is obtained by using an eight Modulator ADC over a single modulator ADC.

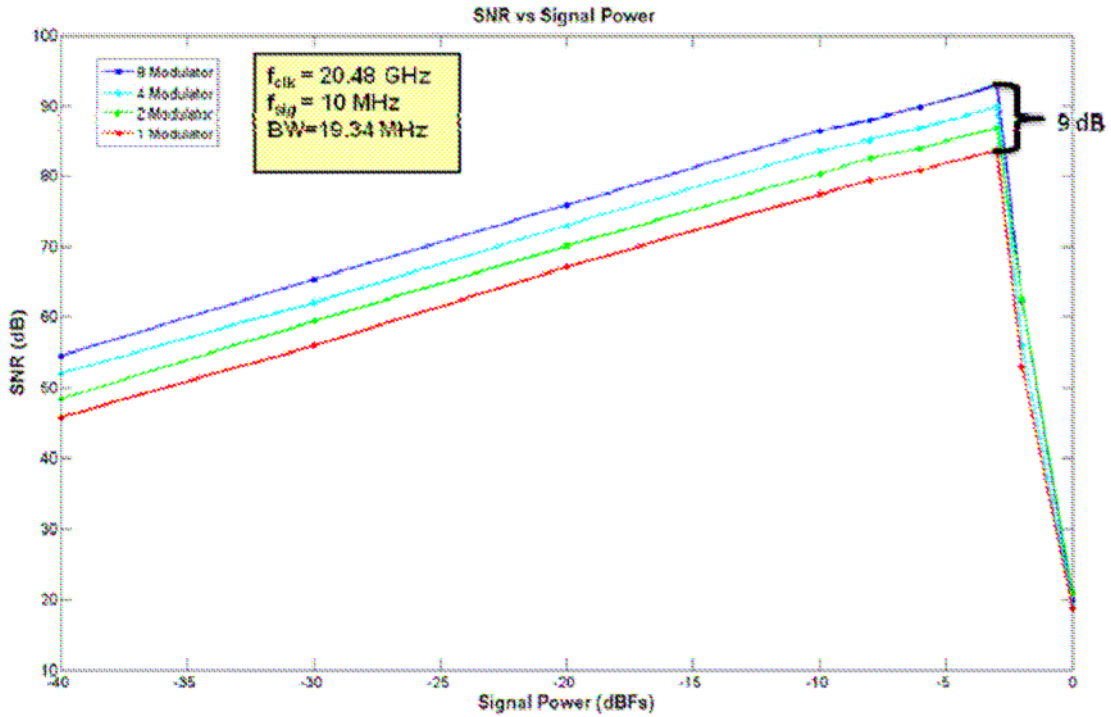


Figure 7.3: SNR (dB) versus Signal Power (dBFs) of 1, 2, 4 and 8 Modulator ADC outputs

### 7.3 Circuit Level Design and Simulation

In the previous section we showed, using behavioral system level simulations, the improvements that can be obtained using multi-modulator ADC designs. However, these simulations did not include the circuit design parameters, which crucial in determining the working of the ADC.

#### 7.3.1 Determination of Circuit Parameters for ADC

The multi-modulator is being designed for cutoff frequency of 1GHz low pass front end. The other important parameters are the primary and secondary inductances of the pick-up transformer and the Low pass filter characteristics as determined as shown

$$\text{Characteristic impedance, } Z = \sqrt{L_{\text{primary}}/C} \quad (7.1)$$

Cutoff frequency, 
$$F_c = 1/2\pi\sqrt{L_{primary}.C} \quad (7.2)$$

Lower bound set by flux noise

$$\Phi_N = I_M \cdot L_{secondary} < LSB \quad (7.3)$$

Higher Bound set by  $\beta_L \sim 2\pi$  which implies  $L_{secondary} * I_c = \Phi_0$  ( $I_c = 120\mu A$ ),  $L_{sec} = 17 \text{ pH}$

$$M = \frac{LSB_\Phi}{LSB_I} \quad (7.4)$$

$$LSB_\Phi = \frac{\Phi_0}{2m\sqrt{NQ}} \quad (7.5)$$

With number of synchronization channels  $m=1$ ,  $Q =$  number of independent modulators (assume  $Q = 4$ ),  $N =$  Decimation factor (assume  $N = 64$ ). For sensitivity of -90 dBm, assuming a 50 ohm load, the sensitivity in terms of current ( $LSB_{(I)}$ ) translates to 140 nA and for sampling frequency of 20GHz, we obtain  $M=400\text{pH}$ .

### 7.3.2 Transformer Design

The Transformer pick up coil was designed, is shown in figure 7.4, and was based on spiral inductors. The values of the coil were estimated using Wheelers formula inductance formula [2].

$$R_{mean} = (R_{outer} + R_{inner}) / 2 \quad (7.6)$$

$$\text{thickness} = R_{outer} - R_{inner} \quad (7.7)$$

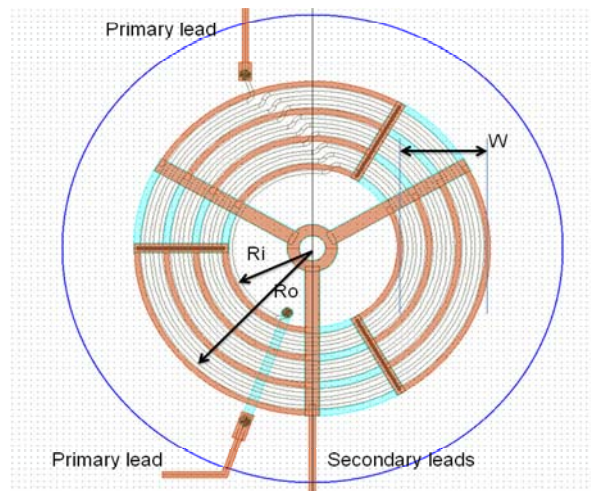
$$L_{spiral} = 3.93 \times 10^{-5} \times R_{mean}^2 N^2 / (8 * R_{mean} + 11 * \text{thickness}) \quad (7.8)$$

, where  $L_{spiral}$  (in nH), thickness (in  $\mu m$ ) and  $R_{mean}$  (in  $\mu m$ ) and  $N$  is the number of turns.

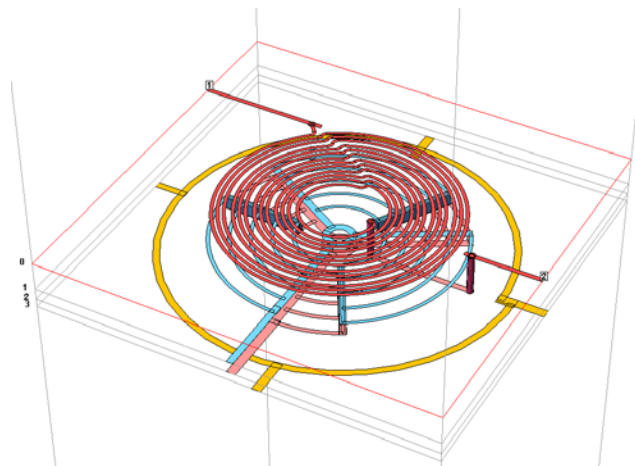
The Coil properties were extracted using SONNET, a 3D electromagnetic simulator [30]. From formula 7.6, 7.7 and 7.8, Inductance of primary coil  $L$  (primary, calculated) = 17.6nH and from sonnet simulation Inductance of primary coil,  $L$  (primary, simulated) = 16.04nH. Inductance of secondary coil  $L$  (secondary, simulated) = 19.91nH, 1st resonant



frequency from sonnet simulation observed at 3.1 GHz. From SONNET simulation we also obtain, the capacitance values; capacitance between coil and the ground,  $C=9.09\text{pF}$  and capacitance between the primary and the secondary coil is  $C_m=0.8\text{pF}$ . The Spice model schematic is constructed, from the simulations of the transformer is shown in figure 7.5.



(a)



(b)

**Figure 7.4: The Layout of the transformer coil. The Number of turns  $N=12$ , with primary inductance  $L_{pri}=27\text{nH}$  and secondary inductance  $L_{sec}=19\text{nH}$ . The inner radius,  $R_i$ , Outer radius,  $R_o$ , Width,  $W$ . (b) the 3D view of the simulated transformer( cell size  $2.5 \times 2.5 \text{ um}$ , air  $=250\text{um}$ ,  $si\_substrate=250\text{um}$ , separation from ground ring and outer coil radius  $75\text{um}$ )**

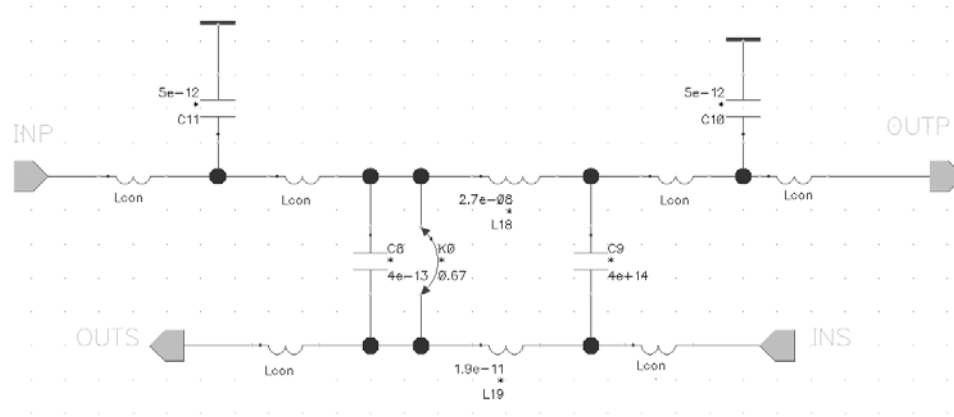


Figure 7.5: The schematic developed for the transformer based on the values extracted by 3D electromagnetic simulation of the transformer.

### 7.3.3 LC Low Pass Filter Design

A low pass 5th order Butterworth filter was designed with a cutoff frequency of 1GHz. The design characteristics of the filter are displayed along with its schematic in figure 7.6 and figure 7.7.

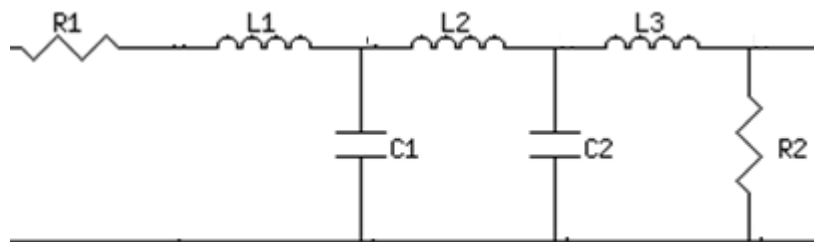
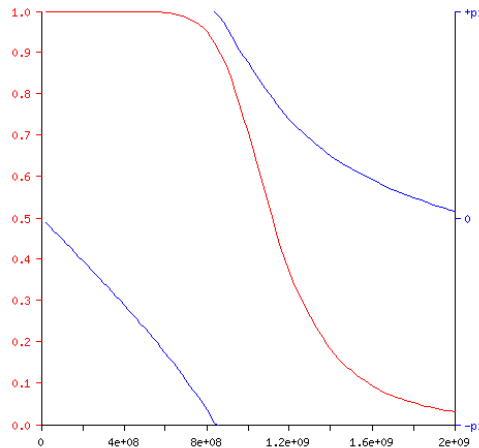


Figure 7.6: schematic of the filter,  $R1=R2=50\text{ ohm}$ ,  $C1=C2=5.15\text{pF}$ ,  $L1=L3=4.92\text{nH}$ ,  $L2=15.9\text{nH}$



**Figure 7.7: The Amplitude (normalized) and Phase characteristics of the 5th order Butterworth filter**

The inductor, for the LC filter (shown in figure 7.8a), must be based on the spiral inductor, as it is quite large compared to other RSFQ circuit elements. The spiral inductor designs, properties extracted using SONNET simulations (shown in figure 7.8b) and theoretical calculations based on eqs.7.6,7.7.,7.8, are compared and results are shown in table 7.1.

**Table 7.1: Inductance values of the spiral inductor coil for LC filter**

| Coil structure (Spiral type, layer, turns, inductor type) | Inductance (calculated) | Inductance (simulated) |
|---|-------------------------|------------------------|
| (Single l, M2, 6,L3/L1)                                   | 6.3 nH                  | 6.34nH                 |
| (Single l, M3, 6,L3/L1)                                   | 6.3nH                   | 6.48nH                 |
| (bilayer ,M2 M3,12,L2)                                    | 25.2nH                  | 23.1nH                 |

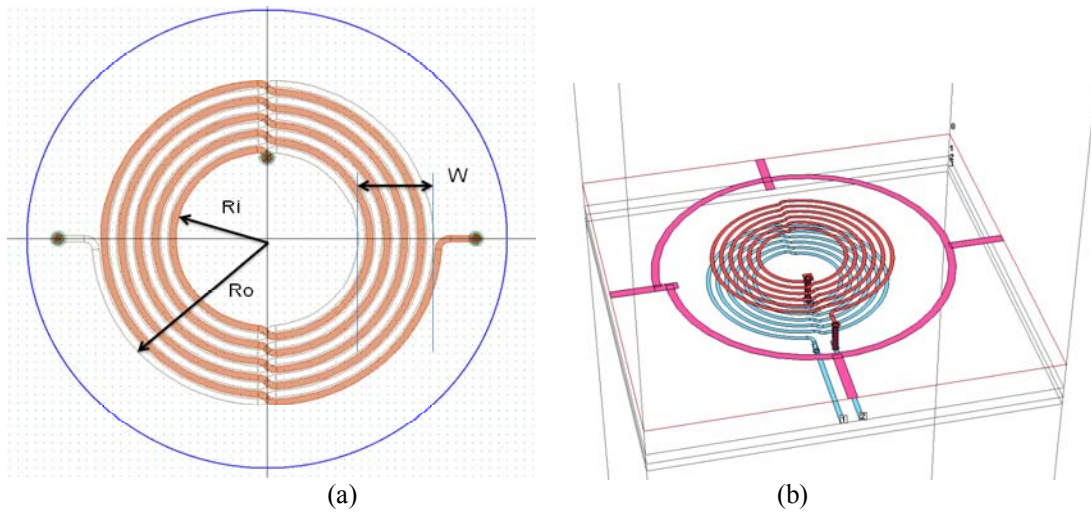


Figure 7.8: The bilayer spiral is shown above, with  $N=12$  turns. The spiral inductor is constructed with  $N=6$ , in M2 and M3 layers. The 3D view of the bilayer spiral is shown above, with  $N=12$  turns. The spiral inductor is constructed with  $N=6$ , in M2 and M3 layers. ( cell size  $2.5 \times 2.5 \mu\text{m}$  , air =  $250 \mu\text{m}$ ,  $\text{si\_substrate} = 250 \mu\text{m}$ , separation from ground ring and outer coil radius  $75 \mu\text{m}$  )

The Complete layout for the low pass LC filter is shown in figure 7.9. The Large capacitors are constructed between M2 layers and the ground layer M0, occupy an area of  $340 \mu\text{m}^2$  each.

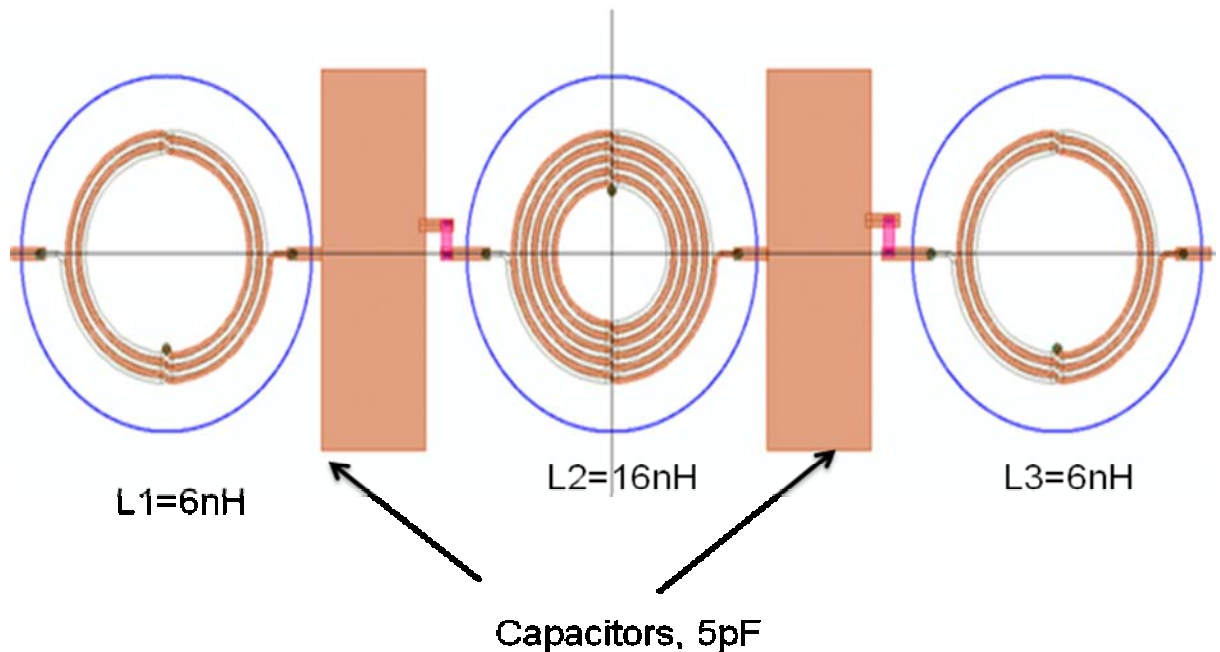


Figure 7.9: The Complete Layout of the 5<sup>th</sup> order Butterworth Low Pass filter is shown. The two capacitor are constructed between M2 and the ground layer M0

## 7.4: PSCAN Simulation of the 4-modulator ADC

We have performed circuit level simulation of the multi-modulator architecture (including the schematic models of the LC filter and pickup transformer) using PSCAN [37]. The complete schematic for the 4-modulator ADC is shown in figure 7.10. For the design specifications, the inter-modulator delay is of the orders of a few clock periods. Additional active transmission lines may be used for finer delay compensation. This variable delay capability also helps to compensate inter-modulator delay due to LC device mismatch.

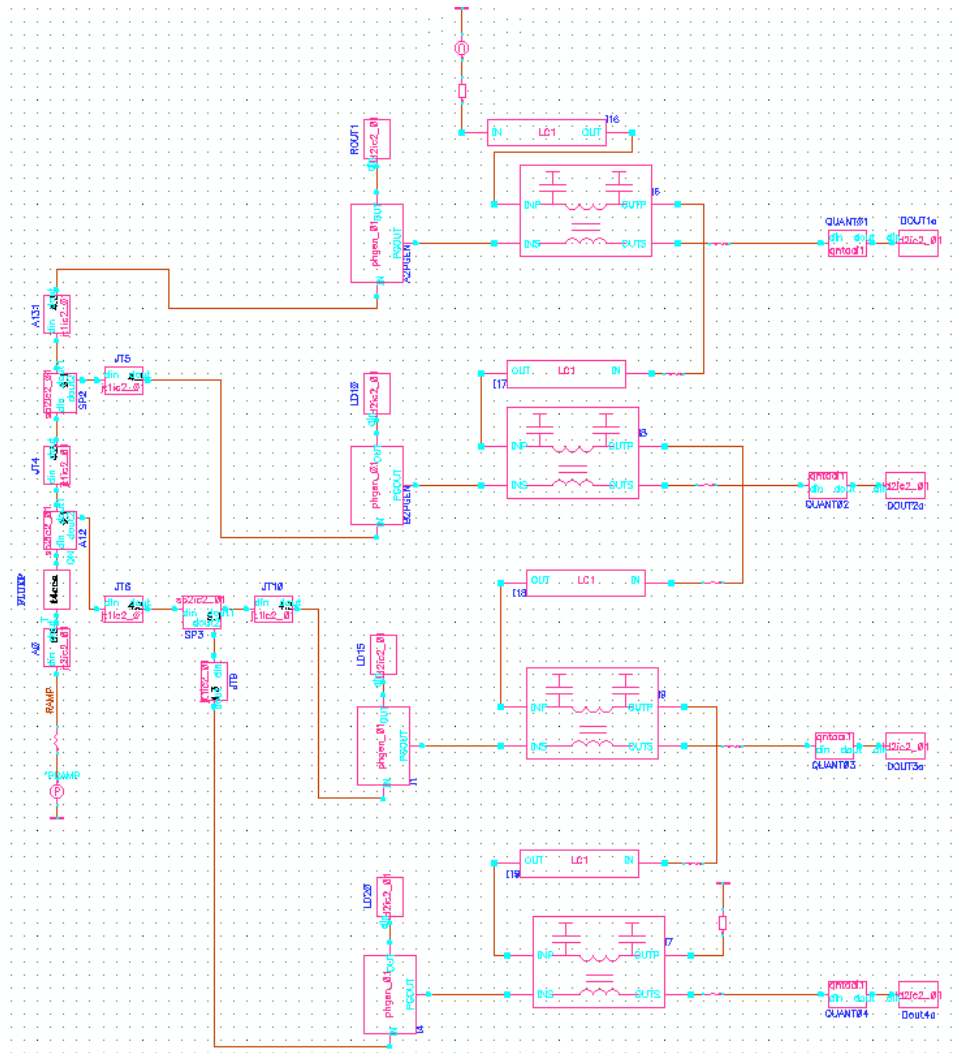
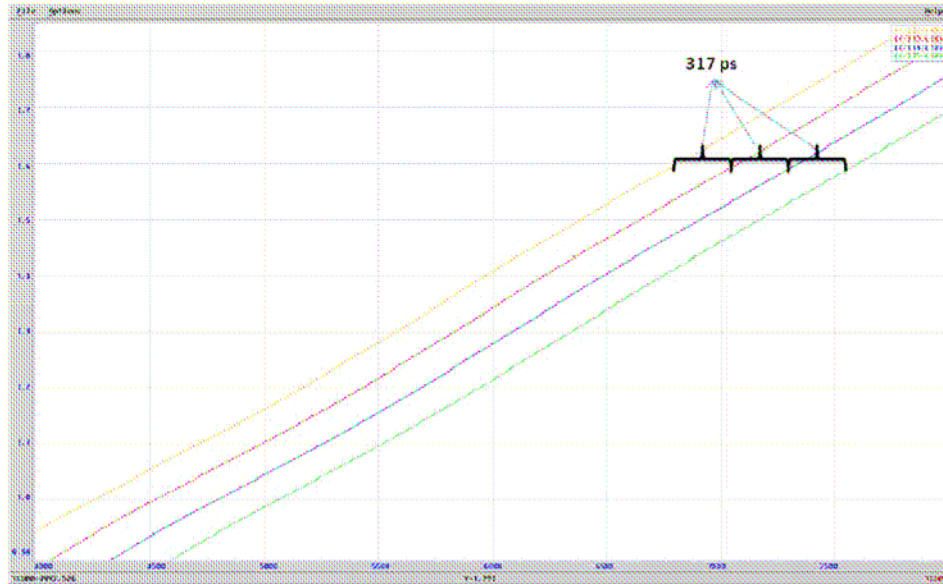


Figure7.10: schematic of the 4 multi-modulator PSCAN simulations

The current through the primary of individual modulators are plotted to show the inter-modulator delay (figure 7.11). The differentiated outputs at the end of each modulator are shown in figure 7.12.



**Figure 7.11: The inter modulator delay**

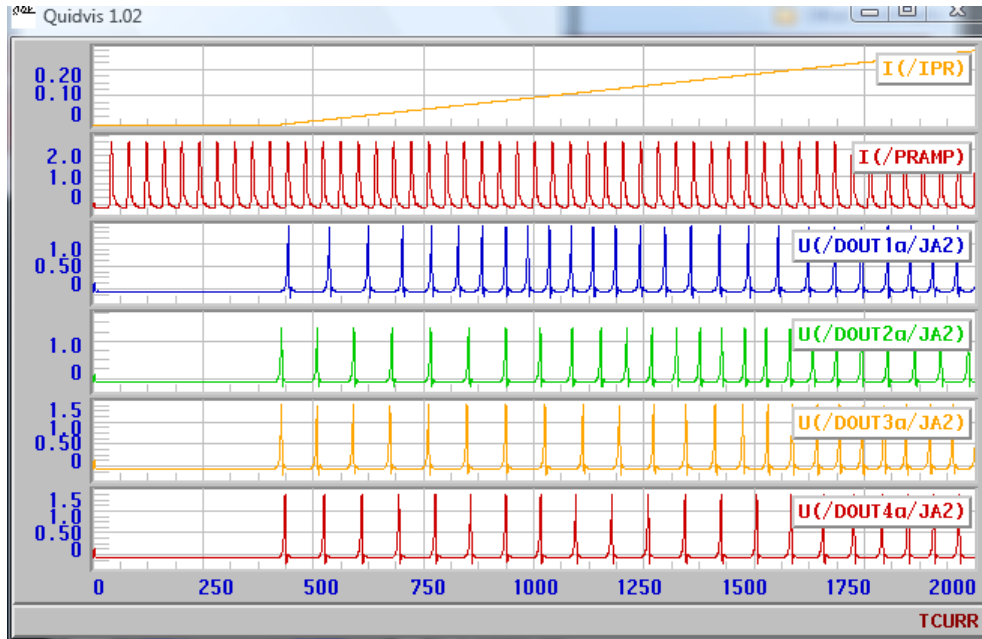


Figure 7.12: The operation of the front end of the multi-modulator ADC, the differential output pulses are shown.

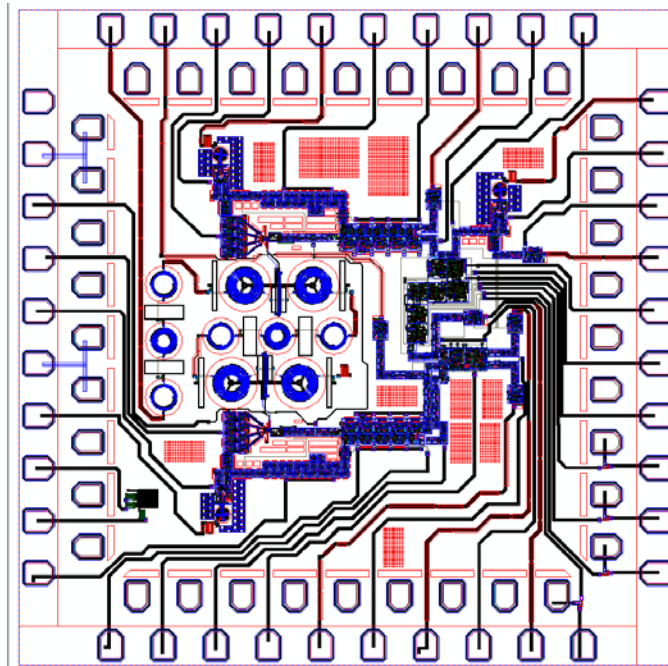


Figure 7.13: The complete layout constructed for the 2-modulator design

## **7.5 Discussion and Future work**

The multi-modulator design approach has been presented with its advantages over existing superconducting modulators. The current project of Multi-modulator ADC is still in progress. The design layout for 2-modulator ADC is shown in figure 7.13, due to the space constraints only a 2-modulator ADC could be designed in a 5x5mm chip. The future designs of the layout will include a 4-modulator design and also include a low pass multi-modulator for cutoff frequency of 100MHz front end.



## **Chapter 8**

### **Conclusion and Future Work**

#### **8.1 Conclusion**

In this thesis, the large scale integration issues of digital superconducting circuits have been presented.

##### **8.1.1 Flux Trapping:**

-A complete theoretical foundation has been revisited for analyzing parasitic flux trapping in superconducting circuit. Also, the impact of flux trapping on the operation of superconducting circuits was studied, using SONNET and PSCAN simulators.

-A complete experimental methodology, with 3D magnetic field control, has been developed for investigating parasitic flux trapping in superconducting circuits, for quantitative analysis, in both cryo-coolers and Helium Dewars. Superconducting IC's of shift registers of 16bit and 6bit were designed and fabricated for investigating parasitic flux trapping.

-A new set of moat protocols were also studied for parasitic flux trapping to determine the best layout configuration. The most resistant moat configuration has been able to prevent flux trapping upto 20mG, which is comparable to Earth's magnetic field.

-Flux trapping studies were also carried out on the power independent circuits, a logic family for low power circuits.

##### **8.1.2 Power Independent Circuits**

-A new concept of low power superconducting circuits, power independent RSFQ cell was introduced, to eliminate static power dissipation in logic gates. The circuit was

incorporated into shift register design, fabricated and experimentally tested with  $\pm 20\%$  margins.

### **8.1.3 Current Biasing**

-Demonstration of current recycling for nearly 1k Josephson junction superconducting IC with over 1000 junctions and fabricated in  $1\text{KA}/\text{cm}^2$  technology is presented. A bias current reduction of  $1/N$  was achieved, where  $N$  is the number blocks biased serially.

-Development and analysis of summing array amplifiers, for high frequency output drivers, based on current recycling technique is presented. The output drivers, constructed by parallel (4 blocks) and serial (20 blocks) connections were able to obtain upto 0.4mv and 2mV output voltage respectively, with  $\pm 15$  operating margins.

-The effect of magnetic field on current recycling circuit margins has also been reported. Some of the circuits have exhibited asymmetric operating margins for the magnetic scans.

### **8.1.4 Multichip Modules**

-We have developed a new inter-chip interconnect design and the wafer-level bumping process for superconductor integrated circuits, using evaporated or electroplated bumps of various compositions – Ti/Pd/Au, Ti/Pd/Cu/Au, Ti/Pd//In/Au – in order to replace the manual chip-level immersion bumping in molten InSn.

-The maximum chip-to-chip SFQ pulse transmission rates of 110 GHz was observed for the circuits fabricated by HYPRES  $4.5\text{ kA}/\text{cm}^2$  process and using evaporated Ti/Pd/Au bumps of  $1.8\ \mu\text{m}$  height.

## **8.2 Future Work**

### **8.2.1 Flux Trapping:**

-To study and determine the threshold fields for the layout configuration under temperature gradient during the cooling transition through the critical temperature, which can have an effect on the parasitic flux trapping.

-To design circuits resistant to flux trapping by changing the transition temperatures of all or selected individual metallic layers. The idea is to provide magnetic shielding to the next layer as the circuit is being cooled.

### **8.2.2 Low Power RSFQ - Power Independent Circuit:**

-To design power independent circuits with a memory element- single junction SQUID- with lower coil inductances.

-To design power independent circuits with higher resistance to parasitic flux trapping, by enclosing the entire circuit or part of the circuit in a superconducting shield.

-To design new circuits, such as programmable frequency divider, to study the high speed operating limits of the power independent circuits.

### **8.2.3 Current Biasing in RSFQ Circuits:**

-The current recycling circuits face limits on the scalability due to high transients in the coupling circuits. These transients can be eliminated with better design of coupling circuits and incorporating filters for the purpose which are currently under development.

-Enclosing part of the circuit in on-chip superconducting shields to make them more resistant to external magnetic fields.

### **8.2.3 Multi-chip Modules**

-To investigate the physical properties of the bumps, such as the cutoff frequency of the bumps, the resistance of the bumps. Also alternative methods of deposition of solder bumps and gold stud bumps that will guarantee better uniformity are being investigated.

-New designs must be developed to study the nature of transfer of pulses between two chips, if the bumps are of capacitive nature or inductive nature.

#### **8.2.4 Multi-Modulator ADC**

-The 4, 8-modulator ADC is yet to be designed. A multi-chip module for constructing multi-modulator ADC is a viable solution.

## REFERENCES

- [1] M. Tinkham, "Introduction to superconductivity", 2<sup>nd</sup> Edition, Dover publications, 1996.
- [2] C. W. Turner and T. Van Duzer, "Principles of Superconducting devices and circuits", 2<sup>nd</sup> Edition, Prentice Hall publications, 1999.
- [3] Alan M. Kadin, "Introduction to Superconducting Circuits", Wiley-Interscience; 1 edition, March 11, 1999.
- [4] K.K.Likharev, "Dynamics of Josephson Junctions and circuits", Gordon and Breach publishers, 1985.
- [5] John Clarke and Alex I. Braginski (Edited), "The SQUID Handbook", Wiley-VCH publications, 2004.
- [6] V.V Schmidh, "The Physics of Superconductors", P. Mueller and A.V. Ustinov, Eds. Berlin, Germany: Springer-Verlag, 1997.
- [7] Alexander. V. Rylyakov, "Ultra-low-power RSFQ Devices and digital autocorrelation of Broadband Signals", Ph.D. Dissertation, SUNY Stony Brook, May 1997.
- [8] K.K. Likharev and V.K. Semenov, "RSFQ Logic/Memory Family: A new Josephson-Junction Technology for sub-Terahertz-clock-frequency digital systems", *IEEE Trans. Appl. Supercond.*, Vol 1, No. 1, March 1991.
- [9] K.K.Likharev, O.A. Mukhanov and V.K. Semenov, "Resistive single flux quantum logic for Josephson-junction technology", *SQUID 85*, Berlin, Germany 1985.
- [10] "Superconducting Technology Assessment", Report of national security agency, office of corporate assessments, August 2005.
- [11] O. A. Mukhanov, D. Gupta, A. M. Kadin, and V. K. Semenov, "Superconductor Analog-to-Digital Converters," *Proceedings IEEE*, vol. 92, no. 10., pp. 1564-1584, Oct. 2004.
- [12] M.A, Nielsen and I.L. Chuang, "Quantum Computation and Quantum Information", Cambridge University Press, Cambridge, 2000.
- [13] D.K. Brock, E.K. Track and J.M. Rowell, "Superconductor ICs: The 100-GHz second generation", *IEEE Spectrum*, vol 37, Dec 2000, pp 40-46.
- [14] S.R. Norsworthy, R. Schreier, and G.C. Temes, "Delta-Sigma Data Converters: Theory, Design and Simulation", *New York: IEEE Press 1997*.
- [15] J.F. Bulzacchelli, "Superconductor Bandpass Delta-Sigma Modulator for direct Analog-to-Digital Conversion of Microwave Radio", Ph.D. dissertation, Massachusetts Inst. Tech., Cambridge, 2003.

- [16] T.V.Fillipov,S.V. Pflyuk,V.K.Semenov and E.B.Wikborg,” Encoders and decimation filters for superconductor oversampling ADCs,” *IEEE Trans Appl. Supercond.*, vol 11, pp 545-549, Mar 2001.
- [17] R. Rafique,” Superconducting High Speed Passive Interconnects,” Ph.D. dissertation, Chalmers University of Technology, Goteborg, Sweden, 2007.
- [18] P.Bunyk, K.K. Likharev, and D. Zinoviev,” RSFQ technology: physics and deivces,” *Int. J. High Speed Electron. Syst.*, vol.11, pp.257-305, 2001.
- [19] L.A. Abelson and G.L. Kerber,” Superconductor Integrated Circuit Fabrication Technology,” *IEEE Proceeds.*, vol 92, no. 10, pp.1517-1533,Oct. 2004.
- [20] M.A. Washington and T.A. Fulton, “Observation of flux trapping threshold in narrow superconducting thin films”, *Appl. Phys. Lett.*, vol. 40, pp. 848-50, 1 May 1982.
- [21] S. Bermon and T. Gheewala, “Moat-guarder Josephson SQUIDS”, *IEEE Trans. On Magn.* Vol. MAG-19, pp. 1160-64, May 1983.
- [22] M. Jeffery, T. Van Duzer, J.R. Kirtley and M.B. Ketchen, ”Magnentic imaging of moat-guarded superconducting electronic circuits”, *Appl. Phys. Lett.* Vol. 67, pp. 18-21, Sep. 1995.
- [23] G Stan, S.B. Field and J.M. Martinis, ” Critical filed for complete vortex expulsion from narrow superconducting strips”, *Phys. Rev. Lett.* 92, 097003, pp. 1-4, Mar. 2004.
- [24] I.L. Maksimov and G.M. Maksimova, ”Stability limits, structure and relaxation of a mixed state in superconducting films with a edge barrier”, *JETP Letters*, pp. 423-429, Mar. 1997.
- [25] D. Kouzoudis, M. Breitwisch and D.K. Finnemore, ” Edge barrier pinning for a superconducting vortex”, *Phys. Rev. B*, vol. 60, pp. 10508-12, Oct. 1999.
- [26] C.P. Bean and J.D. Livingston,” Surface barrier in Type II superconductors”, *Phys. Rev. Lett.*, vol 12, pp. 14-16, Jan. 1964.
- [27] M.M. Khapaev, "Extraction of inductances of plane thin film superconducting circuits", *Supercond. Sci. Technol.*, 1997, vol. 10, pp. 389-394.
- [28] M. M. Khapaev, A.Yu. Kidiyarova-Shevchenko, P. Magnelind, and M. Yu. Kupriyanov, “ 3D-MLSI: Software package for inductance calculation in multilayer superconducting interegrated circuits”, *IEEE Trans. on Applied Supercond.*, vol. 11, pp. 1090-93, Jan. 2001.
- [29] J.M. Jaycox and M.B. Ketchen, ”Planar coupling scheme for ultra-low noise DC SQUIDS”, *IEEE Trans. Appl. Magn.*, vol 17, pp 400-403, Jan 1981.
- [30] High Frequency Electromagnetic Software SONNET, Web page: [www.sonnetsoftware.com](http://www.sonnetsoftware.com)

- [31] A.A.Golubov and M.Yu. Kupriyanov, "Effect of solitary Abrikosov vortices on the properties of Josephson tunnel junctions", *Sov. Phys. JETP* vol. 65, pp. 849-55, Apr. 1987.
- [32] V.K. Semenov, Yu.A. Polyakov, and W. Chao, "Extraction of impacts of fabrication spread and thermal noise on operation of superconducting digital circuits", *IEEE Trans. Applied Supercond.*, vol. 9, pp. 4030-33, Jun. 1999.
- [33] D. Zinoviev and Y. Polyakov, "Octopux: an advanced automated setup for testing superconductor circuits", *New York State Workshop on Academic Electronics*, 1996.
- [34] K. Tanaka, T. Morooka, A. Odawara, Y. Mawatari, S. Nakayama, A. Nagata, M. Ikeda, K. Chinone and M. Koyanagi, "Study of trapped flux in superconducting thin film – observation by scanning SQUID microscope and simulation," *IEEE Trans. on Applied Supercond.*, vol. 11, pp. 230-34, Jun. 2001.
- [35] K. Suzuki, H. Kawamura, M. Maruyama, T. Hato, H. Suzuki, S. Yorozu, Y. Kameda, Y. Ishimaru, K. Nakayama, H. Wakana, S. Adachi, Y. Tarutani and K. Tanabe, "Investigation of the flux state in single-flux-quantum circuits with moats by scanning SQUID microscope", *Superconductor Science and Technology*, vol. 19, pp. 316-19, Mar. 2006.
- [36] K. Suzuki, H. Suzuki, S. Adachi, T. Utagawa, U. Kawabe and K. Tanabe, "Magnetic imaging of high -T<sub>c</sub> films with moat patterns by scanning SQUID microscope", *Physica C*, pp. 1301-05, Sep. 2002.
- [37] S. Polonsky, V. Semenov, and P. Shevchenko. "PSCAN: Personal superconductor circuit analyzer," *Supercond. Sci. Technol.*, vol. 4, pp 667-670, Nov. 1991.
- [38] K. Tanaka, T. Morooka, A. Odawara, K. Chinone and Y. Mawatari, "Optimized positions of Josephson Junctions to prevent trapping of magnetic fluxes in cooling under the static environment", *Physica C*, vol. 402, pp. 371-380, Mar. 2004.
- [39] S. L. Miller, K.R. Biagi, J. R. Clem, and D.K. Finnemore, "Critical currents of cross-type superconducting-normal-superconducting junctions in perpendicular magnetic fields", *Phys. Rev. B*, 31.2684, pp. 2684-2695, Mar. 1985.
- [40] P.I. Bunyk, S.V. Rylov, "Automated Calculation of Mutual Inductance matrices of multilayer superconductor integrated circuits," *Ext. Abs. ISEC'93*, p.62, 1993
- [41] V.K. Semenov, G. Danilov and D.V. Averin, "Reversible superconducting circuits using nSQUIDs", *IEEE Transactions Appl Supercond.*, vol 17, no.2, Jun 2007.
- [42] H. Terai, M. Tanaka, Y. Yamanashi, Y. Hashimoto, A. Fujimaki, N. Yoshikawa, Z. Wang, "Diagnostic Test of Large-Scale SFQ Shift Register," *IEEE Trans. Appl. Supercond.*, vol. 17, no. 2, pp. 422-425, Jun 2007.

- [43] V.K. Semenov and J. Ren, "Stimulus and Read-Out Interfaces for nSQUID arrays", Extended abstract ISEC 2007, Report P-U07.
- [44] Yu.A. Polyakov, S. Narayana and V.K. Semenov, "Flux trapping in superconducting circuits," *IEEE Trans. Appl. Supercond.*, vol. 17, no 2, pp.520-525, Jun 2007.
- [45] Supradeep Narayana, Yu. A. Polyakov and V. K. Semenov, "Evaluation of Flux Trapping in Superconducting Circuits," *IEEE Trans. Appl. Supercond.*, vol. 19, no 3, pp.640-643, Jun 2009.
- [46] S.K.Tolpygo, D. Tolpygo, R.T. Hunt, S. Narayana, Yu. A. Polyakov and V.K.Semenov, "Wafer Bumping Process and Inter-Chip Connections for Ultra-High Data Transfer Rates in Multi-Chip Modules With Superconductor Integrated Circuits," *IEEE Trans. Appl. Supercond.*, vol. 19, no 3, pp.598-603, Jun 2009.
- [47] S. Narayana, Yu. A. Polyakov, V.K. Semenov, S.K. Tolpygo and R.T. Hunt, "Design of Wafer-Bumps for Multi-Chip Modules with Ultra-High Data Transfer Rates," International superconducting electronics conference, Japan 2009.
- [48] Supradeep Narayana and V.K. Semenov, "Comparison of flux trapping in power independent and RSFQ D flip-flops," 15<sup>th</sup> US Workshop in Superconducting devices and circuits, 2008.
- [49] S. Narayana, V.K. Semenov and D. Averin, "Power Minimization Techniques in RSFQ Circuits," manuscript under preparation.
- [50] S. Narayana and V.K. Semenov, "Power Independent RSFQ Circuits", Extended abstract ISEC 2007, Report P-U01.
- [51] H. Terai, S. Yorozu, A. Fujimaki, N. Yoshikawa and Z. Wang, "Signal Integrity in large-scale single-flux-quantum circuit", *physica c:superconductivity*, vol 445-448, Oct 2006, pp 1003-1007.
- [52] K.Suzuki, S. Yorozu, Y. Kameda and K. Tanabe, "Investigation of magnetic flux state in Nb SFQ circuits by scanning SQUID microscope", *physica c:superconductivity*, vol 445-448, Oct 2006, pp 1034-1036.
- [53] M.Dorojovets and P.Bunyk, "Architectural and implementation challenges in designing high-performance RSFQ processors: A Flux-1 microprocessor and beyond," *IEEE Trans. Appl. Supercond.*, vol 13, No 2, Jun 2003, pp 446-449.
- [54] P.Bunyk, M.Leung, and M.Dorojovets, "Flux-1 RSFQ microprocessor: Physical design and test results," *IEEE Trans. Appl. Supercond.*, vol. 13, No 2, Jun 2003, pp 433-436.
- [55] Q.Herr, M.wire and A. Simth, "High speed data link between digital superconductor chips," *Appl. Phys. Lett.* Vol.80, pp 3210-3212, Apr 2002.



- [56] M.W Johnson,Q.P. Herr,D.J. Durand and L.A. Abelson,"Differential SFQ transmission using Either inductive or capacitive coupling," *IEEE Trans. Appl. Supercond.* , Vol 13,No 2,Jun 2005.
- [57] C.K. Teh, Y. Enomoto and Y. Okabe,"Current recycling technique using capacitive grounding," *Supercond. Sci. Technol.*, vol.16.2003,pp 1513-1517.
- [58] J.H. Kang and S.B. Kaplan,"Current recycling and SFQ signal transfer in Large scale RSFQ circuits," *IEEE Trans. Appl. Supercond.* ,vol. 13,No. 2, Jun 2003,pp 547-551.
- [59] J.H. Kang , D Gupta and S.B. Kaplan,"Demonstration of RSFQ digitizer on a mutichip module," *IEEE Trans. Appl. Supercond.* ,vol. 12,No.3, Sep 2002,pp 1848-1852.
- [60] W.Chen,A.V.Rylyakov,V.Patel,J.E. Lukens and K.K. Likharev,"Rapid single flux quantum T-flipflop operating up to 770 GHz," *IEEE Trans. Appl. Supercond.* ,vol. 19,No.1,Jun 1999,pp 3212-3215.
- [61] S. Tahara,S.Yorozu,Y. Kameda,Y. Hashimoto,H.Numata,T. Satoh,W. Hattori, and M. Hidaka,"Superconducting digital electronics," *IEEE Trans. Appl. Supercond.* ,vol. 11,Mar 2004,pp 463-468.
- [62] O. Mukhanov, A. Inamdar, T. Filippov, A. Sahu, S. Sarwana, and V.K. Semenov,"Superconductor components for direct digital synthesizer," *IEEE Trans. Appl. Supercond.* ,2007
- [63] D. Gupta, T.V. Filippov, A.F. Kirichenko, D.E. Kirichenko, I.V. Vernik, A. Sahu, S.Sarwana, P. Shevchenko, A. Talalaevskii, and O. A. Mukhanov,"*Digital Channelizing radio frequency receiver*", *IEEE Trans. Appl. Supercond.* ,2007.
- [64] M.R. Rafique, H. Engseth, A.Kidiyarova-Shevchenko,"Optimization of high frequency flip-chip interconnects for digital superconducting circuits,"*Supercond. Sci. Technol*, vol. 19,March 2006,pp. 354-361.
- [65] N. Yoshikawa and Y kato," Reduction of power consumption of RSFQ circuits by inductance-load biasing",*Superconductor Sci. Technol.*,Vol. 12,pp. 918-920,1999.
- [66] Stats Polonsky,"Delay insensitive RSFQ circuits with zero static power dissipation", *IEEE Trans. Appl. Supercond.*, vol 9 No2, pp 3535-39, June 1999.
- [67] A.H. Silver and Q. P. Herr,"A New concept for ultra-low power and ultra-high clock rate circuits", *IEEE Trans. Appl. Supercond.*, vol 11 No1, pp 333-37, March 2001.
- [68] M. Tanaka,T. Kondo,N. Nakajima,T.Kawamoto,Y. Yamanashi,Y. Kamiya,A. Akimoto,A. Fujimaki,H. Hayakawa,N. Yoshikawa,H. Terai,Y. Hashimoto, and S. Yorozu,"Demonstration

- of a single-flux-quantum Microprocessor using passive Transmission lines”, *IEEE Trans. Appl. Supercond.*, vol. 15, no.2, June 2005, pp. 400-403.
- [69] T. Ortlepp, Ariando, O. Mielke, C. J. M. Verwijs, K. F. K. Foo, H. Rogalla, F. H. Uhlmann, and H. Hilgenkamp, ”Flip-Flopping fractional flux quanta,” vol. 312, no. 5779, *Science* 9, Jun 2006, pp 1495-1497.
- [70] A. Silver, P. Bunyk, A. Kleinsasser and J. Spargo, ”Vision for single flux quantum very large scale integrated technology”, *Supercond. Sci. Technol.* Vol.19,2006, S307-S311.
- [71] A.M. Kadin, R.J. Webber and S. Sarwana, ” Effects of superconducting return currents on RSFQ circuit performance”, *IEEE Trans. Appl. Supercond.*, Vol 15, No. 2, June 2005.
- [72] K. Fujiwara, S. Nagasawa, Y. Hashimoto, M. Hidaka, N. Yoshikawa, M. Tanaka, H. Akaike, A. Fujimaki, K. Takagi, and N. Takagi, ” Research on Effective Moat configuration for Nb Multi-layer Device Structure,” *IEEE Trans Appl. Supercond*, vol 19, No. 3, Jun 2009, pp.607-610.
- [73] B. Ebert, T. Ortlepp and F.H. Uhlmann, ”Experimental Study of the Effect of Flux Trapping on the Operation of RSFQ Circuits,” *IEEE Trans Appl. Supercond*., vol 19, no 3, Jun 2009, pp.611-616.
- [74] K. Tagaki, M. Tanaka, S. Iwasaki, R. Kasagi, I. Kataeva, S. Nagasawa, T. Satoh, H. Akaike and A. Fujimaki, ” SFQ Propagation Properties in Passive Transmission Lines Based on a 10-Nb-Layer Structure,” *IEEE Trans Appl. Supercond*., vol 19, no 3, Jun 2009, pp.617-620.
- [75] O. Mielke, T. Ortlepp, B. Dimov, and F.H. Uhlmann, ”Phase Engineering Techniques in Superconducting Quantum Electronics, *J. Phys: Conf. Ser.*, 97(012196):9, 2008.
- [76] A.V. Ustinov and V.K. Kaplunenko, ”Rapid Single Flux Quantum Logic using  $\pi$ -Shifters,” *Journal of Appl. Phys.*, vol. 94, no.8, pp.5405-5407, 2007.
- [77] J.B. Majer, J.R. Butcher and J.E. Mooij, ”Simple Phase Bias for Superconducting Circuits,” *Appl. Phys. Lett.*, vol. 80, no. 19, pp. 3638-3648, 2002.
- [78] S.V. Rylov and R.P. Robertazzi, ”Superconductive high –resolution A/D converter with phase modulation and multi-channel timing arbitration,” *IEEE Trans Appl. Supercond.*, vol. 5, pp. 2260-2263, 1995.
- [79] V.K. Semenov and A. Inamdar, ” Limitations on Performance of Superconductor Oversampling ADCs ,” *IEEE Trans. Appl. Supercond.*, vol.15, no.2, Jun 2005.

- [80] I.V. Vernik, D.E. Kirichenko, T.V. Filippov, A. Talalaevskii, A. Sahu, A. Inamdar, A.F. Kirichenko, D.Gupta, and O.A. Mukhanov,” Superconducting High-Resolution Low-Pass Analog-to-Digital Converters”, *IEEE Trans. Appl. Supercond.*,2007.
- [81] F. Chiarello, P. Carelli, M.G. Castellano, C. Cosmelli, M.I. Khabipov, R. Leoni, G. Torrioli, A.B. Zorin, "Tunable flux qubits controlled by rapid single flux quantum logic: considerations and perspectives", Extended Abstracts, 10th International Superconductive Electronics Conference, ISEC 2005, P-C.04, Noordwijkerhout, NL, 2005.
- [82] HYPRES Nb Process Design Rules (30-1000-4500 A/cm<sup>2</sup>), Process #03- 10-45. HYPRES, Inc., Elmsford, NY 10523.Available:  
<http://www.hyres.com/pages/download/designrules/DesignRules.pdf>
- [83] S. K. Tolpygo, D. Yohannes, R.T. Hunt, J.A. Vivalda, D. Donnelly, D. Amparo, and A.F. Kirichenko, “20 kA/cm<sup>2</sup> process development for superconductor integrated circuits with 80 GHz clock frequency,” *IEEE Trans. Appl. Supercond.*, vol. 17, pp. 946-951, June 2007.
- [84] M. Hidaka, S. Nagasawa, K. Hinode, and T. Satoh, “Improvements in fabrication process for Nb-based single flux quantum circuits in Japan,” *IEICE Trans. Electron.*, vol. E91-C, pp. 318-324, Mar. 2008
- [85] K.E. Yokoyama, G. Akerling, A.D. Smith, and M. Wire, “Robust superconducting die attach process,” *IEEE Trans. Appl. Supercond.*, vol. 7, pp. 2631-2634, June 1997.
- [86] Y. Hashimoto, S. Yorozy, and T. Miyazaki, “Transmission of singleflux-quantum pulse between superconductor chips,” *Appl. Phys. Lett.*, vol. 86, pp. 072502-1 – 072502-3, Feb. 2005
- [87] Y. Hashimoto, S. Yorozy, T. Satoh and T. Miyazaki, “Demonstration of chip-to-chip transmission of single-flux-quantum pulses at throughputs beyond 100 Gbps,” *Appl. Phys. Lett.*, vol. 87, pp. 022502-022504, July 2005.
- [88] Y. Hashimoto, S. Yorozy, and Y. Kameda, “Development of cryopackaging and I/O technologies for high-speed superconductive digital systems,” *IEICE Trans. Electron.*, vol. E91-C, pp. 325-332, Mar.2008.
- [89] S. B. Kaplan, V. Dotsenko, and D. Tolpygo, “High-speed experimental results for an adhesive-bonded superconducting multi-chip module,” *IEEE Trans. Appl. Supercond.*, vol. 17, pp. 971-974, June 2007.
- [90] S.V. Polonsky, V.K. Semenov, and D.F. Schneider “Transmission of single-flux-quantum pulses along superconducting microstrip lines,” *IEEE Trans. Appl. Supercond.*, vol. 3, pp. 2598-2600, Mar. 1993.

## Appendix I

A compilation of some of the RSFQ cells and gates have been described which are used in the design of circuits, presented in chapters 2-7.

### A1.1 Splitter

SFQ pulses can be replicated with JTL's having two outputs. A single junction cannot drive more than two outputs. A tree of splitters is used to build large fanout circuits.

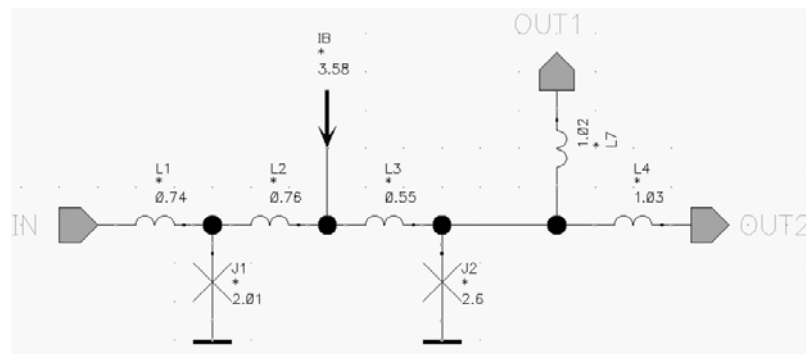


Figure A1.1: RSFQ splitter

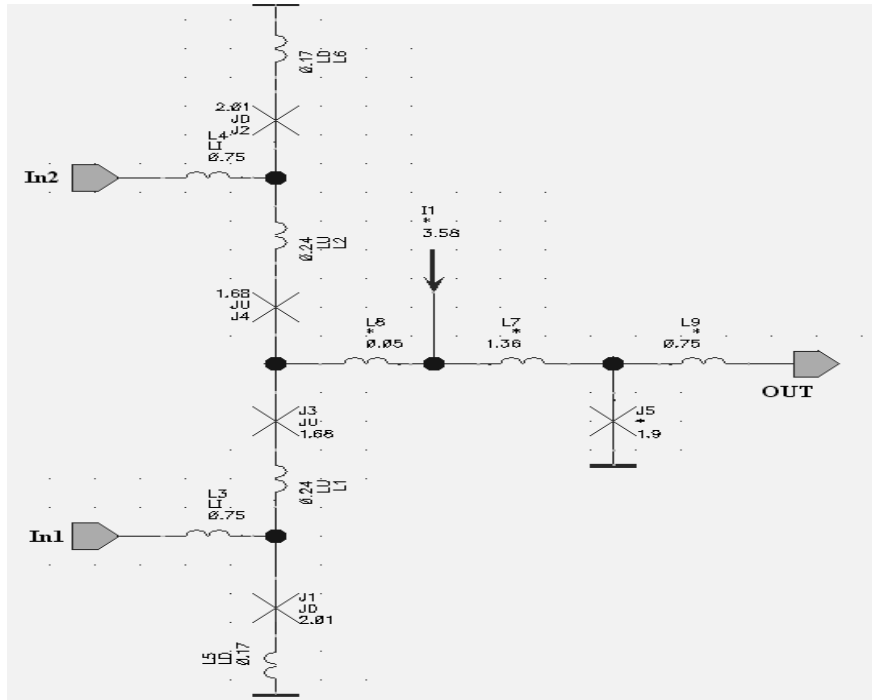
### A1.2 Confluence Buffer

If two pulses have to be merged a confluence buffer is used. Two buffer stages (comparators without quantizing inductance form buffers) constitute the CB as shown in figure A1.2. An SFQ pulse from in1 enter through J1 and leaves J5 , buffer junction J4 makes a  $2\pi$  phase jump preventing J2 from sending a pulse to in2 , a backward moving pulse. The arrival of two pulse will result in only one outgoing SFQ pulse (one pulse is rejected and only one is transmitted).

### A1.3 D Flip-flop

The clocked version of the RS flip-flop and the basic design is shown in figure A1.3. The clock is used as a reset for the RS flip-flop. The two states are 1 and '0' when a flux quantum is stored or not stored in J1-L1-J2 loop. Inductance L1 is a quantizing inductance and an SFQ pulse arrives at the junction J1 waits for the clock signal to be released by J2. The junction J0 is optional and acts as a buffer in case two signals arrive

before the reset signal. Without junction J0, D flip-flop is just a direct combination of a JTL and a controlled two junction comparator. The D flip-flop is used for construction of the shift registers used for flux trapping studies. More details will be illustrated in the following chapters.



FigureA1.2: RSFQ Confluence buffer

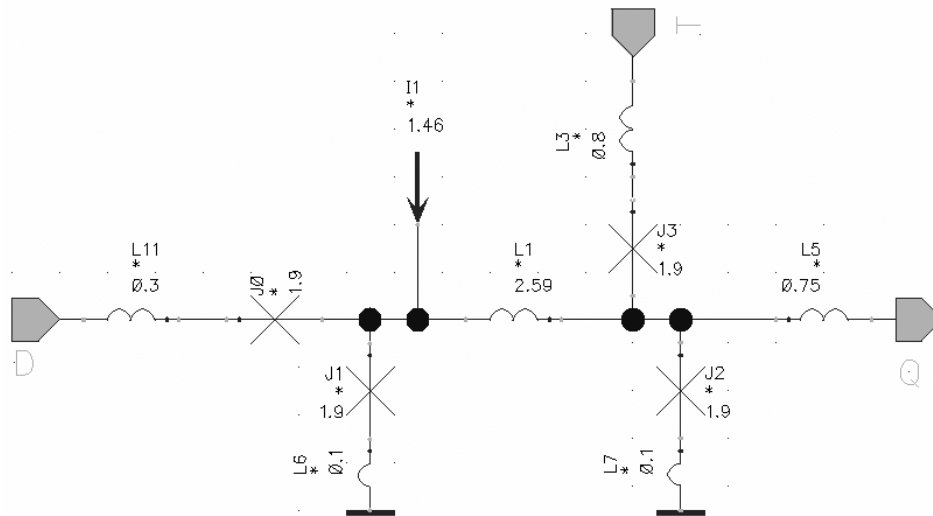


Figure A1.3: RSFQ D flip-flop

### A1.4 Superconducting Microstrip lines (SMSL)

An SFQ pulse can be interpreted as a superposition of microwaves. SMSLs need two metal layers: one for signal line and another for ground. SMSL introduces certain dispersion properties at high frequency where effective dielectric constant increases. However, in the present processes, the thickness of dielectric layer is very small. So dispersion in SMSL is negligible for wide bandwidth. In the current process, the SMSL are low ohmic ( $< 50 \Omega$ ). The implementation of high ohmic SMSLs is limited by Design Rules.

### A1.5 SMSL Driver

The function of the driver is to send a single SFQ pulse at a time through the connected SMSL. The resistance of SFQ driver ( $0.25\text{-}05 \text{ ohm}$ ) is used to decrease the quality factor of the resonator formed by the SMSL and thus to absorb all the traveling reflected signal generated at the receiver and impedance discontinuities. The Junction, JD, is designed with critical current slightly higher than that of JTL to compensate energy losses in the link due to series resistor and different impedance discontinuities.

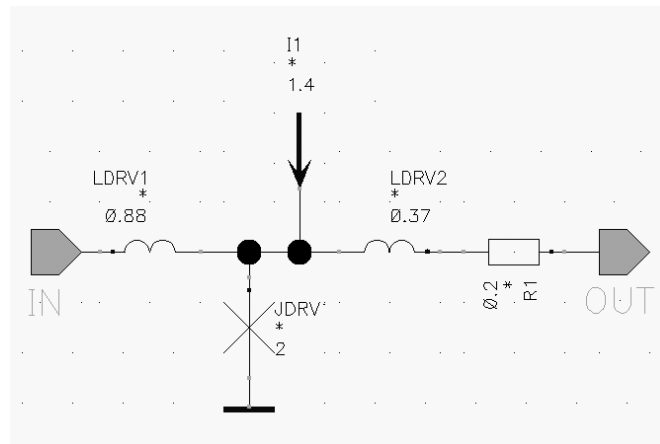
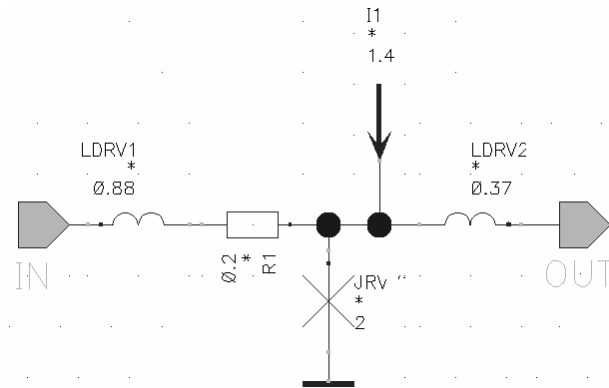


Figure A1.4: RSFQ SMSL driver

### A1.6 SMSL Receiver

The function of the receiver is a JTL with modified parameters. The critical current of the receiving input junction should be small to support SFQ pulses with very small energy.



**Figure A1.5: RSFQ SMSL receiver.**

## **A1.7 I/O interface**

The interface structures for SFQ electronics that was used in the circuits were SFQ/DC converter and DC/SFQ converters.

### **A1.7.1 Input:**

High speed reception of input of NRZ signals can be done with the DC/SFQ converter. DC/SFQ converter generates one SFQ pulse at the rising edge of the DC-signal input. The quantizing loop in the DC/SFQ converter is J2-L1-J1-J3, as shown in figure A1.6a. When a sufficiently high input current is applied from the DC-source, junction J2 switches and generates an SFQ pulse to the output and an anti pulse to the quantizing loop. The captured flux in the quantizing loop reduces the current through junction J2 below the critical current and increases the biasing of the junctions J1 and J3, junctions J1 and J3 act as a single junction. At the falling edge of the DC signal J1 and J3 switch restoring the initial state of the quantizing loop. Junction J4 is used as a matching element to the other RSFQ cells.

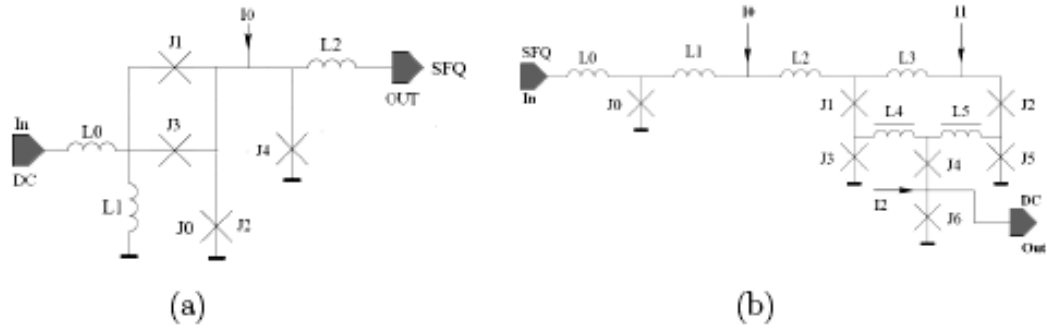


Figure A1.6: (a) DC/SFQ converter (b) SFQ/DC converter

### A1.7.2 Output:

The output of the RSFQ circuit is generated by a conventional SFQ/DC converter as shown in figure A1.6b. The junction J6 is responsible for generation of the output signal is embedded into quantizing interferometer J3-L4-L5-J5. In the initial state circulating current in the loop flows through the junction J3 and junction J6 is under biased and is in the superconducting state. SFQ pulse arriving to the input induces switching of the junction J3 and changes direction of the circulating current. Parameters of the circuit adjusted than critical current and it switches to the resistive state. It remains in the resistive state until arrival of the second incoming SFQ pulse. The output voltage is fabrication process dependent and typically is in the order of a few hundreds  $\mu\text{V}$ .

Each input also connection to the SFQ/DC converter to monitor correctness of the input test pattern. Combination of the DC/SFQ and SFQ/DC converters are the “monitors”. The voltage bias level and the signal amplitude define the monitor operation.